

New Photoanodes and Hole Transporting Materials for the Fabrication of Perovskite-Based Solar Cells

University of Seville

PhD Program:

“Ciencia y Tecnología de Nuevos Materiales”

Director: Shahzada Ahmad

Tutor: Agustín Rodríguez González-Elipe



ABENGOA
RESEARCH

2016

Fco. Javier Ramos Mellado

Acknowledgments/Agradecimientos

First of all, I would like to acknowledge Abengoa Research for giving me the opportunity to start my doctoral work. It was a great pleasure being part of this company, particularly, taking part of this pioneer project called Abengoa Research: doing cutting edge research in Spain, in sustainable energy field, looking for future business sounded as too many fantasies together but we combated and overcame them. Long live AR!

Thanks also to University of Seville and specially to responsables of Science and Technology of new Materials Program, since organizing a PhD Program under continuous changing conditions is never easy and you were able to consolidate it successfully.

Very important and personal thanks to my supervisor at Abengoa Research and the director of this thesis: Shahzada Ahmad, for trusting me and letting me work my way in a very exciting and motivating environment offering me always, the best was in your hand. I have learnt a lot from you, but the best is, I can really say I have a good friend for future.

My sincere thanks to Agustin Rodriguez González-Elipe, tutor of this thesis for giving me interesting and fruitful guidelines. Your immense knowledge was always instructive and motivational.

Next paragraph is booked for all my colleagues at Abengoa Research, in particular for all those worked next to me at lab: Samrana, Manuel, Laura, Elena, Gonzalo and all of them who helped me to complete this research work.

I cannot forget Manuel Doblaré, as main responsible of Abengoa Research project. You always had your door opened for any problem or question being able to solve everything was in your hand bringing a smile.

Very special thanks to Michael Grätzel and M.K. Nazeeruddin. It was an unforgettable opportunity working at EPFL with you. It has been probably the most inspirational experience in my life. I have learnt not only more science I could ever imagine there, but also I discovered myself living in other country.

Thanks also to all my colleagues at EPFL, they always helped and taught me in the right direction.

La prochaine reconnaissance est pour la famille Burrus. Xavier et Diane, vous m'avez fait sentir plus qu'un simple locataire à St. Sulpice, vous savez très bien que vous êtes pratiquement mes parents suisses parce que je me sens comme un serpeliou-espagnol. Merci beaucoup pour votre énorme gratitude et attention. Merci beaucoup de vos leçons linguistiques car le français que je suis capable de parler est grâce à vous. J'ai bien joui des débats et discussions, de mon étage à Zermatt et de la magnifique opportunité de découvrir la gastronomie suisse : raclette, fondue, papet vaudois et des fromages. Merci beaucoup et à bientôt!

A continuación, me tomaré la licencia de escribir unas pocas líneas en español.

Mamen y Saioa. Una parte bien importante de esta tesis es gracias a vosotras. Os voy a echar mucho de menos. Os deseo lo mejor, que es lo que me habéis dado, me habéis animado y me habéis hecho pasarlo bien olvidando el tedio del día a día. Gracias por no poder evitar sonreír aunque, a veces, vengan mal dadas. Vuestro positivismo y alegría es altamente contagioso. Seguid cultivándolo.

Me gustaría agradecer a todos los compañeros doctorandos en Abengoa, los que quedan y aquellos que pasaron. Me gustaría no perder nunca el contacto a través de los grupos de *whatsapp* Martes de cañas y DMHe. Ha sido una época apasionante de aprendizaje multidisciplinar y de continuo cultivo de la curiosidad, germen de toda ciencia y conocimiento. (Espero encontrar candidatos que custodien la Constitución de DMHe).

Para todos mis amigos del pueblo del que: *“Cual nevada paloma / que del azul del cielo / vino a posar el vuelo / en lo alto de una loma / castellana, / irradia su blancura / hacia la gran llanura / el Campo de Criptana. / Así la vio Cervantes / y la juzgó tan bella / que formó cien gigantes, tan blancos como ella, / para que con sus brazos extendidos / le dieran el más firme de los nidos,”* porque pese a la distancia que me ha acarreado esta etapa en mi vida, siempre me siento como en casa al recordar cuando alguna vez hemos entonado esos versos. Espero que perdure por muchos años el espíritu del Palomino's Club aunque, a veces, no lo podamos rememorar cuánto quisiéramos.

Sin moverme de geografía, a toda mi familia. Principalmente a mis padres y mi hermano. Papá y mamá, espero que seáis conscientes de que vuestro continuo apoyo y ánimo han sido los principales causantes de seguir siempre hacia delante con paso seguro y firme, sin desistir, sin dejar de esforzarse. Muchas gracias por vuestro sacrificio generoso y por vuestros sabios consejos. A veces, estúpidamente, estas cosas cuesta decirlas; aquí las tenéis para cuando queráis leerlas. Carlos, siento ser un manco y cansarte a menudo con mis torpezas informáticas; me gustaría devolverte la ayuda que me ofreces y poder vernos más porque siempre que estoy contigo aprendo mucho y me lo paso en grande. Por cierto, ahora ya me vas a poder cantar el *“Me hago doctor”* con razón. Además, un cariñoso recuerdo a mi abuela Josefina, a la que me cuesta recordar sin lágrimas al pensar en la alegría que hubiera sentido de haber visto completado este proceso.

Por último, a Miriam, mi novia y espero que, dentro de poco, mucho más. Sabes que has sido la principal sufridora de mis largas estancias lejos, mis malos humores en momentos estresantes y divagaciones varias que suponen esta tesis. Muchas gracias por tu apoyo, tu comprensión y tu cariño. Ten presente que, al final de una etapa se aprecia con añoranza y nostalgia el camino recorrido y con pasión y entusiasmo lo que está por llegar, *“o sea / resumiendo / estoy jodido / y radiante / quizá más lo primero / que lo segundo / y también / viceversa”*.

“Ipsa scientia potestas est”
(knowledge itself is power)

-Sir Francis Bacon
In *Meditationes Sacrae* (1597)

“Any problem can be solved using the materials in the room”

-Edwin Herbert Land.
In Peter C. Wensberg, *Land's Polaroid: A Company and the Man Who Invented It*
(1987).

Abstract

Perovskite Solar Cells (PSC) is one the most recent photovoltaic approaches to transform directly sun light into electricity. Though perovskite type materials are known for more than a century, the employment of novel hybrid organic-inorganic perovskite materials as absorbers in photovoltaic was recently developed, firstly in 2009 using perovskite with a liquid electrolyte based devices and afterwards in 2012 with the start of the so-called *perovskite fever* employing a solid-state configuration. During this short period of existence, the evolution of PSC field has been prompt and substantial, and power conversion efficiencies over 20% at lab scale are being obtained.

In a typical PSC configuration, perovskite absorber layer is placed between electron-transporting material (ETM) and hole-transporting material (HTM). Normally, ETM layer consisted of mesoporous films made of inorganic metal oxides particles, principally TiO_2 , other metal oxide as well as *n*-type organic or inorganic based materials. At lab scale, ETM can be easily dispensed through solutions process spin coating technique to prepare the photoanode of the PSC. However it is unscalable and high material consuming process. For the HTM, some molecules are extensively reported in the literature due to its performance such as 2,2',7,7'-Tetrakis[N,N-di(4-methoxyphenyl)amino]-9,9'-spirobifluorene (Spiro-OMeTAD) and Poly(triaryl amine) (PTAA). However, they have some disadvantages such as their high price, difficult synthesis and the requirement of adding certain compounds for high performance which reduce the final stability of devices.

In order to overcome the cited drawbacks of existing ETM and HTM for PSC fabrication, some novel alternatives have been exposed in the present work to solve the state of the art issues.

Firstly, ZnO porous columnar thin films grown by plasma enhanced chemical vapor deposition (PECVD) were used as effective photoanodes in PSC. With this method it is also possible to control the deposition conditions over large area. Furthermore, columnar TiO_2 films grown by physical vapor deposition at oblique angle incidence (PVD-OAD) were also applied as photoanodes in PSC; the resulting thickness and porosity of thin films can be modified by tuning the incidence angle. In addition, with the employment of PVD-OAD technique, rational design of 1-dimensional photonic crystals (1-DPC) layers were implemented as photoanodes in PSC exhibiting enhanced optical and absorbing properties. The techniques employed here for the photoanode development were solvent free and present good control of the film properties and homogeneity over large area.

On the other hand, novel HTM molecules were explored in PSC fabrication. Moreover, all the studied molecules presented highest occupied molecular orbital (HOMO) levels compatible with perovskite valence band, making them candidates to be used in PSC. The soluble pentacene derivatives such as TIPS-pentacene, was reported for first time as efficient and stable HTM in PSC without the use of any additive. A non-aggregated phthalocyanine molecule (coded as TT80), soluble in organic apolar solvents has been described as HTM in PSC as well. Two novel molecules, which were easy to synthesize and were based on triazatruxene

compounds (named as HMDI and HPDI), were design as such to ensure high solubility in apolar solvents, improved stability and performance in PSC.

In conclusion, by introducing novel ETM architectures and HTM compounds, the spectrum of possibilities in the field of PSC has been expanded. This offers new pathways for future PSC development and commercialization.

Resumen

Las celdas solares de perovskita (PSC, del inglés *perovskite solar cells*) se consideran uno de los ejemplos de tecnología fotovoltaica más recientes para transformar de manera directa la luz solar en electricidad. Aunque las perovskitas son materiales que se conocen por más de un siglo, la utilización de perovskitas híbridas orgánicas-inorgánicas como materiales absorbedores en dispositivos fotovoltaicos es relativamente reciente, siendo usadas por primera vez en 2009 en dispositivos fotovoltaicos con electrolito líquido y, poco después, al comienzo de la *fiebre de la perovskita* en 2012, en configuraciones en estado sólido. En este breve lapso de tiempo, la evolución en este campo fotovoltaico ha sido rápida y sustancial, habiéndose logrado eficiencias en la conversión superiores al 20% a escala de laboratorio.

En una configuración de PSC típica, la capa de perovskita que funciona como absorbedor de luz se encuentra ubicada entre un material transportador de electrones (ETM, del inglés *electron-transporting material*) y un material transportador de huecos (HTM, del inglés *hole-transporting material*). Normalmente, la capa de ETM consiste en una lámina mesoporosa hecha de partículas de óxidos metálicos (TiO_2 , principalmente), pero también se pueden encontrar otros materiales semiconductores tipo-n, tanto orgánicos como inorgánicos. A escala de laboratorio, el ETM se puede dispensar fácilmente a través de técnicas de *spin-coating* para preparar los fotoánodos de las PSC. Sin embargo, este proceso no es escalable y requiere un gran consumo de productos. En el caso de los HTM, algunas moléculas como 2,2',7,7'-Tetrakis[N,N-di(4-metoxifenil)amino]-9,9'-spirobifluoreno (Spiro-OMeTAD) y Poli(triarilamina) (PTAA) han sido extensamente documentadas en bibliografía debido a su contrastado comportamiento. No obstante, dichos compuestos presentan algunos inconvenientes como su elevado precio, su difícil síntesis, así como la necesidad de añadir ciertos aditivos en su composición que disminuyen la estabilidad de los dispositivos fotovoltaicos.

Para solventar los problemas encontrados en el estado del arte que tienen relación con el uso de ETM y HTM en la fabricación de PSC, se han propuesto algunas nuevas alternativas en el presente trabajo.

De este modo, en primer lugar, se han implementado láminas delgadas porosas basadas en columnas de ZnO crecidas mediante deposición química en fase vapor mejorada por plasma (PECVD, del inglés *plasma-enhanced chemical vapor deposition*) como fotoánodos de PSC, siendo eficientes y habiéndose empleado técnicas fácilmente escalables y homogéneas sobre grandes superficies para su preparación. En segundo lugar, mediante la técnica de deposición física en fase vapor bajo ángulo de incidencia oblicuo (PVD-OAD del inglés *physical vapor deposition at oblique angle deposited*), se han preparado films nanocolumnares de óxido de titanio que se han introducido como ETM poroso de PSC, donde ciertas propiedades del fotoánodo tales como la porosidad pueden ser controladas de manera precisa modificando el ángulo de incidencia. Además, con el uso de la misma técnica se han diseñado cristales fotónicos porosos de 1-dimensión (1-DPC, del inglés *1-dimensional photonic crystal*) que sirven de fotoánodos de PSC con propiedades ópticas y de absorción mejoradas en los dispositivos fotovoltaicos.

Todas las técnicas para la fabricación de los novedosos fotoánodos expuestos en este trabajo reúnen las características de ser fácilmente escalables, controlables y homogéneas sobre gran superficie.

Por otro lado, se han testado nuevas moléculas como HTM para la fabricación de PSC. Asimismo, todos los compuestos analizados presentan orbitales moleculares con niveles energéticos de alta ocupación (HOMO, del inglés *highest occupied molecular orbital*) compatibles con la banda de valencia de la perovskita, haciendo factible así su uso como HTM de PSC. El derivado del pentaceno soluble en disolventes orgánicos llamado TIPS-pentaceno, ha sido empleado como HTM de PSC sin incluir ningún tipo de aditivo en su formulación. También se ha demostrado que una molécula basada en ftalocianina (llamada TT80), que no presenta agregación y es soluble en disolventes orgánicos apolares, se ha podido introducir como HTM en PSC. Por último, se han concebido dos compuestos orgánicos basados en triazatruxeno (llamados HMDI y HPDI) que presentan alta solubilidad en disolventes orgánicos y se han implementado como HTM de PSC con alta estabilidad y buen comportamiento.

En conclusión, mediante el uso de nuevas arquitecturas porosas en el ETM, y nuevos compuestos para el HTM, se ha incrementado el espectro de posibilidades en el campo de las PSC. De esta manera, se han abierto nuevas rutas interesantes de cara al futuro desarrollo y comercialización de las tecnologías basadas en PSC.

List of abbreviations

1-DPC	1-dimesional photonic crystal
AM	Air mass
AM1.5G	Reference solar spectral irradiance according to American Society for Testing Materials, ASTM G-173-03
bl-TiO ₂	TiO ₂ blocking layer
CIGS	Copper indium gallium selenide
CVD	Chemical vapor deposition
DFT	Density functional theory
DMF	<i>N,N</i> -Dimethylformamide
DMSO	Dimethylsulfoxide
DSC	Differential scanning calorimetry
DSSC	Dye-sensitized solar cell
ETA	Extremely thin absorber
ETM	Electron-transporting material
FA	Formamidinium: (NH ₂ -CH=CH ₂) ⁺
FF	Fill factor
FTO	Fluorine doped tin oxide
GBL	Gamma-butyrolactone (γ -butyrolactone)
HMDI	5,10,15-Trihexyl-3,8,13-trimethoxy-10,15-dihydro-5 <i>H</i> -diindolo [3,2- <i>a</i> :3',2'- <i>c'</i>]carbazole
HOMO	Highest occupied molecular orbital
HPDI	5,10,15-Tris(4-(hexyloxy)phenyl)-10,15-dihydro-5 <i>H</i> -diindolo [3,2- <i>a</i> :3',2'- <i>c'</i>]carbazole
HTM	Hole-transporting material.
IPCE	Incident photon-to-current efficiency
LED	Light-emmiting diode
LiTFSI	Bis(trifluoromethane)sulfonimide lithium salt
LUMO	Lowest unoccupied molecular orbital
MA	Methylammonium: (CH ₃ NH ₃) ⁺

MPP	Maximum power point
mp-TiO ₂	Mesoporous TiO ₂
NC-TiO ₂	Nanocolumnar TiO ₂
NREL	National Renewable Energy Laboratory
OPV	Organic photovoltaics
PCE	Power conversion efficiency. Also represented as η
PECVD	Plasma-enhanced chemical vapor deposition
PL	Photoluminescence
PSC	Perovskite solar cell
PTAA	Poly(triaryl amine), Poly[bis(4-phenyl)(2,4,6-trimethylphenyl)amine]
PV	Photovoltaic
PVD- OAD	Physical vapor deposition at oblique incidence angle
QDSC	Quantum dot solar cell
SC	Solar cell
SEM	Scanning electron microscopy
Spiro- OMeTAD	2,2',7,7'-Tetrakis[<i>N,N</i> -di(4-methoxyphenyl)amino]-9,9'- spirobifluorene, N ² ,N ² ,N ^{2'} ,N ^{2'} ,N ⁷ ,N ⁷ ,N ^{7'} ,N ^{7'} -octakis(4-methoxyphenyl)-9,9'- spirobi[9H-fluorene]-2,2',7,7'-tetramine
ss-DSSC	Solid-state dye sensitized solar cell
t-BP	4- <i>tert</i> -Butylpyridine
TCO	Transparent conducting oxide
TIPS	Triisopropylsilylethynyl
ToF-SIMS	Time of flight-secondary ion mass spectrometry
TT80	Zn(II)octa(2,6-diphenylphenoxy) phthalocyanine

List of symbols

c	Speed of light $c = 2.99792 \times 10^8 \text{ m s}^{-1}$
e^-	Electron
E_b	Binding energy
h	Planck constant. $h = 6.62607 \times 10^{-34} \text{ J s} = 4.13567 \times 10^{-15} \text{ eV s}$
E_g	Band gap
$E_{g \text{ opt}}$	Optical band gap
h^+	Hole
I_0	Dark saturation diode current
I_D	Dark current, also known as diode current
I_L	Light generated current
I_{SC}	Short-circuit current
I_{SH}	Shunt current
J_0	Dark saturation diode current density
J_D	Dark current, also known as diode current density
J_L	Light generated current density
J_{MPP}	Current density at maximum power point
J_{SC}	Short-circuit current density
k_B	Boltzmann constant. $k_B = 1.38065 \times 10^{-23} \text{ J K}^{-1} = 8.61733 \times 10^{-5} \text{ eV K}^{-1}$
m	Diode ideality factor
n	Refractive index
q	Elementary charge. $q = 1.60218 \times 10^{-19} \text{ C}$
R_S	Series resistance
R_{SH}	Shunt resistance.
t	Tolerance factor
T	Temperature
T_g	Glass transition temperature
V_{MPP}	Voltage at maximum power point
V_{OC}	Open-circuit voltage

Greek letters

α	Incidence glancing angle
β	Tilting angle
θ	Zenithal angle
λ	Wavelength
μ	Octahedral factor
ρ_N	Charge carrier density in number of particles /volume. Frequently represented in literature simply as n
Φ	Photon flux

Table of contents

Acknowledgments/Agradecimientos	- III -
Abstract	- VII -
Resumen	- IX -
List of abbreviations	- XI -
List of symbols	- XIII -
Greek letters	- XIV -
Table of contents	- XV -
1. Introduction	- 1 -
1.1 Brief history of PV	- 3 -
1.1.1 Early PV approaches	- 3 -
1.1.2 1st Generation PV	- 4 -
1.1.3 2nd Generation PV	- 5 -
1.1.4 3rd Generation PV	- 5 -
1.1.5 Perovskite solar cells (PSC)	- 6 -
1.1.6 Summary and efficiency chart	- 7 -
1.2 Solar Cell Characterization	- 9 -
1.2.1 Solar spectra	- 9 -
1.2.2 I - V characteristics	- 10 -
1.2.3 Incident Photon-to-Current Efficiency (IPCE)	- 12 -
1.3 PSC principles	- 14 -
1.3.1 Perovskite: basics and general description	- 14 -
1.3.2 Perovskite Crystal Structure	- 15 -
1.3.3 Optical properties	- 18 -
1.3.4 Electronic properties and charge recombination	- 20 -
1.3.5 Device architecture	- 25 -
1.3.6 Deposition routes	- 28 -
1.3.7 Spin coating 1-step deposition	- 29 -
1.3.8 Other aspects to consider for future commercialization	- 30 -
1.4 Motivation and scope of this work.	- 32 -
Literature	- 34 -
2. Objectives	- 47 -

3.	Global summary of results	- 51 -
3.1	PSC based on nanocolumnar plasma deposited ZnO thin films	- 53 -
3.2	Nanocolumnar 1-dimensional TiO ₂ photoanodes deposited by PVD-OAD for PSC fabrication	- 56 -
3.3	Porous 1-dimensional nanocolumnar structures as effective photonic crystal for PSC	- 61 -
3.4	A dopant free linear acene derivative as a HTM for PSC	- 65 -
3.5	Non-aggregated Zn(II)octa(2,6-diphenylphenoxy) phthalocyanine as a HTM for efficient PSC	- 68 -
3.6	Rational design of triazatruxene based hole conductors for PSC	- 70 -
4.	Global discussion of results	- 75 -
4.1	PSC based on nanocolumnar plasma deposited ZnO thin films	- 77 -
4.2	Nanocolumnar 1-dimensional TiO ₂ photoanodes deposited by PVD-OAD for PSC fabrication	- 78 -
4.3	Porous 1-dimensional nanocolumnar structures as effective photonic crystal for PSC	- 80 -
4.4	A dopant free linear acene derivative as a HTM for PSC	- 82 -
4.5	Non-aggregated Zn(II)octa(2,6-diphenylphenoxy) phthalocyanine as a HTM for efficient PSC	- 84 -
4.6	Rational design of triazatruxene based hole conductors for PSC	- 85 -
5.	Conclusions	- 87 -
	Appendix	- 91 -
	Presentation of doctoral thesis (official document)	- 93 -
	Appropriateness report	- 95 -
	Contribution report	- 97 -
	Report of scientific relevance of the publications	- 99 -
	List of publications	- 103 -
	Copy of publications contained in this thesis	- 105 -
	International mention (official document)	- 185 -
	International experts reports	- 187 -
	Certificate of stays	- 191 -
	List of stays	- 193 -
	List of patents	- 193 -
	List of conferences	- 194 -

1. Introduction

1.1 Brief history of PV

Solar cells transform sunlight directly into electricity with the employment of semiconductor materials through photovoltaic (PV) effect. Although PV installation has increased considerably in recent years, and the total power installed capacity in the world was $\sim 233\text{GW}_p$ by the end of 2015¹ and will be between $396\text{--}540\text{GW}_p$ by the end of 2019 [1] (Figure 1.1). The growth of PV technologies has been long and irregular. In the following sections, a short historical overview of PV technologies will be presented.

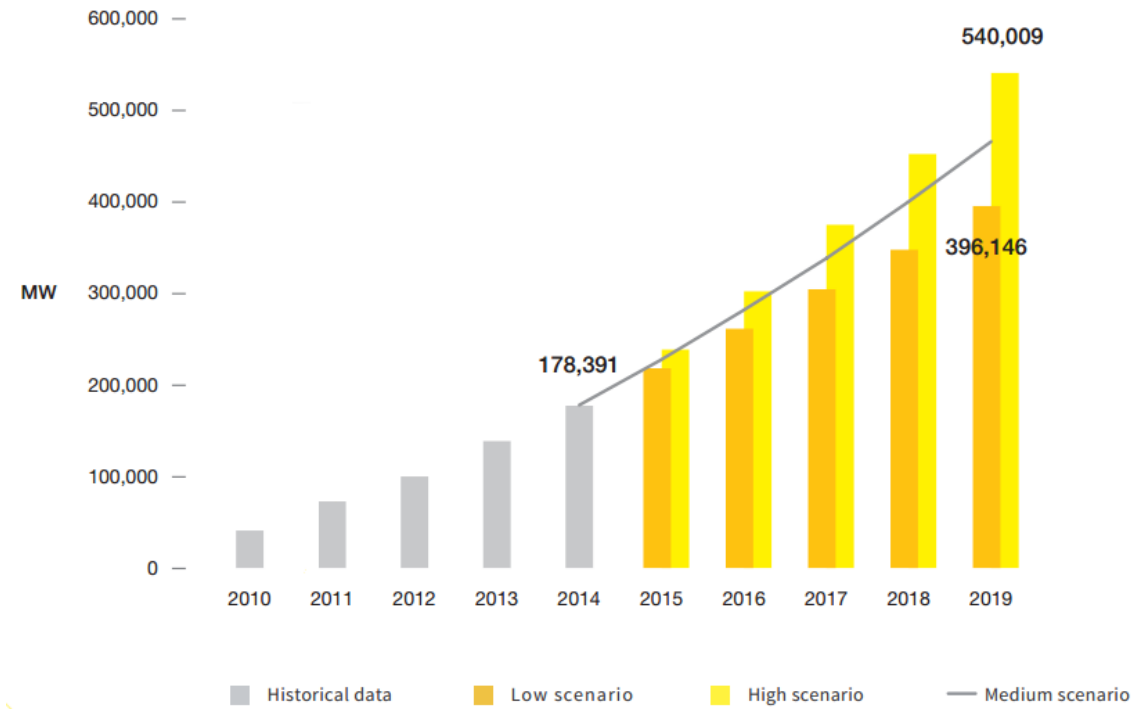


Figure 1.1. World solar PV cumulative market scenarios until 2019. Source: Solar Power Europe (SPE) [1].

1.1.1 Early PV approaches

The PV effect was discovered by A. E. Becquerel in 1839 where silver halides coated electrodes improved the generated current in the presence of blue and violet light [2].

Further, in 1877, W.G. Adams and R.E. Day noticed the generation of a current between two platinum wires connected at the edges of a vitreous selenium cylinder [3], *i.e.* the first evidence of PV effect in a solid state device ever. During the Universal exhibition 1878 in Paris, A. Mouchot displayed the first solar power generator.

Following this, in 1883, C. Fritts was able to fabricate a *thin film* solar cell sandwiching $25\text{--}125\ \mu\text{m}$ of Se between a metal and a gold leaf manually pressed to the Se surface [4]. Although these Se thin film PV prototypes were poorly efficient ($<1\%$ Power Conversion Efficiency, PCE), it is worth to mention the

¹ To be updated by June 2016 in the 2016 SPE report.

overall configuration was quite similar to the current silicon solar cell technology. C. Fritts was the first to demonstrate the capability of this field, identifying the use of low cost materials and process, and the power storage as critical points for a future development of this technologies [5], being both topics are still essential nowadays.

After several decades, during early 1930's there was a renaissance in PV technologies due to the copper-cuprous oxide junctions (Cu-Cu₂O). Almost 40 scientific works were reported in Grondahl's review in 1933 for this junction couple. [6]. A typical configuration of the original Cu-Cu₂O PV cells consisted on cuprous oxide grown over metallic copper; a Pb wire was pressed to cuprous oxide with a glass plate [5]. For the first time, a transparent side was described in a layered architecture to allow the light come into the cell.

Taking advantage of the Cu-Cu₂O impulse, selenium based solar cells were studied further and improved, converting in the dominant variety of PV those days [7]. During that decade, more precisely in 1832, the PV effect in Cadmium selenide (CdSe) was demonstrated by Audobert and Stora. In 1839, Nix and Treptwo reported thalious sulphide (Tl₂S) as semiconductor for PV [8].

1.1.2 1st Generation PV

J. Czochralski invented the method to produce single crystal metal ingots from molten solutions with the help of a seeding agent by 1918 [9]. Nevertheless, until thirty years later, this process was not adapted to grow semiconductor single-crystal ingots. Czochralski process variation to grow crystalline germanium and later silicon was conceived in 1948 by G. Teal and J. Little [10], being considered as the starting point for subsequent first generation PV.

Another decisive development in the PV field took place in 1941, when doping was utilized for first time creating *p*- and *n*-type doped Si [11].

During 1950's, Bell Labs were focused in the fabrication of solar cells for space purposes. In 1954, the first silicon solar cell with a PCE of ~6% based on a p-n junction was fabricated by the Bell Lab team composed of Daryl Chapin, Calvin Fuller and Gerald Pearson [12]. That was a major breakthrough in the field of PV technologies, since only 0.5% PCE were obtained earlier this advance. For first time, a functional solar cell showed a decent PCE that allowed its implementation in several applications. After further optimization, Bell Labs was able to produce silicon solar cell with 11% PCE. That was considered as the birth for 1st generation PV.

1st Generation PV comprises both monocrystalline and polycrystalline silicon solar cells. The main difference between mono- and polycrystalline silicon relies on the crystal size. While monocrystalline silicon has a grain size over 10 cm, polycrystalline has much smaller, and is normally between 1 μm-1 mm (when grain size is between 1 mm-10 cm it is often termed as multicrystalline) [13].

From an industrial prospects, monocrystalline silicon is being grown by Czochralski process; whereas polycrystalline silicon is produced by either Siemens or fluidized bed reactor (SBR) processes to achieve very high purity silicon (solar grade).

Currently, first generation PV solar cells are able to reach 25.6% of PCE for monocrystalline and 21.25% for polycrystalline at lab scale (Figure 1.2). While in a solar modules 22.9% and 19.2% PCE is being offered respectively [14]. Presently, PV market is clearly dominated by 1st generation silicon crystalline solar panels with a ~90% of the global market [15].

1.1.3 2nd Generation PV

In order to find other alternatives inside PV technology, which consuming less material and potentially more efficient and cheaper than the ones based on silicon, thin film based technology was developed. They were termed as 2nd generation PV and appeared in 1970's. These type of thin film PV were made of either III-V (*e.g.* GaAs), II-VI (such as CdTe and CdS) or I-III-VI₂ (for example CIGS) semiconductors or amorphous silicon. In these configurations, the absorber is presented as a thin film, in order to save material and hence reducing the cost.

One important highlight during this period was the first GaAs heterostructure created by the Nobel prize winner, Z. Alferov and coworkers in 1970 [16]. GaAs is one of the most interesting alternatives to replace crystalline silicon with certified PCE of 28.8% in single junction solar cells and 24.1% for modules [14].

Copper Indium Gallium Selenide (CIGS) and Cadmium telluride (CdTe) thin films based absorbers were also classified in this category. PCE of 22.3% for CIGS and 22.1% for CdTe at lab scale and modules with 17.5% and 18.6% respectively have been reported recently [14].

Additionally, in 1976, D. Carlson and C. Wronski developed the first amorphous silicon (a-Si) solar cell with 1.1% of PCE [17]. Two years later, the first solar calculator was developed using this technology. Although at that moment the performance was limited, it paved the route to take advantage of a material which today dominates the world of mini PV applications, such as calculators and small fans. PCE of 10.2% for a-Si and 13.6% using a multijunction in combination with nanocrystalline silicon were certified leading this sector [14].

Today, approximately the 10% of the market is covered by thin film technologies [15]. However, certain issues as toxicity and the use of low abundant materials must be solved.

1.1.4 3rd Generation PV

The most recent PV impulse has been the so-called 3rd Generation PV; a diverse variety of different PV approaches belongs to this group. 3rd Generation PV consist in diverse technologies, not fully commercially exploited yet, which could allow a reduction in the final watt peak price and they have been developed since 1990's. They are potentially cheap and easy to fabricate. These PV technologies still need more research to push the efficiencies and to circumvent certain issues to be reliable for industrial scale.

Dye-Sensitized Solar Cells (DSSC) are considered as the first approach inside this category. DSSC were presented by B. O'Regan and M. Grätzel in 1991 using a mesoporous TiO₂ (mp-TiO₂) photoanode, a Ru complex dye and iodide/triiodide

redox liquid electrolyte with PCE over 7% [18]. To avoid leakage and corrosion issues caused by liquid redox electrolytes, solid-state dye-sensitized solar cells (ss-DSSC) were developed placing an organic hole transporting material (HTM) instead of liquid redox shuttle. First report for ss-DSSC was published by U. Bach and coworkers in 1998 showing a 0.74% PCE [19]. Nowadays, DSSC technologies have shown interesting results, their working principles have been understood and a wide variety of approaches and alternatives have been created [20]. The Japanese company Sharp have certified efficiencies of 11.9% in the case of liquid DSSC (8.8% for a submodule) [14] while lower performances was reported for ss-DSSC, a respectable PCE of 7.2% was reported when small organic solid molecule 2,2',7,7'-Tetrakis[*N,N*-di(4-methoxyphenyl)amino]-9,9'-spirobifluorene (Spiro-OMeTAD) was placed as HTM [21], and 10.2% for inorganic HTM based on perovskite structure [22].

Organic Photovoltaics (OPV) belongs to the area of electronics where conductive organic polymers and/or small organic molecules are responsible for the absorption of light and generation of charges by PV effect. They have been developed since early 2000's. Similarly to DSSC, OPV has offered plenty of alternatives with potentially cheap solutions [23]. Champion cells certified in this field have shown PCE of 11.0% for lab scale and 8.7% for a module, both made by Toshiba [14].

When a crystal of semiconductor material such as: PbS, PbSe, CdS, CdSe or CdTe is small enough (in the order of nanometers) quantum confinement in the three directions of space can be found forming quantum dots. These semiconductor nanoparticles can absorb light and transmit its energy to a second semiconductor which is sensitized by the quantum dots transferring the generated charges. Quantum Dot Solar Cells (QDSCs) are based on this principle. Although the sophisticated physics is underlying these devices, the fabrication approach is simple, being possible the preparation through solution process in a simple manner with a well control of the bandgap and an easy tuning of the absorption spectra by tuning the size of the dots [24]. PCE of 10.6% was certified using QDSC by Toronto University.

Finally, the most recent technology discovered inside 3rd generation PV has been perovskite solar cells that will be explained more in detail in subsequently section.

1.1.5 Perovskite solar cells (PSC)

Hybrid organic-inorganic perovskite solar cells (PSC) have been the most recent advance in 3rd Generation solar cells. Perovskites with PV interest are based in halides with central cations having oxidation state +2 such as lead (II) or Sn (II) and organic cations +1 like methylammonium (MA) or formamidinium (FA).

Mitzi and coworkers from IBM Center developed several organic-inorganic perovskites with other organic cations for diverse electronic applications such as transistors and light emitting diodes [25]–[29]. In 2009, Miyasaka and coworkers published the first approach using MAPbI₃ and MAPbBr₃ perovskites as absorbers in DSSC with a limited PCE of 3.8% [30]. After that, Park's group showed a QDSC using perovskite with a very promising 6.5% PCE [31], however the structure still uses corrosive liquid electrolytes.

In 2012, methylammonium lead triiodide perovskite (MAPbI₃) was introduced in a solid state devices forming a continuous film of perovskite, sandwiched between the electron transporting material (ETM) and hole transporting material (HTM) showing efficiencies over 9% [32]. Another significant characteristic has amplified the interest over PSC was the demonstration of ambipolar conductivity, *i.e.* both electrons and holes can be transported in hybrid organic-inorganic perovskites [22], [33], [34]. Grätzel and coworkers pushed this research field by reporting and certifying a highly efficient solar cell using sequential deposition route [35]. Nowadays efficiencies >20% have been reported in literature [36], [37] with a certified record of PCE=22.1% from KRICT/UNIST, Korea. In addition, efficiencies of 15.6% have been certified recently using active areas bigger than 1 cm² [38].

1.1.6 Summary and efficiency chart

A summary of the best efficiency research cell efficiencies is shown in Figure 1.2. This work is compiled by National Renewable Energy Laboratory (NREL). Crystalline Si is represented in blue, 2nd generation PV cells are in green (except GaAs is in purple), and emerging 3rd generation PV are depicted in orange-red. Heterojunctions are represented in purple (except the abovementioned GaAs case). Heterojunctions were not explained before because they are out of the scope of these work but, essentially, they consist on devices with several semiconductors with different band gaps where each semiconductor absorbs certain range of wavelength.

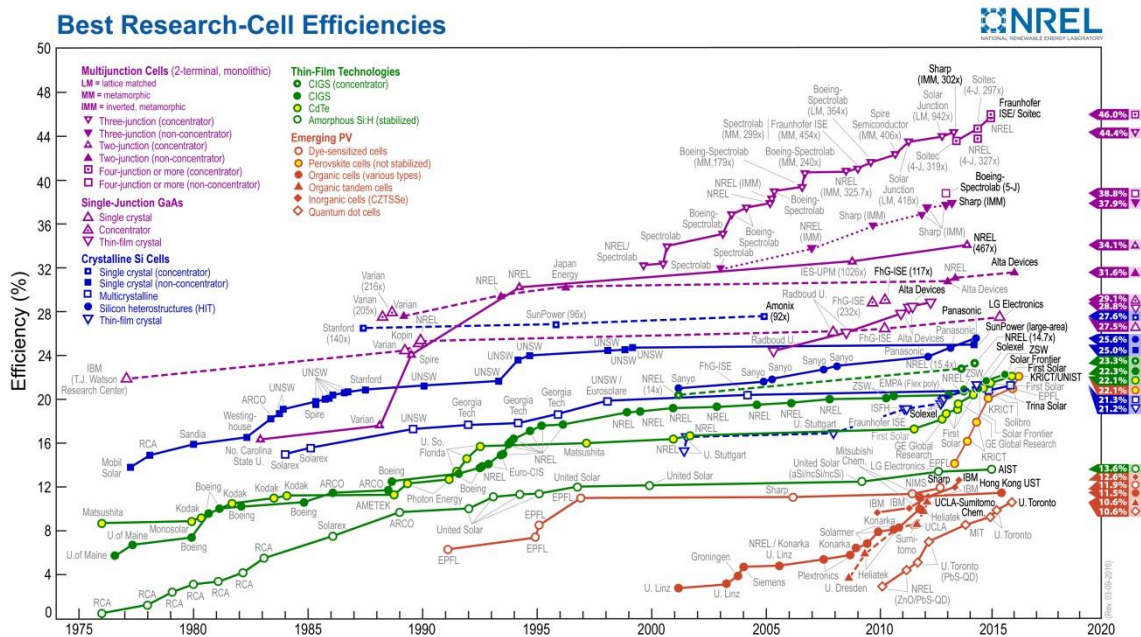


Figure 1.2. Best research-cell efficiencies chart for different PV technologies. Extracted from NREL website.

On the basis of absorption of light and charge carrier take place together (in the same material) or separated (in two different ones), PV cells can be classified in semiconductor and sensitized solar cell respectively. Whereas in semiconductor solar cells 1st, 2nd generation PV are included; between sensitized solar cells DSSC (both liquid and solid) and QDSC are counted in.

The case of OPV is more complex, since, light absorption occurs in the donor molecule and the generated Frenkel exciton is diffused to the interface where the splitting of excitons takes place; then charges travel from that interface to the edges. They are not purely semiconductors because they need an interface to dissociate the high energy Frenkel exciton into electron and holes.

PSC was seen as quantum dots sensitizing mp-TiO₂ during the first approaches of this technology [30], [31]; however, currently it has been established as semiconductor where transport of charges happens in the bulk of perovskite as well.

Based on previous classification and the generation they belong to, a conceptual scheme is presented in Figure 1.3 including all PV technologies.

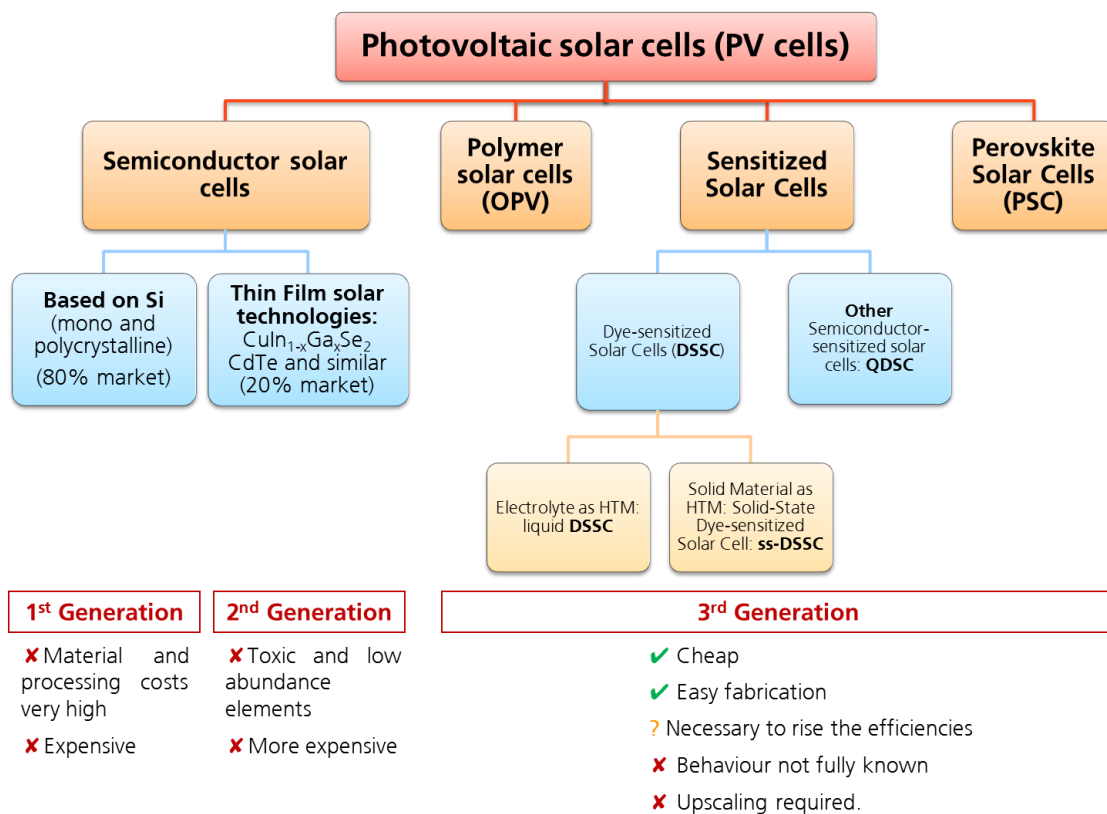


Figure 1.3. Scheme of the different generations of PV showing the different types included in each category.

1.2 Solar Cell Characterization

1.2.1 Solar spectra

Sun irradiance is not homogeneous over Earth surface. Hence, the selection of the appropriated solar spectra adequate to test the PV devices is a key step in the subsequent evaluation and comparison of the solar cells. To compare results and extract conclusions from parts of the world with different irradiance, an international standard is needed. The standard used is made by American Society for Testing and Materials (ASTM).

Air Mass Zero spectra (AM0) is considered as the extraterrestrial irradiance *i.e.* the irradiance at the top of the atmosphere (black line in Figure 1.4). It is worthy to say AM0 correlates quite well with the black body irradiation at 5800 K. 1366.1 W m^{-2} is given by the total integrated irradiance of this spectrum. AM0 irradiance spectrum is reported in ASTM E-490.

Once light has reached the atmosphere, a part is attenuated by the absorption and scattering before attaining terrestrial surface. UV and visible light is absorbed by ozone (O_3) and oxygen (O_2), near infrared by nitrous oxide (N_2O) and methane (CH_4) while carbon dioxide (CO_2) and water (H_2O) absorb both in near and far infrared. Another factor to take in consideration is the angle of incidence of incoming light which depends on the latitude and the moment of the day. To standardize it, the concept air mass (AM) is applied. AM is the optical path length through the atmosphere (L) normalized by the path length vertically upwards *i.e.* the zenithal one (L_0). Accordingly, AM is calculated as:

$$AM = \frac{L}{L_0} \approx \frac{1}{\cos(\theta)} \quad (1.1)$$

Where θ is the angle formed between the zenith and the shortest path direction of incoming sun light. ASTM G-173-03 establishes an angle of 48.19° giving $AM=1.5$. Furthermore, for this standard, both direct and diffuse light is considered giving 1000.4 W m^{-2} for AM1.5G. If no more information is specified, AM1.5G will be the sun irradiance standard employed in this whole work. AM0 and AM1.5G are depicted in the following Figure 1.4 showing the reduction caused by absorption of atmospheric gases.

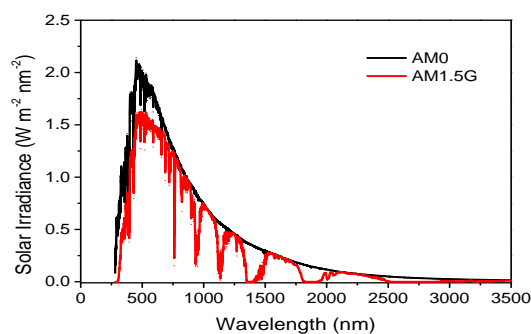


Figure 1.4. Solar irradiance spectra AM0 and AM1.5G extracted from ASTM E-490 and ASTM G-173-03 respectively.

1.2.2 I - V characteristics

The most representative test for any type of PV solar cell is the study of current-voltage characteristics, (I - V curve). It is based on the definition of a solar cell as a device that generates both current and voltage without any external source while it is illuminated. Consequently, a solar cell can be represented using double diode model due to its lack of ideality where a current source (I_L) connected in parallel with two diodes (Diode 1: $m=1$, $I_0=I_{01}$; Diode 2: $m=2$, $I_0=I_{02}$), to generate a voltage (V). However, there are some parasitic resistances such as shunt (R_{SH}) and series (R_S) resistances which limit the performance of solar cells. R_{SH} is the result of undesirable charge recombination mechanisms while R_S is the result of taking into account resistance at the interfaces, resistance in the bulk materials due to its own lack of conductivity and the sheet resistance comes from the glass transparent substrate. Subsequently, in an ideal device, $R_{SH} \rightarrow \infty$ since no parasitic current should be lost through the parallel branch and $R_S \rightarrow 0$ because losses by resistivity of materials and contacts are minimized. The equivalent circuit for a solar cell considering double diode model with R_{SH} and R_S is represented in Figure 1.5.

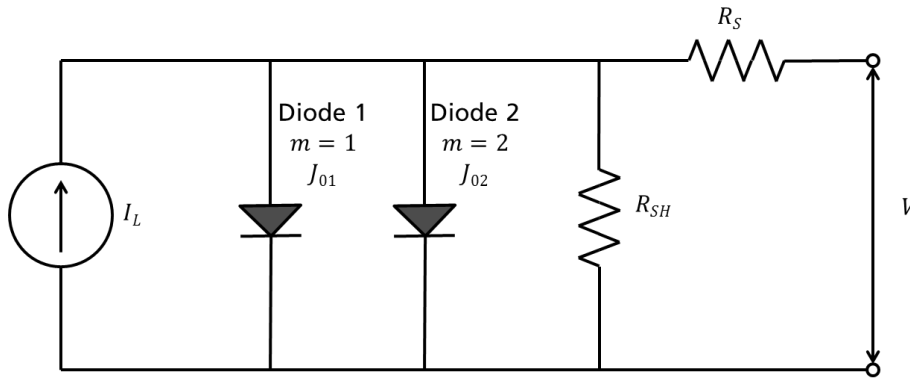


Figure 1.5. Equivalent circuit for a PV solar cell using double diode model.

Thus, the current flowing in PV solar cell can be expressed [39], [40]:

$$I = I_L - I_D - I_{SH} \quad (1.2)$$

Where I_L is the light generated current originated by absorbed photons, I_D is the dark current which corresponds with diode current and I_{SH} is the shunt current that matches with the current losses through the parallel branch.

- Latter term of equation 1.2: I_{SH} , can be defined considering the previous equivalent circuit by:

$$I_{SH} = \frac{V+IR_S}{R_{SH}} \quad (1.3)$$

When $R_{SH} \rightarrow \infty$, equation 1.3 is annulled.

- Dark current term (I_D) corresponds with double diode equation model:

$$I_D = I_{01} \left\{ \exp \left[\frac{q(V+R_S)}{k_B T} \right] - 1 \right\} - I_{02} \left\{ \exp \left[\frac{q(V+R_S)}{2k_B T} \right] - 1 \right\} \quad (1.4)$$

Where I_{01} and I_{02} are the corresponding dark saturation diode currents for diodes with ideality factor 1 and 2 respectively, T is the temperature in K, q is the elementary charge constant and k_B is Boltzmann constant. The effect of both diodes can be expressed in only one equation if a global ideality factor (m) is defined. In this case ideality factor is comprised $1 < m < 2$, so equation 1.4 can be simplified to:

$$I_D = I_0 \left\{ \exp \left[\frac{q(V+R_S)}{mk_B T} \right] - 1 \right\} \quad (1.5)$$

In addition, when $R_S \rightarrow 0$, equation 1.5 is transformed into:

$$I_D = I_0 \left\{ \exp \left[\frac{qV}{mk_B T} \right] - 1 \right\} \quad (1.6)$$

- Finally, taking into account both $R_{SH} \rightarrow \infty$ and $R_S \rightarrow 0$, light generated current (I_L) can be approximated as:

$$I_L = I_{SC} \quad (1.7)$$

To summarize, counting equations 1.3 and 1.4, equation 1.2 which represents current flowing through a solar cell (I) can be expressed as:

$$I = I_L - I_{01} \left\{ \exp \left[\frac{q(V+R_S)}{k_B T} \right] - 1 \right\} - I_{02} \left\{ \exp \left[\frac{q(V+R_S)}{2k_B T} \right] - 1 \right\} - \frac{V+IR_S}{R_{SH}} \quad (1.8)$$

If all simplifications are considered: $R_{SH} \rightarrow \infty$, $R_S \rightarrow 0$ and agglutination of ideality factor, equation 1.8 is simplified to:

$$I = I_{SC} - I_0 \left\{ \exp \left[\frac{qV}{mk_B T} \right] - 1 \right\} \quad (1.9)$$

For research purposes, the total photogenerated current (I) results less informative than current density (J) because J is normalized by area giving a result independent of the solar cell size, extracting more valuable information from material properties point of view. So, equation to 1.9 can be replaced by its analogous:

$$J = J_{SC} - J_0 \left\{ \exp \left[\frac{qV}{mk_B T} \right] - 1 \right\} \quad (1.10)$$

Moreover, under short-circuit conditions; both equations 1.9 and 1.10 are annulled: $I = J = 0$ and $V = V_{OC}$. From those equations 1.9 and 1.10 can be obtained:

$$V_{OC} = \frac{mk_B T}{q} \ln \left(\frac{I_{SC}}{I_0} + 1 \right) = \frac{mk_B T}{q} \ln \left(\frac{J_{SC}}{J_0} + 1 \right) \quad (1.11)$$

On the other hand, a schematic image showing a typical J - V curve is showed in Figure 1.6. It can be observed as R_{SH} decreases, the curve becomes less horizontal at low voltages while as R_S increases the J - V curve is turned into less vertical at high voltages.

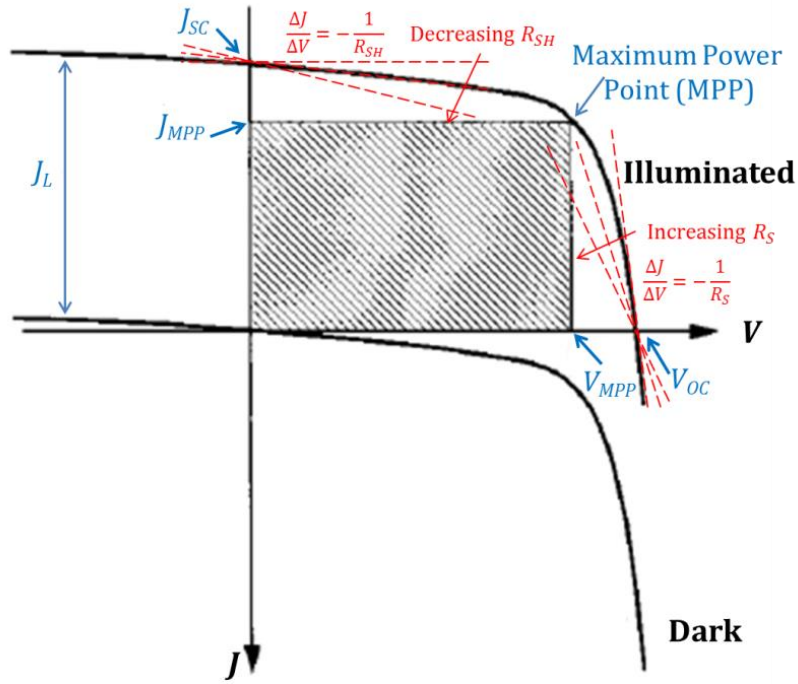


Figure 1.6. Schematic J - V curve representation. Adapted from Sze, S.M. and Ng, K.K. in *Physics of Semiconductor devices*, Wiley [41].

The overall efficiency of any solar cell is given by the ratio of the maximum power out achieved divided by the incoming light power (see equation 1.13). A quality parameter so-called fill factor (FF) is defined to characterize the *square-ness* of the J - V curve. Mathematically, FF is the ratio between maximum PCE divided by the theoretical maximum efficiency without any type of shunt, series or recombination losses or, *i.e.* the product of V_{OC} by J_{SC} .

$$FF = \frac{PCE}{V_{OC} J_{SC}} = \frac{J_{MPP} V_{MPP}}{J_{SC} V_{OC}} \quad (1.12)$$

Considering the previously defined fill factor, PCE of a solar cell can be expressed in percentage like:

$$PCE (\%) = \frac{P_{out}}{P_{in}} 100 = \frac{V_{MPP} J_{MPP}}{P_{in}} 100 = \frac{J_{SC} V_{OC} FF}{P_{in}} 100 \quad (1.13)$$

Where P_{in} is fixed to $100 \text{ mW cm}^{-2} = 1000 \text{ W m}^{-2}$ according AM1.5G.

1.2.3 Incident Photon-to-Current Efficiency (IPCE)

Incident photon-to-current efficiency (IPCE), also known as Incident photon-to-converted electron efficiency, is a measurement of the ratio of incident photons they are converted into electrons inside a PV device. A schematic draw of a typical IPCE is depicted in Figure 1.7.

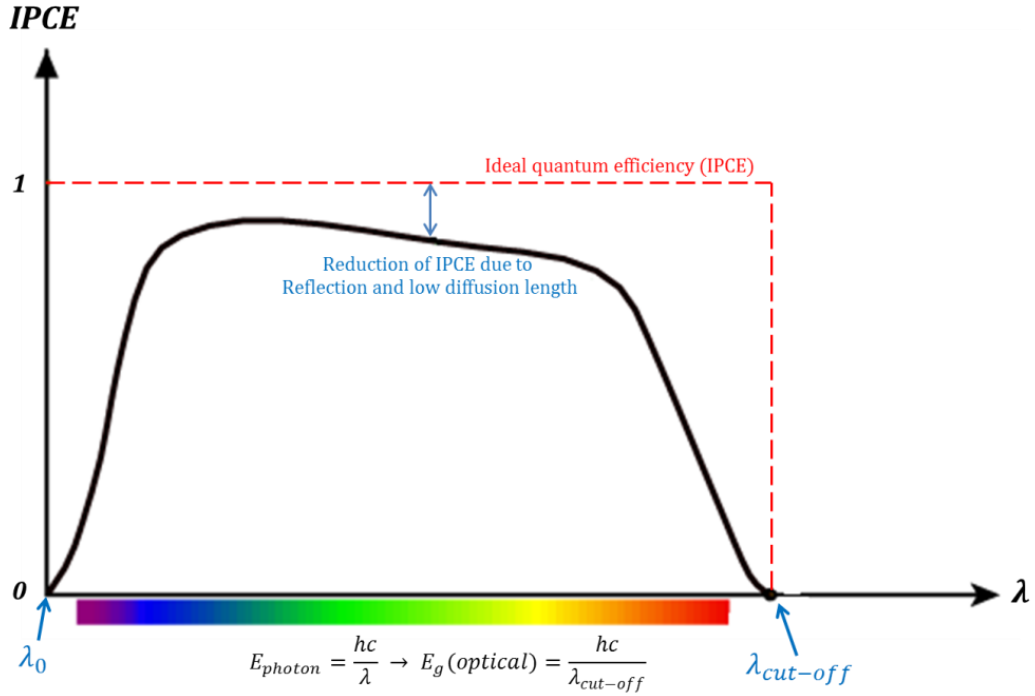


Figure 1.7. Schematic representation of IPCE curve.

The fundamental of this technique consist on measuring the quantum efficiency, *i.e.* the ratio of incident photons are converted into collected electrons at each wavelength (see equation 1.14). Hence, IPCE gives an idea of which part of the spectra is more efficiently absorbed and collected.

$$IPCE(\lambda) = \frac{hc}{q} \frac{J_{SC}(\lambda)}{\lambda P_{in}(\lambda)} = \frac{\text{collected } e^{-}(\lambda)}{\text{incident photons}(\lambda)} \quad (1.14)$$

Where h is the Planck constant, c is the speed of light, q is the elementary charge, λ the applied wavelength whereas $J_{SC}(\lambda)$ and $P_{in}(\lambda)$ are the short-circuit current generated and the power incident at each wavelength respectively.

The characterization of quantum efficiency makes possible not only to differentiate how many incident photons are really converted into electrons, but also which is the minimum photon energy where absorbers are excited to harvest light. This minimum energy gap is calculated as the photon energy for the cut-off wavelength (using equation 1.15) and corresponds with the optical bandgap.

$$E_{\text{photon}} = \frac{hc}{\lambda} \rightarrow E_g(\text{optical}) = \frac{hc}{\lambda_{\text{cut-off}}} \cong \frac{1240}{\lambda_{\text{cut-off}}(\text{nm})} (\text{in eV}) \quad (1.15)$$

The area under the IPCE curve is proportional to the total current density under illumination (J_L), that can be correlated with short-circuit current density (J_{SC}) as it was explained in the previous section. Therefore, the expected J_{SC} can be obtained by integration of equation 1.16 being used to cross-check the result attained by $J-V$ characterization.

$$J_{SC} = \int_{\lambda_0}^{\lambda_{\text{cut-off}}} q IPCE(\lambda) \Phi(\lambda) d\lambda \quad (1.16)$$

Where λ_0 is the more energetic (minimum) wavelength absorbed by the solar cell, $\lambda_{cut-off}$ the less energetic (maximum) one, while $\Phi(\lambda)$ is the photon flux at each wavelength.

Finally, IPCE can be considered as a global measurement of different individual processes such as: light harvesting, injection and collection of electron. Then, IPCE is the product of those individual processes and it can be expressed as following:

$$IPCE(\lambda) = LHE(\lambda) \eta_{inj}(\lambda) \eta_{col}(\lambda) \quad (1.17)$$

Where $LHE(\lambda)$ is the light harvesting efficiency, while $\eta_{inj}(\lambda)$ and $\eta_{col}(\lambda)$ are the injecting and collecting efficiencies respectively.

1.3 PSC principles

PSC are the most recent addition in 3rd generation PV technology. Perovskites with PV interest are normally based on non-natural organo-metal(II) halides. These perovskites ensure both crystal, optical and electronic properties interesting to be used in solar cells. In this section perovskite properties will be detailed and explained focusing in the properties with special interest for PV applications.

1.3.1 Perovskite: basics and general description

Perovskites were discovered by Gustav Rose in 1839 when he found calcium titanate (CaTiO_3) in samples from Ural Mountains [42]. This mineral was named in honor of the famous Russian mineralogist Lev Perovski. After that, the name perovskite has been extended to any compound with formula: ABC_3 and crystal structure analogous to CaTiO_3 one.

Generally, most studied perovskites are oxides where C is oxygen B is a tetravalent metal and A is a divalent cation: ABO_3 . Oxide perovskites is a wide group with interesting and peculiar electrical properties induced by perovskite crystal structure such as piezoelectricity, ferroelectricity, ferromagnetism, multiferroicity, ionic conductivity or superconductivity [43].

Later, Mitzi and coworkers at IBM Research Center, developed varieties of synthetic hybrid organic-inorganic perovskite halides using metals like tin (Sn) or lead (Pb) for diverse electronic applications such as $(\text{C}_{20}\text{H}_{22}\text{S}_4\text{N}_2)\text{PbCl}_4$ for light emitting diodes (LEDs) and $(\text{C}_6\text{H}_5\text{C}_2\text{H}_4\text{NH}_3)_2\text{SnI}_4$ for transistors [25]–[29]. Note that general formula for halide perovskites (ABX_3) has slightly changed to $(\text{R-NH}_3)_2\text{BX}_4$ or $(\text{NH}_3\text{-R-NH}_3)\text{BX}_4$ since layered perovskite structures are expected, *i.e.* alternating inorganic and organic sections inside the perovskite bulk due to the large size of the organic cation. The number of sections and the separation between them can be tuned by changing the size of the organic cation, modifying the band gap as consequence [29]. When a very small organic cation is introduced in the perovskite, discontinuities in the perovskite structure are not created, so changes in the bandgap are not possible by quantum confinement forming a normal ABX_3 perovskite. To summarize, Mitzi's work includes several synthetic hybrid organic-inorganic perovskites with organic cations (A^+) such as $\text{C}_4\text{H}_9\text{NH}_3^+$, $\text{C}_6\text{H}_5\text{C}_2\text{H}_4\text{NH}_3^+$ or $\text{C}_{20}\text{H}_{22}\text{S}_4\text{N}_2^+$; while Pb^{2+} , Sn^{2+} are the principal metal +2 cations although other

metal cations can be also found (Cu^{2+} , Ni^{2+} , Co^{2+} , Fe^{2+} , Mn^{2+} , Cr^{2+} , Pd^{2+} , Cd^{2+} , Ge^{2+} , Eu^{2+} , Yb^{2+}) and Cl^- , Br^- and I^- as halogens [26], [29]. In spite of many working principles, characterization and properties were reported by Mitzi's group, perovskites were not applied in photovoltaic solar cells.

Perovskite absorbers for PV applications are synthetic hybrid organic-inorganic lead or tin halide based compounds with general formula ABX_3 , where A are organic cations either methylammonium (MA , CH_3NH_3^+) or formamidinium (FA , $\text{NH}_2\text{-CH=CH}_2^+$), B is Pb^{2+} or Sn^{2+} , and X is a halogen: Cl^- , Br^- or I^- . First approaches using perovskite photovoltaics employed methylammonium lead iodide ($\text{CH}_3\text{NH}_3\text{PbI}_3$) as harvester [30], [31], [35]. After that, both MA-FA [44]–[46] and Br-I [47], [48] mixtures were created to vary the light harvesting properties and bandgap conferring respectable properties as PV absorber. On the other hand, although tin based perovskites were reported [46], [49], [50], the poor PV properties, having a maximum PCE of only 6% reported [50]. In addition, the poor reproducibility and extreme moisture sensitivity on Sn halide perovskites make them less important materials to focus.

1.3.2 Perovskite Crystal Structure

In previous section, the general formula for perovskites: ABX_3 was discussed. However, to form a perovskite it is necessary not only having that stoichiometry but also presenting a crystal structure similar to the first discovered perovskite: CaTiO_3 .

Therefore, in an ideal symmetric cubic perovskite structure, B cation is placed in a 6-fold coordination (BX_6) surrounded by an octahedron of anions, and the A cation in 12-fold cuboctahedral coordination. Furthermore, an essential requirement to form a perovskite, A cation must be larger than B one (Figure 1.8a and 1.8b for the detail of the 12-fold cuboctahedral coordination of A cation).

The relative size of ions and distances between them determine the final crystal structure, since either octahedral rotations or B cation displacement are common deviations from ideal cubic perovskite structure. Those deviations from ideal cubic system define many of the perovskite properties, principally the electronic and magnetic ones. In order to characterize the structure of a perovskite material, two parameters are established: tolerance factor (t) and octahedral factor (μ). Tolerance factor is a magnitude firstly proposed by Goldschmidt [51] to quantify the stability and distortion of crystal structures as a function of ionic radii (equation 1.18). If $t > 1$ perovskite structure is not presented, because A cation is too big or B cation too small forming normally hexagonal crystal structures; when $t < 1$, perovskite presents octahedral rotations; for $t \sim 1$ perovskite tends to form cubic structures and, finally, when A and B cations have similar size, $t < 0.71$ creating non-perovskite like structures, frequently trigonal crystal ones.

$$t = \frac{R_A + R_X}{\sqrt{2}(R_B + R_X)} \quad (1.18)$$

However, for certain types of perovskites, tolerance factor is not enough to predict the stability of the structure. Therefore, Li *et al.* proposed the introduction of octahedral factor (μ) [52] to complement the explanation of stability of perovskite

structures with ABX_3 formula regarding their ionic radii (equation 1.19). Therefore, when halide perovskites (ABX_3) with tolerance factor comprised between $0.71 < t < 1$, also require an octahedral factor of $0.41 < \mu < 0.732$ for the stability of perovskite crystal structure.

$$\mu = R_B/R_X \quad (1.19)$$

Considering organic-inorganic hybrid perovskites halides with PV interest, ionic radii of different ions are [53]:

- $R_A=0.18$ nm for methylammonium (MA), 0.23 nm for ethylammonium (EA) and 0.19-0.22 nm in the case of formamidinium (FA).
- $R_B=0.119$ nm for Pb^{2+} and 0.110 nm for Sn^{2+} .
- $R_X=0.181$ nm for Cl^- , 0.196 nm for Br^- and 0.220 nm in the case of the most extended I^- .

Consequently, the crystal structure of typical $CH_3NH_3PbI_3$ ($t=0.834$ and $\mu=0.541$) corresponds with a stable perovskite with octahedral rotations and the organic linear methylammonium cation in the center as it is depicted in Figure 1.8c. Other stable perovskites with possible PV interest such as are included in Figure 1.8d.

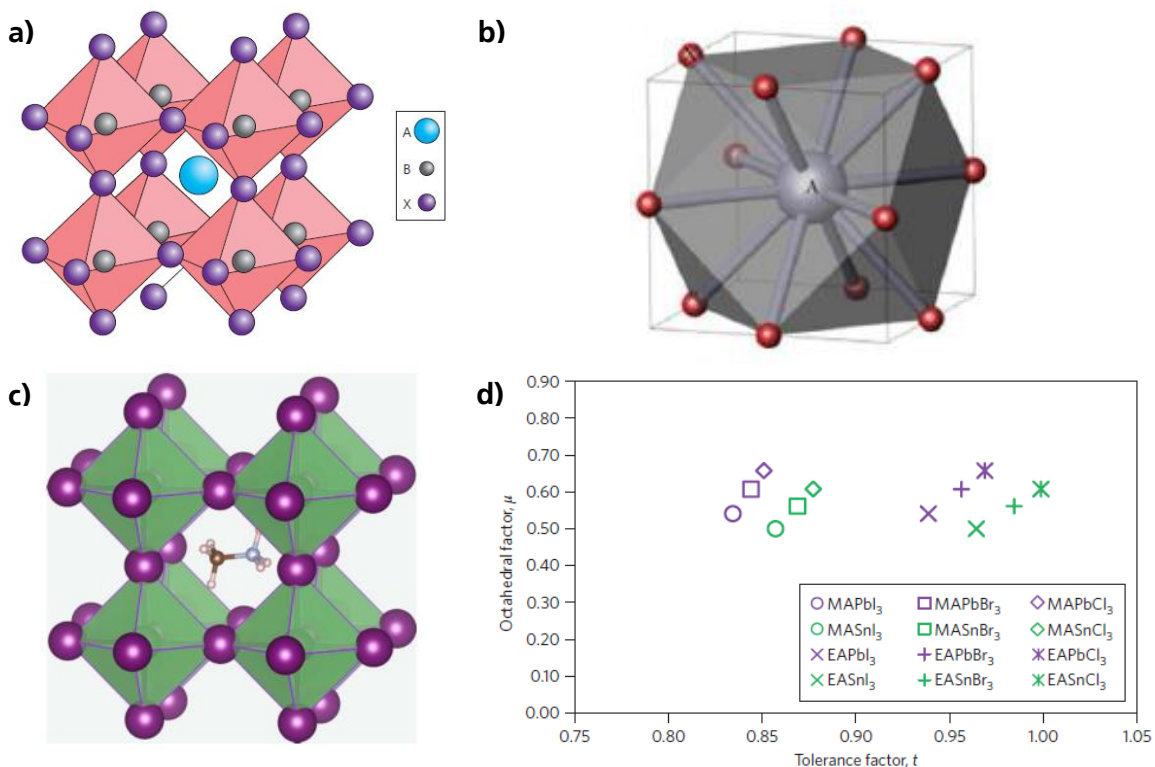


Figure 1.8. a) Ideal cubic-symmetry perovskite structure with ABX_3 formula. Taken from Eames, C. *et al.* [54], b) detail of the 12-fold cuboctahedral coordination for the A cation in a ABX_3 perovskite. Extracted from Gao, P. *et al.* [55], c) structure of $CH_3NH_3PbI_3$ showing octahedral rotations and the linear methylammonium cation in the center. Also from Eames, C. *et al.* [54] and d) tolerance (t) and octahedral factors (μ) for different perovskites with photovoltaic interest. From Green *et al.* [53].

On the other hand, a point group that includes an inversion center as one of its symmetry elements is called centrosymmetric [56]. Certain perovskite materials, such as BaTiO_3 and PbTiO_3 are not centrosymmetric due to B cation displacement. For non-centrosymmetric perovskite materials, *e.g.* the above-mentioned BaTiO_3 and PbTiO_3 , B-site off-centering drives ferroelectric behavior. Generally, ferroelectricity is only present in perovskites with $t \sim 1$, since it is reduced by A-site antipolar movement in perovskites as octahedral rotations increases (when t is reduced) [43]. Nevertheless, octahedral rotations are not responsible by itself of ferroelectric suppression, since some perovskites show ferroelectric behavior together with octahedral rotations (*e.g.* GdScO_3 or CaZrO_3). Actually, it is the A-site displacements that accompany the octahedral rotations which produce the decisive role in suppressing ferroelectricity [43]. B-displacement has not been shown in organic-inorganic lead halide perovskite family (APbX_3) due to their ionic radii of their components. So, theoretically, ferroelectricity driven by B-site off-centering is not possible as usual. Moreover, authors reported complete absence of ferroelectricity in hybrid lead halides showing only remarkable polarization using piezoelectric force microscopy (PFM) [57]. However, for perovskites for PV interest, it becomes much more complex to analyze this phenomenon since A cation is not represented as a point in the space but a linear structure. Hence, in some reports, A is represented as a dipole which causes ferroelectricity [58].

Regarding the effects of temperature on crystal structure, different perovskite phases are expected, being α -phase the high temperature one, and then other β and γ phases are formed as temperature is decreased. Depending on the type of organic cations and halide anions employed in the perovskite synthesis variations in crystal phases are expected.

First approach studying temperature dependence of crystal lattice for methylammonium lead halides was accomplished by Poglitsch and Weber [59]. In this study, three different phases were distinguished for $\text{CH}_3\text{NH}_3\text{PbI}_3$ perovskite: a cubic $Pm\bar{3}m$ α - $\text{CH}_3\text{NH}_3\text{PbI}_3$ over 54°C , a tetragonal $I4/mcm$ β - $\text{CH}_3\text{NH}_3\text{PbI}_3$ between 54°C and -111°C , and orthorhombic $Pna2_1$ γ - $\text{CH}_3\text{NH}_3\text{PbI}_3$ phase for temperatures lower than -111°C . More recent works done by Stoumpos *et al.* [60] disclosed similar tendency, however α phase is based on not perfectly cubic but an almost cubic $P4mm$ tetragonal space group $>50^\circ\text{C}$ (57°C according Baikie *et al.* [61]), while β - $\text{CH}_3\text{NH}_3\text{PbI}_3$ is reported as tetragonal $I4cm$ for $-111^\circ\text{C} < T < 50^\circ\text{C}$ and orthorhombic γ - $\text{CH}_3\text{NH}_3\text{PbI}_3$ lower than that temperature.

One important consideration is at room temperature, PV active β -phase is present, however on increase in temperatures such as 60°C , which is a normal working temperature for any PV technology, active β -phase is transformed into α - $\text{CH}_3\text{NH}_3\text{PbI}_3$. Thus the, implementation in future industrial methods, could imply heat sink systems design. The introduction of compositional engineering utilizing other types of perovskites, can limit or even avoid this potential issue. For example, $\text{HC}(\text{NH}_2)_2\text{PbI}_3$ exhibit a PV active trigonal α -phase ($P\bar{3}m1$) for $T > -73^\circ\text{C}$, another trigonal β - $\text{HC}(\text{NH}_2)_2\text{PbI}_3$ ($P3$) for $-143^\circ\text{C} > T > -73^\circ\text{C}$ and orthorhombic γ - $\text{HC}(\text{NH}_2)_2\text{PbI}_3$ below -143°C . It is noticeably that for temperatures lower than 87°C in the presence of solvents, a non-perovskite like yellow compound δ - $\text{HC}(\text{NH}_2)_2\text{PbI}_3$ with hexagonal structure ($P6_3mc$) is formed inside the mother liquor [60], [62].

A summary of different cubic lattice parameters and the distances between ions in the perovskite crystal structure is presented in Table 1.1 showing very similar parameters independently the technique employed for the measurements.

Table 1.1. Crystal structure parameters for cubic (pseudocubic) α -CH₃NH₃PbI₃ phase.

Reference	Technique employed	Cubic lattice parameter (Å)	I-I separation (Å)	Pb-I bond length (Å)	C-N bond length (Å)	C-H bond length (Å)	N-H bond length (Å)
Poglitsch, A. and Weber, D. J. Phys. Chem. (1987) [59]	Dispersive polarizing millimeter-wave interferometer	6.3285	-	-	-	-	-
Kawamura, <i>et al.</i> J. Phys. Soc. Jpn. (2002) [63]	X-Ray diffraction	6.29	-	-	-	-	-
Baikie, T. <i>et al.</i> J. Mater. Chem. A (2013) [61]	X-Ray diffraction	6.28	-	-	-	-	-
Stoumpos, C. C. <i>et al.</i> Inorg. Chem. (2013) [60]	X-Ray diffraction	6.31	4.46	3.16	1.48	-	-
Weller, M. <i>et al.</i> Chem. Commun. (2015) [64]	Neutron diffraction	6.32	4.47	3.16	1.35	0.99	0.99
Eames, C. <i>et al.</i> Nat. Commun. (2015) [54]	DFT	6.28	4.45	3.16	1.48	1.1	1.04

1.3.3 Optical properties

Hybrid organic-inorganic perovskites shows very strong absorption properties in the UV-visible part of spectra. From past PV approaches [30], [31] to more recent developments [36], [65] incident photon-to-current efficiencies (IPCE) of PSC showed outstanding light harvesting and collecting capabilities to take maximum profit from the incident photons along its whole absorption spectra.

In addition to its excellent absorption, the value of the optical bandgap is another key parameter to explain the exceptional behavior in the PSC. Earlier studies were developed explaining the optimum band gap to maximize final PCE is ~1.5eV [66]–[68] which matches with hybrid organic lead halide perovskites. Moreover, perovskite bandgap is a direct band gap, [69] thus no crystal momentum (k-vector) is required for photon absorption.

In more recent works, optical band gap configuration of $\text{CH}_3\text{NH}_3\text{PbI}_3$ forming a continuous media (*i.e.* 3-dimensional perovskite) has been proposed, showing the valence band is formed by Pb6s-I5p sigma σ -antibonding orbital while conduction band consists on Pb6p-I5s σ -antibonding and Pb6p-I5p π -antibonding orbitals [69], [70], as it is represented in Figure 1.9. However, in recent contributions even a more complex distribution was suggested, since two valence bands were found [71]–[74] or even an excited charge transfer state over the conduction band [75].

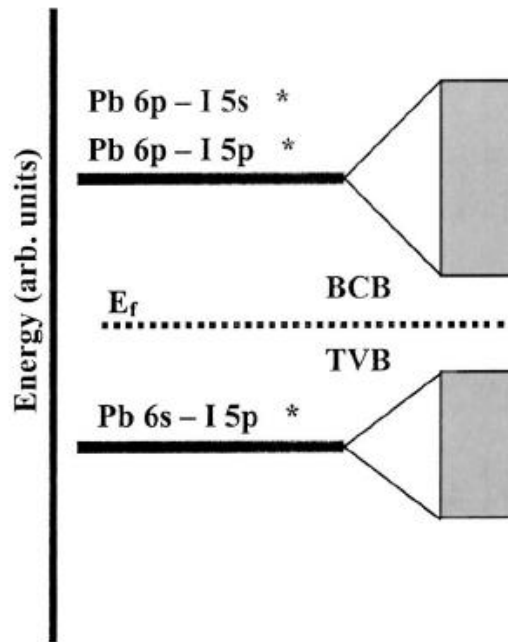


Figure 1.9. Bonding diagram of 3-dimensional $\text{CH}_3\text{NH}_3\text{PbI}_3$ crystal, showing the valence band (VB) and conduction band (CB) orbitals. Adapted from Umebayashi, T. *et al.* [69].

Furthermore, optical bandgap tuning has been a topic with an increasing interest. Modifications in bandgap were achieved principally by two ways: varying MA-FA ratio and I-Br ratio. With the control over methylammonium-formamidinium ratio, an extension into the near infrared absorption spectra was achieved since the onset was displaced from ~ 780 nm to over 800 nm [44]. The variation of iodide-bromide composition contributes not only with the optical band gap variation, but also with open circuit voltage and perovskite color tuning [47]. Therefore, perovskite compositional control has been demonstrated as an effective technique to improve optical properties, and then overall PV behavior in PSC [36], [65], [76].

Finally, other optical characterization findings showed absorption spectra is divided into Beer-Lambert (until ~ 525 nm) and cavity regions (from ~ 525 nm to cut-off wavelength) [77] and the justification of a capping layer also for mesoporous based configuration in order to achieve high efficiency solar cells [78].

1.3.4 Electronic properties and charge recombination

On light illumination on the perovskite absorber, incident photons gets excited, an electron-hole pair called exciton is formed. The required energy to split that exciton into separated electron and hole charges is named as binding energy (E_b). Regarding E_b , excitons are normally divided in two categories: Frenkel excitons and Mott-Wannier ones.

Frenkel exciton are normally presented in low permittivity systems where screening of charges are not significant, so columbic interactions are important producing excitons with small radius difficult to break, so when E_b is high (from 100-1000 meV); Frenkel excitons are usual in OPV systems. In contrast, Mott-Wannier excitons are distinctive from semiconductors, since they are presented in high permittivity media where screening effects reduce the columbic interactions creating much bigger and then, much easier to break excitons; therefore, E_b in these PV systems is lower than Frenkel ones but higher than thermal energy: $k_B T$ (typically around tens of meV but lower than 100 meV).

Binding energies for several types of hybrid organic-inorganic lead halide perovskites are reported in Table 1.2. In layered perovskites, *e.g.* $(C_9H_{19}NH_3)_2PbI_4$, $(NH_2C(l)=NH_2)_3PbI_5$ $(CH_3NH_3)_4PbI_6 \cdot 2H_2O$, binding energies are high, showing E_b values typical for Frenkel excitons. In contrast, for methylammonium lead halides, E_b are much lower but, discrepant. Most of the reported values for $CH_3NH_3PbI_3$ are consistent with Mott-Wannier excitons ($k_B T < E_b < 100$ meV). However, in some reports it is advised the mechanism could be non-excitonic due to the very low value of E_b and nature of perovskite [79], having a direct splitting into free charges (electrons and holes), just by thermal activation, *i.e.* when $E_b < k_B T$. Considering at 25°C, $k_B T=25.7$ meV, non-excitonic nature of perovskite is also supported in recent studies [77], [80].

Table 1.2. Binding energy (E_g) measured by different methods for different perovskite materials. Adapted from Sum, T. and Mathews, N. [81].

Reference	Perovskite	Dimensionality	Method	E_b (meV)
Koutselas, I.B. <i>et al.</i> J. Phys.: Condens. Matter (1996) [82]			Optical absorption	30
Hirasawa, M. <i>et al.</i> Physica B. (1994) [83]			Magneto-absorption	37
Ishihara, T. J. Lumin. (1994) [84]			Temperature dependent PL	45
Tanaka, K. <i>et al.</i> Solid State Commun. (2003) [85]	$\text{CH}_3\text{NH}_3\text{PbI}_3$	3D	Magneto-absorption	50
Sun, S. <i>et al.</i> Energy Environ. Sci. (2014) [80]			Temperature dependent PL	19 ± 3
D'Innocenzo, V. <i>et al.</i> Nat. Commun. (2014) [79]			Optical absorption	55 ± 20
Lin, Q. <i>et al.</i> Nature Photon. (2015) [77]			Optical absorption	~ 2
Tanaka, K. <i>et al.</i> Solid State Commun. (2003) [85]	$\text{CH}_3\text{NH}_3\text{PbBr}_3$	3D	Magneto-absorption	76
Koutselas, I.B. <i>et al.</i> J. Phys.: Condens. Matter (1996) [82]			Optical absorption	150
Zhang, W. <i>et al.</i> Nano Lett. (2013) [86]	$\text{CH}_3\text{NH}_3\text{PbI}_{3-x}\text{Cl}_x$	3D	Temperature dependent PL	98
Ishihara, T. J. Lumin. (1994) [84]	$(\text{C}_9\text{H}_{19}\text{NH}_3)_2\text{PbI}_4$	2D	Temperature dependent PL	≥ 330
Koutselas, I.B. <i>et al.</i> J. Phys.: Condens. Matter (1996) [82]	$(\text{NH}_2\text{C}(\text{l})=\text{NH}_2)_3\text{PbI}_5$	1D	Optical absorption	≥ 410
Koutselas, I.B. <i>et al.</i> J. Phys.: Condens. Matter (1996) [82]	$(\text{CH}_3\text{NH}_3)_4\text{PbI}_6 \cdot 2\text{H}_2\text{O}$	0D	Optical absorption	545

Another characteristics which make hybrid organic-inorganic lead halide perovskite interesting for PV purposes is their high mobility [87] and ambipolar conductivity *i.e.* perovskite can work for both transporting electrons and holes. Ambipolar behavior was demonstrated in initial studies, since Chung *et al.* employed a tin halide perovskite (CsSnI_3) as HTM in ss-DSSC exhibiting remarkable efficiency (PCE>10%) [22] proving *p*-type conduction for that compound. In addition, *p*-type conduction for $\text{CH}_3\text{NH}_3\text{PbI}_3$ based solar cells was validated by Etgar *et al.* using a PSC configuration without HTM [34]. Alternatively, Snaith and coworkers confirmed *n*-type conduction employing a non-injecting electron mesoscopic Al_2O_3 scaffold between anode and $\text{CH}_3\text{NH}_3\text{PbI}_3$, where perovskite was not only the absorbing material but also the responsible to transport electrons to anode.

After charges have been formed and separated, electrons and holes have to reach anode and cathode respectively. If during their path, electrons make contact with holes they recombine immediately resulting in losses since generated charges were

not collected at electrodes. Concentration of charges (both electrons and holes) with time is expressed by general continuity equation (equation 1.20)

$$\frac{d\rho_N}{dt} = G - k_1\rho_N + k_2\rho_N^2 + k_3\rho_N^3 \quad (1.20)$$

Where ρ_N represents charge carrier density in number of particles per volume (either electrons or holes), meanwhile G is the charge generation term, $k_1\rho_N$, $k_2\rho_N^2$ and $k_3\rho_N^3$ are the terms related with monomolecular, bimolecular and trimolecular recombination mechanisms respectively.

An energy level diagram explaining different recombination mechanisms process is shown in Figure 1.10.

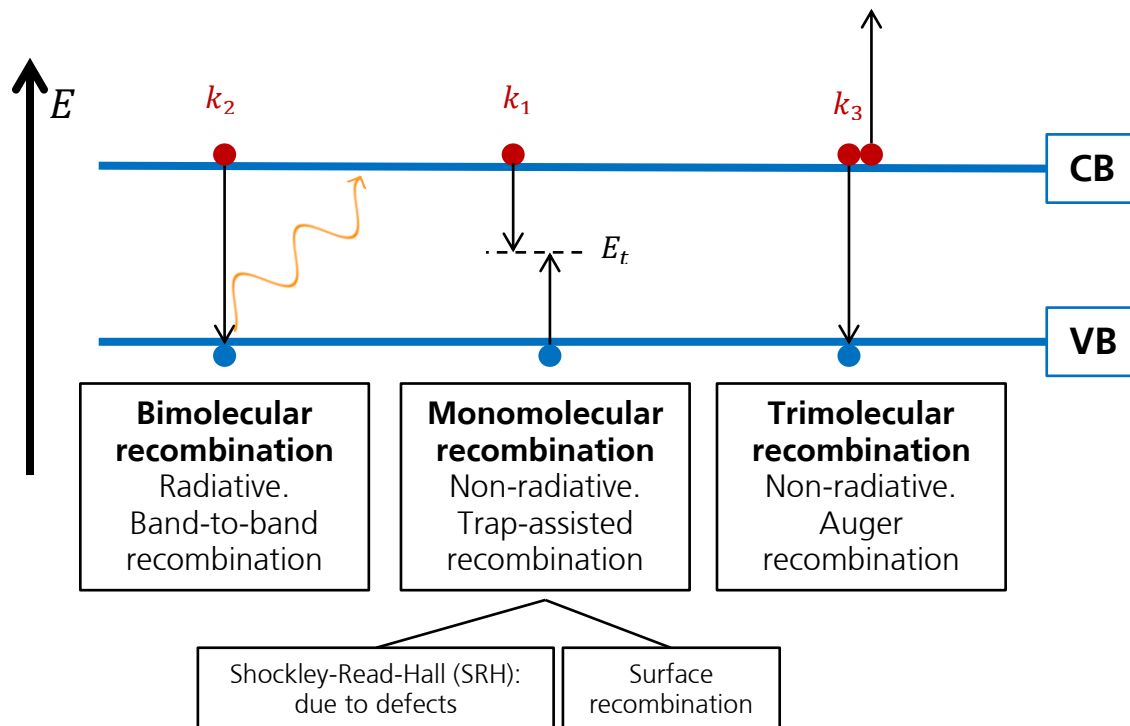


Figure 1.10. Energy level scheme for the different types of recombination mechanisms takes place inside a PSC.

Regarding recombination mechanisms, some differences can be recognized:

- **Monomolecular recombination** (k_1). Non-radiative trap-assisted recombination. It is principal mechanism in PSC [74], [88], [89]. Two different subtypes can be distinguished:
 - Shockley-Read-Hall (SRH) recombination: due to deep traps. It can be reduced controlling the morphology and grain boundaries inside the perovskite layer.
 - Surface recombination: traps at the interfaces. Very important in PSC
- **Bimolecular recombination** (k_2). A radiative due to band to band recombination. It is the desired, as it allows making the process reversible. It is function of the photoluminescence.

- **Trimolecular recombination** (k_3). It is also non-radiative. It is called Auger recombination and less important for PSC.

In Table 1.3 recombination rate constants (k_1 , k_2 and k_3) reported in literature for different perovskites calculated using optical pump THz probe (OPTP) spectroscopy are shown. Charge carrier mobility values were also included in this table. Type of perovskite, deposition method and architecture are detailed in below table for comparison.

Table 1.3. Summary of recombination rate constants and charge carrier mobilities for different hybrid organic-inorganic perovskites. Adapted from Johnston, M. and Herz, L. [90].

Reference	Type of perovskite	Deposition method. Architecture	Charge-carrier mobility ($\text{cm}^2 \text{V}^{-1} \text{s}^{-1}$)	Rate Constants		
				$k_1 \times 10^{-6}$ (s^{-1})	$k_2 \times 10^{10}$ ($\text{cm}^3 \text{s}^{-1}$)	$k_3 \times 10^{28}$ ($\text{cm}^6 \text{s}^{-1}$)
Wehrenfening <i>et al.</i> Adv. Mater. (2014) [88]	MAPbI _{3-x} Cl _x	Solution process. Perovskite over mp-Al ₂ O ₃	11.6	4.9	0.87	0.99
Wehrenfening <i>et al.</i> Energy Environ. Sci. (2014) [89] Wehrenfening <i>et al.</i> J. Phys. Chem. Lett. (2014) [91]		Vapor. Planar	33	12	1.1	0.2
Wehrenfening <i>et al.</i> Adv. Mater. (2014) [88]	MAPbI ₃	Solution process. Perovskite over mp-Al ₂ O ₃	8.2	14	9.2	1.3
Milot <i>et al.</i> Adv. Funct. Mater. (2015) [92]		Solution process. Planar	35	15	0.6	1.6
Rehman, W. <i>et al.</i> Adv. Mater. (2015) [93]	FAPbI ₃	Solution process. Planar	27	7	1.1	0.2
Piatkowski, P. <i>et al.</i> , J. Phys. Chem. Lett. (2016) [94] ^a		Solution process. Planar	40 - 75	0.000152	2.97	7.31
Rehman, W. <i>et al.</i> Adv. Mater. (2015) [93]	FAPbBr ₃	Solution process. Planar	14	21	11	1.5
Noel, <i>et al.</i> Energy Environ. Sci. [50]	FASnI ₃	Solution process. Perovskite over mp-TiO ₂	1.6	8	14	N.R.

^aIn this case OPTP Spectroscopy was employed in combination with Flash photolysis. N.R. Not Reported.

Previously, different processes which are taking place into the perovskite have been discussed, *i.e.* photoexcitation, generation of charges, charge carrier and recombination. A global summary of the different process inside PSC are detailed in Table 1.4. and Figure 1.11, considering TiO₂ as ETM and any HTM. Desirable

processes (green) were differentiated from undesirable ones (red): charge recombination and exciton annihilation.

Table 1.4. Summary of different desirable and undesirable processes into PSC containing TiO₂ as ETM and any HTM. Adapted from Marchioro, A. *et al.* [95].

Desirable process	Undesirable process
<p>0. Photoexcitation of perovskite Perovskite + $h\nu \rightarrow (e^{\cdot}\dots h^{\cdot})_{\text{perovskite}}$</p>	<p>3. Exciton annihilation via photoluminescence $(e^{\cdot}\dots h^{\cdot})_{\text{perovskite}} \rightarrow h\nu$</p>
<p>1. Electron injection into the TiO₂ conduction band $(e^{\cdot}\dots h^{\cdot})_{\text{perovskite}} \rightarrow e^{-}_{\text{CB}}(\text{TiO}_2) + h^{\cdot}(\text{perovskite})$ (1a) $h^{\cdot}(\text{perovskite}) \rightarrow h^{\cdot}(\text{HTM})$ (1b)</p>	<p>4. Non-radiative exciton annihilation $(e^{\cdot}\dots h^{\cdot})_{\text{perovskite}} \rightarrow \nabla$</p>
<p>2. Hole injection into HTM $(e^{\cdot}\dots h^{\cdot})_{\text{perovskite}} \rightarrow h^{\cdot}(\text{HTM}) + e^{-}(\text{perovskite})$ (2a) $e^{-}(\text{perovskite}) \rightarrow e^{-}_{\text{CB}}(\text{TiO}_2)$ (2b)</p>	<p>5. Recombination between electron from TiO₂ and hole from perovskite $e^{-}_{\text{CB}}(\text{TiO}_2) + h^{\cdot}(\text{perovskite}) \rightarrow \nabla$</p> <p>6. Recombination between hole from HTM and electron from perovskite $h^{\cdot}(\text{HTM}) + e^{-}(\text{perovskite}) \rightarrow \nabla$</p> <p>7. Interface TiO₂/HTM recombination $e^{-}_{\text{CB}}(\text{TiO}_2) + h^{\cdot}(\text{HTM}) \rightarrow \nabla$</p>

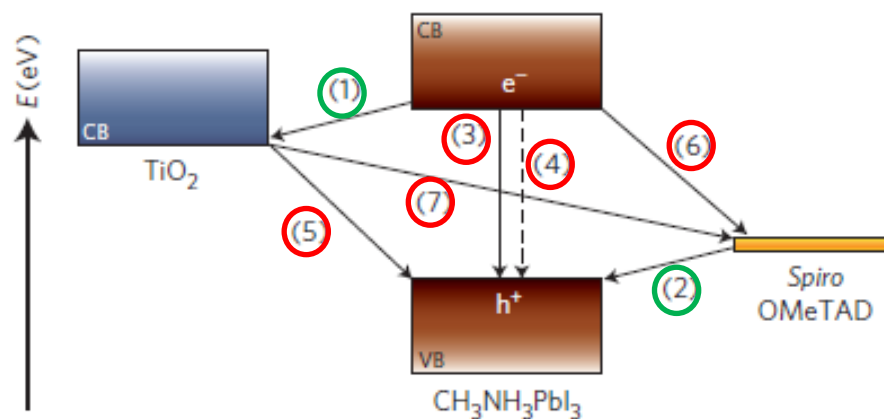


Figure 1.11. Summary of different desirable and undesirable processes into a PSC containing TiO₂ as ETM and Spiro-OMeTAD as HTM. Adapted from Marchioro, A. *et al.* [95].

Another issue which was observed in PSC was the presence of unbalanced charge distribution where electrons are not collected in a balanced way with holes at electrodes, since undesirable accumulation of charges, principally holes sit inside the perovskite capping layer not being extracted sufficiently [96].

As a result of different recombination processes presented, carrier lifetime and diffusion lengths were demonstrated to be ~ 1 micron in PSC [71], [72]. However, the microstructure employed has been revealed as an essential parameter in carrier lifetime enhancement [97].

On the other hand, some perovskite oxides such as LaMnO_3 or LaFeO_3 were proven as effective ionic conductors. Consequently, ion migration has been suggested in several works as the reason underlying several effects [44], [98]. However, ionic conduction in PSC have not been checked until recently [54], [99]. Eames *et al.* were able to evaluate defect formation energies, concluding iodide vacancies were much easier to be moved than any other ones, suggesting an excess of PbI_2 during perovskite synthesis in order to minimize issues derived from defect chemistry. Moreover, demonstration of $\text{CH}_3\text{NH}_3\text{PbI}_3$ as an effective mixed ionic-electronic conductor has been reported by several methods [54], [100]. The mixed conductivity nature of both $\text{CH}_3\text{NH}_3\text{PbI}_3$ and mixed $(\text{CH}_3\text{NH}_3)_{1-x}(\text{NH}_2\text{-CH=CH}_2)_x\text{PbI}_3$ was also confirmed by Yang *et al.* proposing ionic transport is even more important than electronic one inside perovskite materials [99].

Another noticeable phenomenon detected in PSC is the presence of hysteresis in J - V characterization curves. Hysteresis in PSC is the performance dependency of PV devices regarding the voltage sweeping direction. The first observation of hysteresis in PSC was noticed by Snaith and coworkers [101] and it has always been explained as an adverse effect. It is remarkable to mention in many cases, bad preconditioning, wrong measurement practices or extreme sweeping speeds were wrongly attributed to hysteresis effect [102], [103]. Hysteresis origin is still not fully clear. Principal hysteresis explanations were ascribed to undesirable traps in perovskite [104], ionic perovskite conduction [98], [105], [106] or even a mixture of them [107].

1.3.5 Device architecture

Any PV device, independently the type of technology employed or the final architecture prepared, consist of an absorber material placed in between the HTM and the ETM one; adjacent to the transporting materials, two electrodes must be placed, the anodic one next to the ETM and the cathodic next to the HTM, with the limitation that one of two electrodes has to be transparent to let the light come into the PV device. However, this five functional materials *i.e.* anode-ETM-Absorber-HTM-Cathode, could be condensed in less than five material layers if one material is able to wrap several functions at the same time or, in an opposed way, presenting more than five layers when a function is divided in two different materials. An example for the former case is silicon solar cell where between p - and n -type silicon absorption and transporting tasks are covered while for the latter case the combination of compact and mesoporous as ETM in DSSC or PSC can be considered as example.

Taking into account previous considerations, different alternatives can be implemented for PSC architecture:

- **Regular (n-i-p) vs inverted (p-i-n) configuration.** When *n*-type material is directly deposited onto transparent conducting oxide (TCO), making TCO working as anode, the configuration is named as regular one. It was the first one reported and the established criteria to refer them regarding electronic configuration was n-i-p configuration. Meanwhile, if TCO works as cathode due to *p*-type material was deposition onto it, the structure is called as inverted forming a p-i-n structure.
- **Mesoporous vs planar.** Regarding the morphology of the materials utilized two possibilities are differentiated. On the one hand, mesoporous scaffold where perovskite is infiltrated inside the inorganic oxide matrix to push up the absorption properties of the perovskite film. Moreover, two options could be utilized: injecting and non-injecting oxides as mesoporous scaffold. For injecting oxides, electrons can be injected and transported through the inorganic scaffold, *i.e.* the mesoporous film works both as scaffold and ETM, like in mesoporous titania (mp-TiO₂) or ZnO; when non-injecting oxides are employed, mesoporous structure is only working as scaffold since the mismatching between perovskite-inorganic oxide conduction bands blocks the e⁻ injection, as it is described for ZrO₂ [108] or Al₂O₃ [33]. On the other hand, for planar structures, perovskite is sandwiched between hole and electron extracting non-porous layers. flat

Combining all possibilities, four basic conceptual architectures can be used for PSC fabrication, n-i-p configuration with mesoporous structure which was the first reported design, p-i-n mesoporous and both types of planar configurations (regular and inverted). A scheme with the different types of PSC architectures are shown in Figure 1.12.

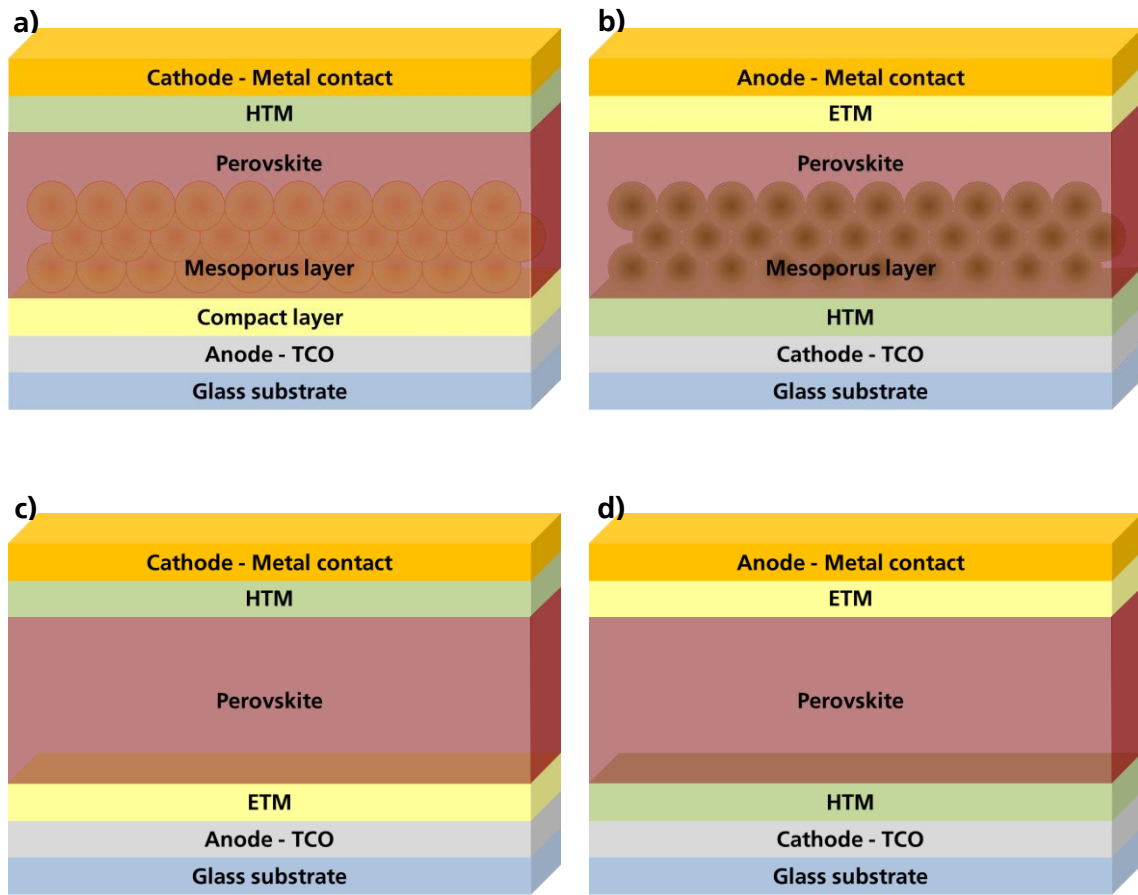


Figure 1.12. Different schematic device configurations employed for PSC fabrication, a) regular (n-i-p) mesoporous configuration, b) inverted (p-i-n) mesoporous architecture, c) regular (n-i-p) planar structure and d) inverted (p-i-n) planar one.

Originally, the first architecture prepared using PSC were based on DSSC, so regular architectures were the first ones divulged. Furthermore, in early approaches, the function of HTM layer was covered by liquid electrolytes [30], [31]. The implementation of solid HTMs in mesoporous regular structures during 2012 [32], [33] gave the breakthrough which impulse PV properties and behavior to revolutionize the field of emerging PV technologies. Inverted planar alternatives were developed placing p -type conducting polymer Poly(3,4-ethylenedioxythiophene)-poly(styrenesulfonate) (PEDOT:PSS) onto TCO [109]–[111] whereas regular planar ones were prepared removing the mesoporous scaffold and controlling perovskite quality by evaporation routes [112], using ZnO or SnO₂ compact layer [113], [114] or by interfacial engineering treatments such as Y-doped TiO₂ [115]. Finally, inverted structures with mesoporous architectures were obtained using NiO mesoporous scaffolds on the bottom part of the solar cell [116], [117].

Independently the configuration employed for PSC fabrication, the selection of adequate ETM and HTM materials plays a decisive role in the characteristics and performance of the final solar cell. For instance, solar cell V_{OC} is determined by the absorber bandgap minus losses. These losses can be either from recombination issues explained before or mismatching between perovskite valence band and HTM highest occupied molecular orbital (HOMO) for hole injection on one side,

and perovskite conduction band and *n*-type semiconductor conduction band (lowest unoccupied molecular orbital, LUMO when *n*-type semiconductor is organic) for electron injection on the other. Although a minimum driving force (~ 0.1 eV) is mandatory in order to inject in a sufficient manner h^+ and e^- in HTM and ETM respectively, mismatchings larger than driving force are problematic as they are transformed into detrimental voltage losses. Hence, searching novel HTM organic materials and alternative ETM with frontier orbitals compatible with perovskite is considered a challenge in order to take profit from the whole perovskite bandgap.

Furthermore, other important features such as potential low cost, easy synthesis and homogenous large scale deposition routes are additional requirements must be warranted by new HTMs and ETM.

1.3.6 Deposition routes

The selection of an appropriated deposition technique is one of the principal limitations to reach good optical and electrical properties for the final perovskite layer. In general, perovskite deposition routes for PV applications have been exploited noticeably for small size, *i.e.* to fabricate small area solar cells for research purposes. Thus, different approaches will be described in detail in the following sections. Independently of the synthesis route employed or the size of the PV device, the chemical reaction consist on the reaction of an organic halide (AX) such as methylammonium or formamidinium iodide with a metal (II) halide (MX_2), normally lead halides such as lead iodide, lead bromide, or lead chloride according equation 1.21.



Recently some noticeable approaches are being made in order to upscale the size of PSC. For example, Han and coworkers reported several methods to make possible the upscaling, such us the fabrication of fully printable PSC without organic layers [118] or the recent stable and large area perovskite modules with high certified efficiency (over 15%) using new inorganic extraction layers [14], [38]. 100 cm² modules were recently reported using blade-coating easy scalable processes [119]. Other interesting route in order to minimize the cost of PV modules have been the implementation of roll-to-roll fabrication processes onto flexible substrates [120]. Finally, the introduction of glass frits to prepare an encapsulated perovskite modules have been reported as well [121], but it doesn't seem to be an effective approach since the thickness of the perovskite films prepared exceed normally the diffusion length.

While for lab deposition routes, four main different techniques are distinguished: spin-coating 1-step deposition, sequential deposition, vapor deposition and vapor-assisted solution process (VASP).

1.3.7 Spin coating 1-step deposition

This is a solution process technique where both inorganic (PbX_2) and organic (AX) precursors are included and dispersed from the same solution using organic solvents such as gamma-butyrolactone, *N,N*-dimethylformamide (DMF), dimethylsulfoxide (DMSO) or a mixture of them. Then, the mixture is spread onto the substrate and spin-coated to remove the excess of solvent making possible the solid-state reaction. Subsequently, the perovskite films are heated to anneal them [32], [33]. This process was the first developed for perovskite PV fabrication and it is depicted in below scheme:

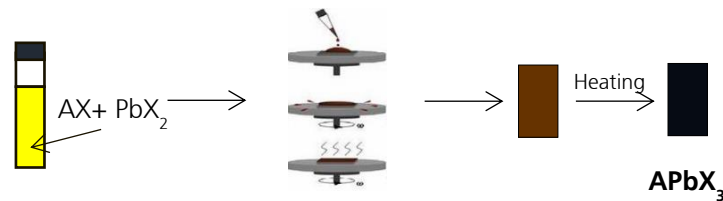


Figure 1.13. Scheme of spin-coating 1-step deposition technique.

Recently, this method has been modified by dripping a poorly polar or non-polar solvent either toluene [122] or chlorobenzene [123] during the drying step of spin coating forming bigger and defect less crystals pushing up the photocurrent.

1.3.7.1 Sequential deposition

This process is based on a variation of previous technique where the inorganic lead halide precursor is deposited initially by spin coating and, after that, the formation of perovskite is achieved by immersing the dried film in an organic precursor solution in isopropanol [35].

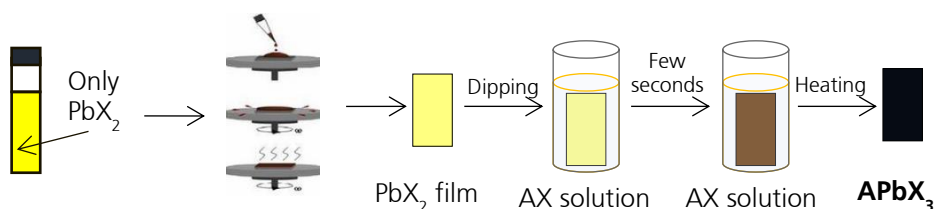


Figure 1.14. Scheme of sequential deposition technique. Adapted from Burschka *et al.* [35].

Im *et al.* [124] proposed a variety of technique where the formation of perovskite is induced by dropping the organic precursor solution onto the inorganic dried film and then spinning that to remove the excess of solvent.

1.3.7.2 Vapor-assisted solution process (VASP)

This is a mix solution-vapor process technique, where the inorganic precursor (PbX_2) is casted onto the substrate by solution process in a first step and then, the films are exposed to an atmosphere rich in organic precursor (AX) to grow perovskite [125]. This approach was proposed by Chen *et al.* obtaining very uniform films with a good control of homogeneity and crystal size. A process diagram of this route is depicted in Figure 1.15.

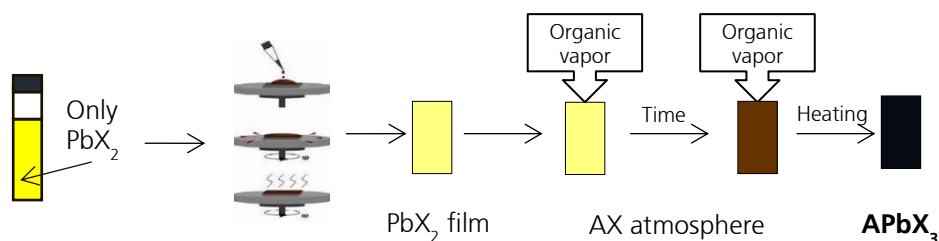


Figure 1.15. Scheme of vapor-assisted solution process. Adapted from Chen *et al.* [125]

1.3.7.3 Vapor deposition

Vapor deposition was firstly reported by Liu and coworkers [112] using a double source: one for the organic (AX) and the other for the inorganic one (PbX_2). One of the issues to control is the gap between sublimation temperatures for organic (low temperature) and inorganic precursors (high temperature) that make difficult the control over the ascendant flows to regulate the stoichiometry of the final material [112]. In Figure 1.16 the scheme of such system is represented. A possible alternative to limit the problems over the stoichiometry control in vapor deposition consist on depositing successively the inorganic and organic compound [126].

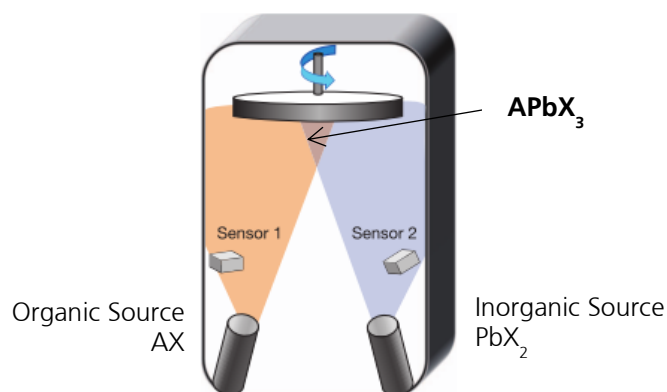


Figure 1.16. Scheme of vapor deposition technique. Taken from Liu *et al.* [112]

A modified version of vapor deposition is recently reported as flash evaporation [127], where perovskite is firstly deposited by conventional solution process techniques over a tantalum sheet and successively placed inside a vacuum chamber promoting the flash evaporation over the desired substrate as current is increased.

1.3.8 Other aspects to consider for future commercialization

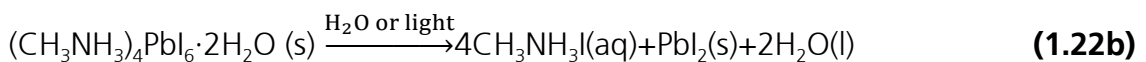
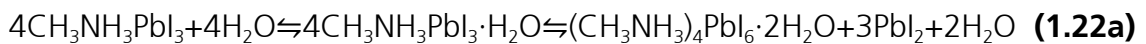
Although the selection of an adequate synthesis route for large area perovskite production maintaining the excellent properties uniformity and low cost obtained at lab scale is still an important bottleneck for future industrial fabrication, there are some other aspects to keep in mind considering a potential future commercialization.

On the one hand, the introduction of lead compounds provides a toxicity concern. According Directive 2011/65/EU of the European Parliament and of the Council of June 8th 2011 regarding the restriction of the use of hazardous substances in

electrical and electronic equipment, the limit of lead present in the final device cannot exceed 0.1% in weight. However, in the point 4.i of the same document it is clearly specified that PV panels are excluded from that rule so any quantity of lead can be used for PV purposes [128]. In addition, to have a global perception, the amount of lead employed to obtain 1000 GW_p year⁻¹ using lead perovskites would be less than 10⁴ tons while 4×10⁶ tons of lead are used every year for lead-acid batteries [129]. Moreover, the substitution of lead by tin was addressed as an advantage from an environmental and security point of view in some works [49], [50]; however, the degradation products of tin perovskites, *i.e.* tin halides, were demonstrated much worse than lead halides for health in a recent study made in zebrafish (*Danio rerio*) [130]. So, the replacement of lead perovskites by tin ones doesn't seem to be of interest neither from a practical point of view (limited efficiencies) nor from a health one. In conclusion, lead toxicity remains as a minor issue since the quantity of lead is low, in principle, there are not legal restrictions for its employment and the candidates to replace it are poorly efficient and paradoxically more poisonous when degraded.

On the other hand, instability of perovskite seems to be one of the main limitations for future commercialization. Concerning temperature, pure methylammonium lead iodide which is the principal example for perovskite photovoltaics presents a phase transition in the range 55-57 °C [59], [60] that could be exceeded during normal operation the final installation. In addition thermal instability of CH₃NH₃PbI₃ in different atmospheres has been addressed provoking degradation into their precursor components as well [131].

Problems in watery ambient are commonly mentioned [132], [133] however the degradation mechanism of perovskite driven by moisture was not been reported until Leguy *et al.* work [134]. In this study two stages are well distinguished. First one corresponds with a reversible perovskite hydration forming mono and later dihydrate (equation 1.22a); while in the former one only the water molecules are captured to form the complex, in the latter the first liberation of PbI₂ is materialized. After that, if either the moisture source is not removed or a light source is nearby, the dihydrate is transformed irreversibly into the original precursor components, *i.e.* lead iodide and methyl ammonium iodide (equation 1.22b).



Recently, another chemical degradation mechanism has been reported. It entails reverse degradation in presence of ammonia [135]. Additionally, some of the additives are frequently presented in HTM recipes can incite a faster degradation.

Regarding effect of light, ultraviolet wavelengths can promote an irreversible degradation of perovskite materials which was not presented in the studies using white LED light [136].

In order to control the stability presented in PSC caused by the abovementioned environmental conditions, several attempts have been addressed in literature. For

instance, to avoid water-driven perovskite degradation, the introduction of hydrophobic agents as polymer-carbon nanotube composites were tested as an effective approach to limit moisture-driven degradation even under moderate heating conditions [137]. Other possibility to control perovskite stability has consisted in removing organic compounds from solar cell architecture being replaced by inorganic ones [117], [118], since certain additives habitually employed to reach high performance using organic semiconductors, like Bis(trifluoromethane)sulfonimide lithium salt (LiTFSI) are highly hygroscopic and other ones directly reacts or dissolves perovskite as 4-*tert*-Butylpyridine (t-BP). Additional possibilities to enhance long term stability of PSC also reported in literature comprised interfacial modifications such as the introduction of chromium oxide-chromium contact to improve air stability [138], CsBr/titania interface modification to improve UV-light instability [139], and the introduction of alkylphosphonic acid ω -ammonium chlorides as crosslinkers, where not only the stability is improved due to an interfacial improvement between perovskite and mesoporous titania, but also the efficiency was enhanced as a result of crosslinking of neighboring perovskite grains [140].

The introduction of hybrid perovskites in multijunctions has been proposed as a potential way to pave the development of mixed PV tandem technologies with superior harvesting properties [141]. Up to now, some efforts have been made to create perovskite tandem multijunctions in combination with silicon [142], [143], $\text{Cu}_2\text{ZnSn}(\text{S},\text{Se})_4$ kesterite [144] and CIGS [143] in order to enhance PV characteristics, but the results were not completely satisfactory since the output power of the best PV individual device were practically not improved by the introduction of tandem architecture. Other perovskite usages with potential commercial interest reported recently consist on water-splitting devices combining perovskite with NiFe layered double hydroxide [145] or BiVO_4 [146].

1.4 Motivation and scope of this work.

Considering the previous state of the art, the search of novel porous photoanodes and new easy to fabricate and cost effective HTM are considered as a necessary requisite to promote and enhance the knowledge of this emerging technology making possible for future commercialization.

New HTMs are required in order to replace the expensive Spiro-OMeTAD or Poly(triarylamine) (PTAA). Those molecules were demonstrated as effective candidates for research and lab scale, however their cost could limit the progress of PSC cell technology. Thus, new small organic molecules easy to fabricate and cost effective were proposed showing properties and behavior remarkable considering the state of the art. The molecules proposed in this thesis were: TIPS-pentacene, where the novelty relies on the use of that molecule as HTM for PSC since it is an classical well studied, high mobility and cheap organic semiconductor; new Zn(II)-based non-aggregated phthalocyanine abbreviated as TT80 and triazatruxene-based compounds (called HMDI and HPDI) with extremely good solubility and HOMO level available to be implemented in PSC as HTM.

Regarding ETM, although planar architecture approaches were proved in literature, best performances and characteristics have been reached with the use of porous inorganic ETM (TiO_2 or ZnO) over a dense buffer or blocking layer using regular

architectures. These materials combine excellent properties with scalable approach. Nevertheless, the techniques employed at lab scale, such as spin-coating or spray coating, are not possible to upscale correctly, are time and material consuming and poorly reproducible being difficult and inadequate for future commercial approaches. Hence, new deposition techniques both easy scalable and highly reproducible and low material consuming are essential for future applications [147]. In this work, solvent-free techniques, such as plasma deposition for ZnO nanowires (PECVD), and physical vapor deposition at oblique angle deposited (PVD-OAD) for TiO₂ nanocolumns and mixed TiO₂-SiO₂, 1-dimensional nanocolumnar photonic crystals were employed and analyzed in order to fabricate fully controllable and easy to upscale porous photoanodes for PSC.

Literature

- [1] Solar Power Europe (SPE), "Global Market Outlook For Solar Power 2015-2019," 2015.
- [2] E. Becquerel, "Mémoire sur les effets électriques produits sous l'influence des rayons solaires," *Comptes Rendus*, pp. 561–567, 1839.
- [3] W. G. Adams and R. E. Day, "The Action of Light on Selenium," *Proc. Royal Soc. (London)*, vol. A25, pp. 113–117, 1877.
- [4] C. E. Fritts, "On a New Form of Selenium Photocell," *American Journal of Science*, vol. 26, pp. 465–472, 1883.
- [5] M. A. Green, "Photovoltaics: Coming on age," *PVSC 1990*, vol. 1, pp. 1–8, 1990.
- [6] L. O. Grondahl, "The Copper-Cuprous-Oxide Rectifier and Photoelectric Cell," *Rev. Mod. Phys.*, vol. 5, p. 141, 1933.
- [7] L. Bergmann, "Über eine neue Selen- Sperrschicht Photozelle," *Physikalische Zeitschrift*, vol. 32, p. 286, 1931.
- [8] F. C. Nix and A. W. Treptow, "A Thallous Sulphide Photo EMF Cell," *Journal Opt. Society of America*, vol. 29, p. 457, 1939.
- [9] J. Czochralski, "Ein neues Verfahren zur Messung der Kristallisationsgeschwindigkeit der Metalle," *Zeitschrift für Physikalische Chemie*, vol. 92, pp. 219–221, 1918.
- [10] D. C. Brock, "Useless No More: Gordon K. Teal, Germanium, and Single-Crystal Transistors," *Chemical Heritage Newsmagazine (Chemical Heritage Foundation)*, vol. 24, no. 1, 2006.
- [11] R. Ohl, "Light-Sensitive Electric device," *U.S. Patent*, p. 2,402,622, 1941.
- [12] D. M. Chapin, C. S. Fuller, and G. L. Pearson, "A New Silicon p-n Junction Photocell for Converting Solar Radiation into Electrical Power," *Journal of Applied Physics*, vol. 25, no. 5, pp. 676–677, 1954.
- [13] P. Basore, "Defining terms for crystalline silicon solar cells.," *Progress in Photovoltaics: Research and Applications.*, vol. 2, pp. 177–179, 1994.
- [14] M. A. Green, K. Emery, Y. Hishikawa, W. Warta, and E. Dunlop, "Solar cell efficiency tables (version 47)," *Prog. Photovolt: Res. Appl.*, vol. 24, pp. 3–11, 2016.
- [15] "Photovoltaics report," *Fraunhofer ISE*, vol. March, pp. 18–19, 2016.

- [16] Z. I. Alferov, V. M. Andreev, M. B. Kagan, I. I. Protasov, and V. G. Trofim, "Solar-energy converters based on p-n $\text{Al}_x\text{Ga}_{1-x}\text{As-GaAs}$ heterojunctions," *Fiz. Tekh. Poluprovodn.*, vol. 4, p. 2378, 1970.
- [17] C. R. Carlson, D.E. and Wronski, "Amorphous Silicon Solar Cells," *Appl. Phys. Lett.*, vol. 28, pp. 671–673, 1976.
- [18] B. O'Regan and M. Grätzel, "A low-cost, high-efficiency solar cell based on dye-sensitized colloidal TiO_2 films," *Nature*, vol. 353, pp. 737–740, 1991.
- [19] U. Bach, D. Lupo, P. Comte, J. E. Moser, F. Weissörtel, J. Salbeck, H. Spreitzer, and M. Grätzel, "Solid-state dye-sensitized mesoporous TiO_2 solar cells with high photon-to-electron conversion efficiencies," *Nature*, vol. 395, pp. 583–585, 1998.
- [20] A. Hagfeldt, G. Boschloo, L. Sun, L. Kloo, and H. Pettersson, "Dye-sensitized solar cells.," *Chem. Rev.*, vol. 110, no. 11, pp. 6595–6663, 2010.
- [21] J. Burschka, A. Dualeh, F. Kessler, E. Baranoff, N. L. Cevey-Ha, C. Yi, M. K. Nazeeruddin, and M. Grätzel, "Tris(2-(1 H -pyrazol-1-yl)pyridine)cobalt(III) as *p*-type dopant for organic semiconductors and its application in highly efficient solid-state dye-sensitized solar cells," *J. Am. Chem. Soc.*, vol. 133, no. 45, pp. 18042–18045, 2011.
- [22] I. Chung, B. Lee, J. He, R. P. H. Chang, and M. G. Kanatzidis, "All-solid-state dye-sensitized solar cells with high efficiency.," *Nature*, vol. 485, pp. 486–489, 2012.
- [23] E. Bundgaard and F. Krebs, "Low band gap polymers for organic photovoltaics," *Sol. Energ. Mat. Sol. Cells*, vol. 91, no. 11, pp. 954–985, 2007.
- [24] R. Debnath, O. Bakr, and E. H. Sargent, "Solution-processed colloidal quantum dot photovoltaics: A perspective," *Energy Environ. Sci.*, vol. 4, no. 12, pp. 4870–4881, 2011.
- [25] D. B. Mitzi, C. a. Feild, W. T. a. Harrison, and a. M. Guloy, "Conducting tin halides with a layered organic-based perovskite structure," *Nature*, vol. 369, no. 6480, pp. 467–469, 1994.
- [26] D. B. Mitzi, "Synthesis, Structure, and Properties of Organic-Inorganic Perovskites and Related Materials," *Prog. Inorg. Chem.*, vol. 48, pp. 1–121, 1999.
- [27] K. Liang, D. B. Mitzi, and M. T. Prikas, "Synthesis and Characterization of Organic–Inorganic Perovskite Thin Films Prepared Using a Versatile Two-Step Dipping Technique," *Chem. Mater.*, vol. 10, no. 1, pp. 403–411, 1998.
- [28] C. R. Kagan, D. . Mitzi, and C. D. Dimitrakopoulos, "Organic-Inorganic Hybrid Materials as Semiconducting Channels in Thin-Film Field-Effect Transistors," *Science*, vol. 286, pp. 945–947, 1999.

- [29] D. . Mitzi, K. Chondroudis, and C. R. Kagan, "Organic – inorganic electronics," *IBM J. Res. Dev.*, vol. 45, no. 1, pp. 29–45, 2001.
- [30] A. Kojima, K. Teshima, Y. Shirai, and T. Miyasaka, "Organometal halide perovskites as visible-light sensitizers for photovoltaic cells.," *J. Am. Chem. Soc.*, vol. 131, no. 17, pp. 6050–6051, 2009.
- [31] J.-H. Im, C.-R. Lee, J.-W. Lee, S.-W. Park, and N.-G. Park, "6.5% Efficient Perovskite Quantum-Dot-Sensitized Solar Cell," *Nanoscale*, vol. 3, no. 10, pp. 4088–4093, 2011.
- [32] H.-S. Kim, C.-R. Lee, J.-H. Im, K.-B. Lee, T. Moehl, A. Marchioro, S.-J. Moon, R. Humphry-Baker, J.-H. Yum, J. E. Moser, M. Grätzel, and N.-G. Park, "Lead Iodide Perovskite Sensitized All-Solid-State Submicron Thin Film Mesoscopic Solar Cell with Efficiency Exceeding 9%," *Sci. Rep.*, vol. 2, p. 591, 2012.
- [33] M. M. Lee, J. Teuscher, T. Miyasaka, T. N. Murakami, and H. J. Snaith, "Efficient Hybrid Solar Cells Based on Meso-Superstructured Organometal Halide Perovskites," *Science*, vol. 338, no. 6107, pp. 643–647, 2012.
- [34] L. Etgar, P. Gao, Z. Xue, Q. Peng, A. K. Chandiran, and B. Liu, "Mesoscopic $\text{CH}_3\text{NH}_3\text{PbI}_3/\text{TiO}_2$ Heterojunction Solar Cells," *J. Am. Chem. Soc.*, vol. 134, pp. 17396–17399, 2012.
- [35] J. Burschka, N. Pellet, S.-J. Moon, R. Humphry-Baker, P. Gao, M. K. Nazeeruddin, and M. Grätzel, "Sequential deposition as a route to high-performance perovskite-sensitized solar cells.," *Nature*, vol. 499, no. 7458, pp. 316–319, 2013.
- [36] N. J. Jeon, J. H. Noh, W. S. Yang, Y. C. Kim, S. Ryu, J. Seo, and S. Il Seok, "Compositional engineering of perovskite materials for high-performance solar cells," *Nature*, vol. 517, no. 7535, pp. 476–480, 2015.
- [37] W. S. Yang, J. H. Noh, N. J. Jeon, Y. C. Kim, S. Ryu, J. Seo, and S. Il Seok, "High-performance photovoltaic perovskite layers fabricated through intramolecular exchange," *Science*, vol. 348, no. 6240, pp. 1234–1237, 2015.
- [38] W. Chen, Y. Wu, Y. Yue, J. Liu, W. Zhang, X. Yang, H. Chen, E. Bi, I. Ashraful, M. Grätzel, and L. Han, "Efficient and stable large-area perovskite solar cells with inorganic charge extraction layers," *Science*, vol. 350, no. 6263, pp. 944–948, 2015.
- [39] M. A. Green, *Solar Cells - Operating Principles, Technology and System Application*. Kensington, Australia: University of NSW, 1992.
- [40] A. McEvoy, T. Markvart, and L. Castañer, *Practical handbook of photovoltaics: fundamentals and applications*, 2nd ed. Elsevier Ltd., 2012.
- [41] S. M. Sze and K. K. Ng, *Physics of Semiconductor Devices*, 3rd ed. Wiley Interscience, 2006.

- [42] M. D. Graef and M. McHenry, *Structure of materials: an introduction to crystallography, diffraction and symmetry*. Cambridge University Press, 2007.
- [43] N. A. Benedek and C. J. Fennie, "Why Are There So Few Perovskite Ferroelectrics?," *J. Phys. Chem. C*, vol. 117, pp. 13339–13349, 2013.
- [44] N. Pellet, P. Gao, G. Gregori, T.-Y. Yang, M. K. Nazeeruddin, J. Maier, and M. Grätzel, "Mixed-organic-cation perovskite photovoltaics for enhanced solar-light harvesting.," *Angew. Chem. Int. Ed.*, vol. 53, no. 12, pp. 3151–317, 2014.
- [45] G. E. Eperon, S. D. Stranks, C. Menelaou, M. B. Johnston, L. Herz, and H. Snaith, "Formamidinium lead trihalide: a broadly tunable perovskite for efficient planar heterojunction solar cells," *Energy Environ. Sci.*, vol. 7, pp. 982–988, 2014.
- [46] T. M. Koh, T. Krishnamoorthy, N. Yantara, C. Shi, W. L. Leong, P. P. Boix, A. C. Grimsdale, S. G. Mhaisalkar, and N. Mathews, "Formamidinium tin-based perovskite with low E_g for photovoltaic applications," *J. Mater. Chem. A*, vol. 3, pp. 14996–15000, 2015.
- [47] J. H. Noh, S. H. Im, J. H. Heo, T. N. Mandal, and S. Il Seok, "Chemical Management for Colorful, Efficient, and Stable Inorganic – Organic Hybrid Nanostructured Solar Cells," *Nano Lett.*, vol. 13, pp. 1764–1769, 2013.
- [48] S. a. Kulkarni, T. Baikie, P. P. Boix, N. Yantara, N. Mathews, and S. Mhaisalkar, "Band-gap tuning of lead halide perovskites using a sequential deposition process," *J. Mater. Chem. A*, vol. 2, no. 24, pp. 9221–9225, 2014.
- [49] F. Hao, C. C. Stoumpos, D. H. Cao, R. P. H. Chang, and M. G. Kanatzidis, "Lead-free solid-state organic–inorganic halide perovskite solar cells," *Nature Photon.*, vol. 8, no. 6, pp. 489–494, 2014.
- [50] N. K. Noel, S. D. Stranks, A. Abate, C. Wehrenfennig, S. Guarnera, A. Haghighirad, A. Sadhanala, G. E. Eperon, S. K. Pathak, M. B. Johnston, A. Petrozza, L. Herz, and H. Snaith, "Lead-Free Organic-Inorganic Tin Halide Perovskites for Photovoltaic Applications," *Energy Environ. Sci.*, vol. 7, pp. 3061–3068, 2014.
- [51] V. M. Goldschmidt, "Die Gesetze der Krystallochemie"., *Die Naturwissenschaften*, vol. 21, pp. 477–485, 1926.
- [52] C. Li, X. Lu, W. Ding, L. Feng, Y. Gao, and Z. Guo, "Formability of ABX_3 ($X = F, Cl, Br, I$) halide perovskites," *Acta Crystallogr. Sect. B*, vol. 64, pp. 702–707, 2008.
- [53] M. A. Green, A. Ho-Baillie, and H. J. Snaith, "The emergence of perovskite solar cells," *Nature Photon.*, vol. 8, no. 7, pp. 506–514, 2014.

- [54] C. Eames, J. M. Frost, P. R. F. Barnes, B. C. O'Regan, A. Walsh, and M. S. Islam, "Ionic transport in hybrid lead iodide perovskite solar cells," *Nat. Commun.*, vol. 6, p. 7497, 2015.
- [55] P. Gao, M. Grätzel, and M. K. Nazeeruddin, "Organohalide lead perovskites for photovoltaic applications," *Energy Environ. Sci.*, vol. 7, pp. 2448–2463, 2014.
- [56] R. Tilley, *Crystals and Crystal Structures*. John Wiley., 2006.
- [57] M. Coll, A. Gomez, E. Mas-Marza, O. Almora, G. Garcia-Belmonte, M. Campoy-Quiles, and J. Bisquert, "Polarization Switching and Light-Enhanced Piezoelectricity in Lead Halide Perovskites," *J. Phys. Chem. Lett.*, vol. 6, no. 8, pp. 1408–1413, 2015.
- [58] J. M. Frost, K. T. Butler, F. Brivio, C. H. Hendon, M. van Schilfgaarde, and A. Walsh, "Atomistic origins of high-performance in hybrid halide perovskite solar cells," *Nano Lett.*, vol. 14, no. 5, pp. 2584–2590, 2014.
- [59] A. Poglitsch and D. Weber, "Dynamic disorder in methylammoniumtrihalogenoplumbates (II) observed by millimeter-wave spectroscopy," *J. Chem. Phys.*, vol. 87, no. 11, pp. 6373–6378, 1987.
- [60] C. C. Stoumpos, C. D. Malliakas, and M. G. Kanatzidis, "Semiconducting tin and lead iodide perovskites with organic cations: phase transitions, high mobilities, and near-infrared photoluminescent properties.," *Inorg. Chem.*, vol. 52, no. 15, pp. 9019–9038, 2013.
- [61] T. Baikie, Y. Fang, J. M. Kadro, M. Schreyer, F. Wei, S. G. Mhaisalkar, M. Graetzel, and T. J. White, "Synthesis and crystal chemistry of the hybrid perovskite $(\text{CH}_3\text{NH}_3)\text{PbI}_3$ for solid-state sensitised solar cell applications," *J. Mater. Chem. A*, vol. 1, no. 18, pp. 5628–5641, 2013.
- [62] S. a. Bretschneider, J. Weickert, J. a. Dorman, and L. Schmidt-Mende, "Research Update: Physical and electrical characteristics of lead halide perovskites for solar cell applications," *APL Mat.*, vol. 2, no. 4, p. 040701, 2014.
- [63] Y. Kawamura, H. Mashiyama, and K. Hasebe, "Structural Study on Cubic-Tetragonal Transition of $\text{CH}_3\text{NH}_3\text{PbI}_3$," *J. Phys. Soc. Jpn.*, vol. 71, no. 7, pp. 1694–1697, 2002.
- [64] M. T. Weller, O. J. Weber, P. F. Henry, A. M. Di Pumpo, and T. C. Hansen, "Complete structure and cation orientation in the perovskite photovoltaic methylammonium lead iodide between 100 and 352 K," *Chem. Commun.*, vol. 51, pp. 4180–4183, 2015.
- [65] D. Bi, W. Tress, M. I. Dar, P. Gao, J. Luo, C. Renevier, K. Schenk, A. Abate, F. Giordano, J. C. Baena, J. Decoppet, S. M. Zakeeruddin, M. K. Nazeeruddin, M. Grätzel, and A. Hagfeldt, "Efficient luminescent solar cells based on

- tailored mixed-cation perovskites," *Sci. Adv.*, vol. 2, no. 1, p. DOI: 10.1126/sciadv.1501170, 2016.
- [66] W. Shockley and H. J. Queisser, "Detailed balance limit of efficiency of p-n junction solar cells," *J. Appl. Phys.*, vol. 32, no. 3, pp. 510–519, 1961.
- [67] C. H. Henry, "Limiting efficiencies of ideal single and multiple energy gap terrestrial solar cells," *J. Appl. Phys.*, vol. 51, pp. 4494–4500, 1980.
- [68] A. De Vos, C. C. Grosjean, and H. Pauwelst, "On the formula for the upper limit of photovoltaic solar energy conversion efficiency," *J. Phys. D: Appl. Phys.*, vol. 15, pp. 2003–2015, 1982.
- [69] T. Umebayashi, K. Asai, T. Kondo, and A. Nakao, "Electronic structures of lead iodide based low-dimensional crystals," *Phys. Rev. B*, vol. 67, no. 15, p. 155405, 2003.
- [70] K. Tanaka, T. Takahashi, T. Kondo, K. Umeda, K. Ema, T. Umebayashi, K. Asai, K. Uchida, and N. Miura, "Electronic and Excitonic Structures of Inorganic–Organic Perovskite-Type Quantum-Well Crystal (C₄H₉NH₃)₂PbBr₄," *Jpn. J. Appl. Phys.*, vol. 44, no. 8, pp. 5923–5932, 2005.
- [71] G. Xing, N. Mathews, S. Sun, S. S. Lim, Y. M. Lam, M. Grätzel, S. Mhaisalkar, and T. C. Sum, "Long-range balanced electron- and hole-transport lengths in organic-inorganic CH₃NH₃PbI₃," *Science*, vol. 342, no. 6156, pp. 344–7, 2013.
- [72] S. D. Stranks, G. E. Eperon, G. Grancini, C. Menelaou, M. J. P. Alcocer, T. Leijtens, L. M. Herz, A. Petrozza, and H. J. Snaith, "Electron-hole diffusion lengths exceeding 1 micrometer in an organometal trihalide perovskite absorber," *Science*, vol. 342, no. 6156, pp. 341–4, 2013.
- [73] J. S. Manser and P. V Kamat, "Band filling with free charge carriers in organometal halide perovskites," *Nature Photon.*, vol. 8, pp. 737–743, 2014.
- [74] P. Piatkowski, B. Cohen, F. J. Ramos, M. Di Nunzio, M. K. Nazeeruddin, M. Grätzel, S. Ahmad, and A. Douhal, "Direct monitoring of ultrafast electron and hole dynamics in perovskite solar cells," *Phys. Chem. Chem. Phys.*, vol. 17, no. 22, pp. 14674–14684, 2015.
- [75] K. G. Stamplecoskie, J. S. Manser, and P. V Kamat, "Dual Nature of the Excited State in Organic-Inorganic Lead Halide Perovskites," *Energy Environ. Sci.*, vol. 8, pp. 208–215, 2015.
- [76] C. Roldán Carmona, P. Gratia, I. Zimmermann, G. Grancini, P. Gao, M. Grätzel, and N. Mohammad K., "High efficiency methylammonium lead triiodide perovskite solar cells: the relevance of non-stoichiometric precursors," *Energy Environ. Sci.*, vol. 8, pp. 3550–3556, 2015.

- [77] Q. Lin, A. Armin, R. Chandra, R. Nagiri, P. L. Burn, and P. Meredith, "Electro-optics of perovskite solar cells," *Nature Photon.*, vol. 9, pp. 106–112, 2015.
- [78] M. Anaya, G. Lozano, M. E. Calvo, W. Zhang, M. B. Johnston, H. J. Snaith, and H. Miguez, "Optical Description of Mesostructured Organic-Inorganic Halide Perovskite Solar Cells," *J. Phys. Chem. Lett.*, vol. 6, no. 1, pp. 48–53, 2015.
- [79] V. D'Innocenzo, G. Grancini, M. J. P. Alcocer, A. R. S. Kandada, S. D. Stranks, M. M. Lee, G. Lanzani, H. J. Snaith, and A. Petrozza, "Excitons versus free charges in organo-lead tri-halide perovskites," *Nat. Commun.*, vol. 5, p. 3586, 2014.
- [80] S. Sun, T. Salim, N. Mathews, M. Duchamp, C. Boothroyd, G. Xing, T. C. Sum, and Y. M. Lam, "The origin of high efficiency in low-temperature solution-processable bilayer organometal halide hybrid solar cells," *Energy Environ. Sci.*, vol. 7, pp. 399–407, 2014.
- [81] T. C. Sum and N. Mathews, "Advancements in Perovskite Solar Cells: Photophysics behind the Photovoltaics," *Energy Environ. Sci.*, vol. 7, pp. 2518–2534, 2014.
- [82] I. B. Koutselas, L. Ducasse, and G. C. Papavassiliou, "Electronic properties of three- and low-dimensional semiconducting materials with Pb halide and Sn halide units," *J. Phys.: Condens. Matter*, vol. 8, pp. 1217–1227, 1996.
- [83] M. Hirasawa, T. Ishihara, T. Goto, K. Uchida, and N. Miura, "Magnetoabsorption of the lowest exciton in perovskite-type compound $(\text{CH}_3\text{NH}_3)\text{PbI}_3$," *Physica B*, vol. 201, pp. 427–430, 1994.
- [84] T. Ishihara, "Optical properties of Pbl-based perovskite structures," *J. Lumin.*, vol. 60–61, pp. 269–274, 1994.
- [85] K. Tanaka, T. Takahashi, T. Ban, T. Kondo, K. Uchida, and N. Miura, "Comparative study on the excitons in lead-halide-based perovskite-type crystals $\text{CH}_3\text{NH}_3\text{PbBr}_3$ $\text{CH}_3\text{NH}_3\text{PbI}_3$," *Solid State Commun.*, vol. 127, pp. 619–623, 2003.
- [86] W. Zhang, M. Saliba, S. D. Stranks, Y. Sun, X. Shi, U. Wiesner, and H. J. Snaith, "Enhancement of Perovskite-Based Solar Cells Employing Core – Shell Metal Nanoparticles," *Nano Lett.*, vol. 13, no. 9, pp. 4505–4510, 2013.
- [87] T. Leijtens, S. D. Stranks, G. E. Eperon, R. Lindblad, E. M. J. Johansson, I. J. McPherson, H. Rensmo, J. M. Ball, M. M. Lee, and H. J. Snaith, "Electronic properties of meso-superstructured and planar organometal halide perovskite films: charge trapping, photodoping, and carrier mobility.," *ACS nano*, vol. 8, no. 7, pp. 7147–55, 2014.

- [88] C. Wehrenfennig, G. E. Eperon, M. B. Johnston, H. J. Snaith, and L. M. Herz, "High Charge Carrier Mobilities and Lifetimes in Organolead Trihalide Perovskites," *Adv. Mater.*, vol. 26, no. 10, pp. 1584–1589, 2014.
- [89] C. Wehrenfennig, M. Liu, H. J. Snaith, M. B. Johnston, and L. M. Herz, "Charge-carrier dynamics in vapour-deposited films of the organolead halide perovskite $\text{CH}_3\text{NH}_3\text{PbI}_{3-x}\text{Cl}_x$," *Energy Environ. Sci.*, vol. 7, pp. 2269–2275, 2014.
- [90] M. B. Johnston and L. M. Herz, "Hybrid Perovskites for Photovoltaics: Charge-Carrier Recombination, Diffusion, and Radiative Efficiencies," *Acc. Chem. Res.*, vol. 49, no. 1, pp. 146–154, 2016.
- [91] C. Wehrenfennig, M. Liu, H. J. Snaith, M. B. Johnston, and L. M. Herz, "Homogeneous Emission Line Broadening in the Organo Lead Halide Perovskite $\text{CH}_3\text{NH}_3\text{PbI}_{3-x}\text{Cl}_x$," *J. Phys. Chem. Lett.*, vol. 5, no. 8, pp. 1300–1306, 2014.
- [92] R. L. Milot, G. E. Eperon, H. J. Snaith, M. B. Johnston, and L. M. Herz, "Temperature-Dependent Charge-Carrier Dynamics in $\text{CH}_3\text{NH}_3\text{PbI}_3$ Perovskite Thin Films," *Adv. Funct. Mater.*, vol. 25, no. 39, pp. 6218–6227, 2015.
- [93] W. Rehman, R. L. Milot, G. E. Eperon, C. Wehrenfennig, J. L. Boland, H. J. Snaith, M. B. Johnston, and L. M. Herz, "Charge-Carrier Dynamics and Mobilities in Formamidinium Lead Mixed-Halide Perovskites," *Adv. Mater.*, vol. 27, no. 48, pp. 7938–7944, 2015.
- [94] P. Piatkowski, B. Cohen, C. S. Ponseca, M. Salado, S. Kazim, S. Ahmad, V. Sundström, and A. Douhal, "Unraveling Charge Carriers Generation, Diffusion, and Recombination in Formamidinium Lead Triiodide Perovskite Polycrystalline Thin Film," *J. Phys. Chem. Lett.*, vol. 7, no. 1, pp. 204–210, 2016.
- [95] A. Marchioro, J. Teuscher, D. Friedrich, M. Kunst, R. van de Krol, T. Moehl, M. Grätzel, and J.-E. Moser, "Unravelling the mechanism of photoinduced charge transfer processes in lead iodide perovskite solar cells," *Nature Photon.*, vol. 8, no. 3, pp. 250–255, 2014.
- [96] V. W. Bergmann, S. A. L. Weber, F. J. Ramos, M. K. Nazeeruddin, M. Grätzel, D. Li, A. L. Domanski, I. Lieberwirth, S. Ahmad, and R. Berger, "Real-space observation of unbalanced charge distribution inside a perovskite-sensitized solar cell," *Nat. Commun.*, vol. 5, p. 5001, 2014.
- [97] D. W. DeQuilettes, S. M. Vorpahl, S. D. Stranks, H. Nagaoka, G. E. Eperon, M. E. Ziffer, H. J. Snaith, and D. S. Ginger, "Impact of microstructure on local carrier lifetime in perovskite solar cells," *Science*, vol. 348, no. 6235, pp. 683–686, 2015.
- [98] W. Tress, N. Marinova, T. Moehl, S. M. Zakeeruddin, and M. K. Nazeeruddin, "Understanding the rate-dependent J–V hysteresis, slow time

- component, and aging in $\text{CH}_3\text{NH}_3\text{PbI}_3$ perovskite solar cells: the role of a compensated electric field," *Energy Environ. Sci.*, vol. 8, pp. 995–1004, 2015.
- [99] T.-Y. Yang, G. Gregori, N. Pellet, M. Grätzel, and J. Maier, "The Significance of Ion Conduction in a Hybrid Organic-Inorganic Lead-Iodide-Based Perovskite Photosensitizer," *Angew. Chem. Int. Ed.*, vol. 54, no. 27, pp. 7905–7910, 2015.
- [100] Y. Yuan, J. Chae, Y. Shao, Q. Wang, Z. Xiao, A. Centrone, and J. Huang, "Photovoltaic Switching Mechanism in Lateral Structure Hybrid Perovskite Solar Cells," *Adv. Energy Mater.*, vol. 5, no. 15, p. DOI: 10.1002/aenm.201500615, 2015.
- [101] H. J. Snaith, A. Abate, J. M. Ball, G. E. Eperon, T. Leijtens, N. Kimberly, S. D. Stranks, J. T. Wang, K. Wojciechowski, and W. Zhang, "Anomalous Hysteresis in Perovskite Solar Cells," *J. Phys. Chem. Lett.*, 2014.
- [102] J. A. Christians, J. S. Manser, and P. V. Kamat, "Best Practices in Perovskite Solar Cell Efficiency Measurements. Avoiding the Error of Making Bad Cells Look Good," *J. Phys. Chem. Lett.*, vol. 6, no. 5, pp. 852–857, 2015.
- [103] O. Almora, I. Zarazua, E. Mas-Marza, I. Mora-Sero, J. Bisquert, and G. Garcia-Belmonte, "Capacitive Dark Currents, Hysteresis, and Electrode Polarization in Lead Halide Perovskite Solar Cells," *J. Phys. Chem. Lett.*, vol. 6, no. 9, pp. 1645–1652, 2015.
- [104] Y. Shao, Z. Xiao, C. Bi, Y. Yuan, and J. Huang, "Origin and elimination of photocurrent hysteresis by fullerene passivation in $\text{CH}_3\text{NH}_3\text{PbI}_3$ planar heterojunction solar cells," *Nat. Commun.*, vol. 5, p. 5784, 2014.
- [105] A. Dualeh, T. Moehl, N. Tétrault, J. Teuscher, P. Gao, M. K. Nazeeruddin, and M. Grätzel, "Impedance spectroscopic analysis of lead iodide perovskite-sensitized solid-state solar cells," *ACS Nano*, vol. 8, no. 1, pp. 362–373, 2014.
- [106] Z. Xiao, Y. Yuan, Y. Shao, Q. Wang, Q. Dong, C. Bi, P. Sharma, A. Gruverman, and J. Huang, "Giant switchable photovoltaic effect in organometal trihalide perovskite devices," *Nat. Mater.*, vol. 14, pp. 193–198, 2015.
- [107] S. Van Reenen, M. Kemerink, and H. J. Snaith, "Modeling Anomalous Hysteresis in Perovskite Solar Cells," *J. Phys. Chem. Lett.*, vol. 6, no. 19, pp. 3808–3814, 2015.
- [108] D. Bi, L. Häggman, G. Boschloo, L. Yang, and E. M. J. Johansson, "Using two-step deposition technique to prepare perovskite ($\text{CH}_3\text{NH}_3\text{PbI}_3$) for thin film solar cells based on ZrO_2 and TiO_2 mesostructures," *RSC Adv.*, vol. 3, pp. 18762–18766, 2013.

- [109] J.-Y. Jeng, Y.-F. Chiang, M.-H. Lee, S.-R. Peng, T.-F. Guo, P. Chen, and T.-C. Wen, "CH₃NH₃PbI₃ perovskite/fullerene planar-heterojunction hybrid solar cells," *Adv. Mater.*, vol. 25, no. 27, pp. 3727–32, 2013.
- [110] P. Docampo, J. M. Ball, M. Darwich, G. E. Eperon, and H. J. Snaith, "Efficient organometal trihalide perovskite planar-heterojunction solar cells on flexible polymer substrates," *Nat. Commun.*, vol. 4, p. 2761, 2013.
- [111] O. Malinkiewicz, A. Yella, Y. H. Lee, G. M. Espallargas, M. Graetzel, M. K. Nazeeruddin, and H. J. Bolink, "Perovskite solar cells employing organic charge-transport layers," *Nature Photon.*, vol. 8, pp. 128–132, 2013.
- [112] M. Liu, M. B. Johnston, and H. J. Snaith, "Efficient planar heterojunction perovskite solar cells by vapour deposition," *Nature*, vol. 501, no. 7467, pp. 395–398, 2013.
- [113] D. Liu and T. L. Kelly, "Perovskite solar cells with a planar heterojunction structure prepared using room-temperature solution processing techniques," *Nature Photon.*, vol. 8, pp. 133–138, 2013.
- [114] J. P. Correa Baena, L. Steier, W. Tress, M. Saliba, S. Neutzner, T. Matsui, F. Giordano, T. J. Jacobsson, A. R. Srimath Kandada, S. M. Zakeeruddin, A. Petrozza, A. Abate, M. K. Nazeeruddin, M. Grätzel, and A. Hagfeldt, "Highly efficient planar perovskite solar cells through band alignment engineering," *Energy Environ. Sci.*, vol. 8, pp. 2928–2934, 2015.
- [115] H. Zhou, Q. Chen, G. Li, S. Luo, T. -b. Song, H.-S. Duan, Z. Hong, J. You, Y. Liu, and Y. Yang, "Interface engineering of highly efficient perovskite solar cells," *Science*, vol. 345, no. 6196, pp. 542–546, 2014.
- [116] Z. Zhu, Y. Bai, T. Zhang, Z. Liu, X. Long, Z. Wei, Z. Wang, L. Zhang, J. Wang, F. Yan, and S. Yang, "High-performance hole-extraction layer of sol-gel-processed nio nanocrystals for inverted planar perovskite solar cells," *Angew. Chem. Int. Ed.*, vol. 53, pp. 12571–12575, 2014.
- [117] J. You, L. Meng, T.-B. Song, T.-F. Guo, Y. (Michael) Yang, W.-H. Chang, Z. Hong, H. Chen, H. Zhou, Q. Chen, Y. Liu, N. De Marco, and Y. Yang, "Improved air stability of perovskite solar cells via solution-processed metal oxide transport layers," *Nat. Nanotechnol.*, vol. 11, pp. 75–81, 2016.
- [118] A. Mei, X. Li, L. Liu, Z. Ku, T. Liu, Y. Rong, M. Xu, M. Hu, J. Chen, Y. Yang, M. Gratzel, and H. Han, "A hole-conductor-free, fully printable mesoscopic perovskite solar cell with high stability," *Science*, vol. 345, no. 6194, pp. 295–298, 2014.
- [119] S. Razza, F. Di Giacomo, F. Matteocchia, L. Cinà, A. L. Palma, S. Casalucia, P. Cameron, A. D'Epifanio, S. Licocchia, A. Reale, T. M. Brown, and A. Di Carlo, "Perovskite solar cells and large area modules (100 cm²) based on an air flow-assisted PbI₂ blade coating deposition process," *J. Power Sources*, vol. 277, no. 1, pp. 286–291, 2015.

- [120] T. M. Schmidt, T. T. Larsen-Olsen, J. E. Carlé, D. Angmo, and F. C. Krebs, "Upscaling of Perovskite Solar Cells: Fully Ambient Roll Processing of Flexible Perovskite Solar Cells with Printed Back Electrodes," *Adv. Energy Mater.*, vol. 5, no. 15, p. DOI: 10.1002/aenm.201500569, 2015.
- [121] A. Hinsch, S. Mastroianni, H. Brandt, F. Heinz, M. C. Schubert, and W. Veurman, "Introduction to in-situ produced perovskite solar cells; a new concept towards lowest module manufacturing costs," *29th European PV Solar Energy Conference and Exhibition*, no. September, pp. 1–5, 2014.
- [122] N. J. Jeon, J. H. Noh, Y. C. Kim, W. S. Yang, S. Ryu, and S. Il Seok, "Solvent engineering for high-performance inorganic-organic hybrid perovskite solar cells.," *Nat. Mater.*, vol. 13, no. September, pp. 897–903, 2014.
- [123] M. Xiao, F. Huang, W. Huang, Y. Dkhissi, Y. Zhu, J. Etheridge, A. Gray-Weale, U. Bach, Y.-B. Cheng, and L. Spiccia, "A Fast Deposition-Crystallization Procedure for Highly Efficient Lead Iodide Perovskite Thin-Film Solar Cells," *Angew. Chem. Int. Ed.*, vol. 126, no. 37, pp. 10056–10061, 2014.
- [124] J.-H. Im, I.-H. Jang, N. Pellet, M. Grätzel, and N.-G. Park, "Growth of $\text{CH}_3\text{NH}_3\text{PbI}_3$ cuboids with controlled size for high-efficiency perovskite solar cells," *Nat. Nanotechnol.*, vol. 9, pp. 927–932, 2014.
- [125] Q. Chen, H. Zhou, Z. Hong, S. Luo, H.-S. Duan, H.-H. Wang, Y. Liu, G. Li, and Y. Yang, "Planar heterojunction perovskite solar cells via vapor-assisted solution process.," *J. Am. Chem. Soc.*, vol. 136, no. 2, pp. 622–625, 2014.
- [126] C.-W. Chen, H.-W. Kang, S.-Y. Hsiao, P.-F. Yang, K.-M. Chiang, and H.-W. Lin, "Efficient and Uniform Planar-Type Perovskite Solar Cells by Simple Sequential Vacuum Deposition," *Adv. Mater.*, vol. 26, no. 38, pp. 6647–6652, 2014.
- [127] G. Longo, L. Gil-Escrig, M. J. Degen, M. Sessolo, and H. J. Bolink, "Perovskite solar cells prepared by flash evaporation," *Chem. Commun.*, no. 51, pp. 7376–7378, 2015.
- [128] European Parliament, *Directive 2011/65/EU of the European Parliament and of the Council of 8 June 2011 on the restriction of the use of certain hazardous substances in electrical and electronic equipment (RoHS)*, vol. 174, no. 1 July. 2011, pp. 88–110.
- [129] G. Hodes, "Perovskite-based solar cells.," *Science*, vol. 342, pp. 317–318, 2013.
- [130] A. Babayigit, D. D. Thanh, A. Ethirajan, J. Manca, M. Muller, H.-G. Boyen, and B. Conings, "Assessing the toxicity of Pb- and Sn-based perovskite solar cells in model organism *Danio rerio*," *Sci. Rep.*, vol. 6, p. 18721, 2016.
- [131] B. Conings, J. Drijkoningen, N. Gauquelin, A. Babayigit, J. D'Haen, L. D'Olieslaeger, A. Ethirajan, J. Verbeeck, J. Manca, E. Mosconi, F. De Angelis,

- and H. Boyen, "Intrinsic Thermal Instability of Methylammonium Lead Trihalide Perovskite," *Adv. Energy Mater.*, vol. 5, no. 15, p. DOI: 10.1002/aenm.201500477, 2015.
- [132] J. Yang, B. D. Siempelkamp, D. Liu, and T. L. Kelly, "An Investigation of $\text{CH}_3\text{NH}_3\text{PbI}_3$ Degradation Rates and Mechanisms in Controlled Humidity Environments Using in situ Techniques," *ACS Nano*, vol. 9, no. 2, pp. 1955–1963, 2015.
- [133] B. Philippe, B.-W. Park, R. Lindblad, J. Oscarsson, S. Ahmadi, E. M. J. Johansson, and H. Rensmo, "Chemical and Electronic Structure Characterization of Lead Halide Perovskites and Stability Behavior under Different Exposures - a Photoelectron Spectroscopy Investigation," *Chem. Mater.*, vol. 27, no. 5, pp. 1720–1731, 2015.
- [134] A. Leguy, Y. Hu, M. Campoy-quiles, M. I. Alonso, O. J. Weber, P. Azarhoosh, M. Van Schilfgaarde, M. T. Weller, T. Bein, J. Nelson, P. Docampo, and P. R. F. Barnes, "The reversible hydration of $\text{CH}_3\text{NH}_3\text{PbI}_3$ in films, single crystals and solar cells," *Chem. Mater.*, vol. 27, no. 9, pp. 3397–3407, 2015.
- [135] Y. Zhao and K. Zhu, "Optical bleaching of perovskite (CH_3NH_3) PbI_3 through room-temperature phase transformation induced by ammonia.," *Chem. Commun.*, vol. 50, no. 13, pp. 1605–1607, 2014.
- [136] T. Leijtens, G. E. Eperon, S. Pathak, A. Abate, M. M. Lee, and H. J. Snaith, "Overcoming ultraviolet light instability of sensitized TiO_2 with meso-structured organometal tri-halide perovskite solar cells.," *Nat. Commun.*, vol. 4, p. 2885, 2013.
- [137] S. N. Habisreutinger, T. Leijtens, G. E. Eperon, S. D. Stranks, R. J. Nicholas, and H. J. Snaith, "Carbon Nanotube/Polymer Composites as a Highly Stable Hole Collection Layer in Perovskite Solar Cells.," *Nano Lett.*, vol. 14, pp. 5561–5568, 2014.
- [138] M. Kaltenbrunner, G. Adam, E. D. Głowacki, M. Drack, R. Schwödiauer, L. Leonat, D. H. Apaydin, H. Groiss, M. C. Scharber, M. S. White, N. S. Sariciftci, and S. Bauer, "Flexible high power-per-weight perovskite solar cells with chromium oxide–metal contacts for improved stability in air," *Nat. Mater.*, vol. 14, pp. 1032–1039, 2015.
- [139] W. Li, W. Zhang, S. Van Reenen, R. J. Sutton, J. Fan, A. A. Haghghirad, M. B. Johnston, L. Wang, and H. J. Snaith, "Enhanced UV-light stability of planar heterojunction perovskite solar cells with caesium bromide interface modification," *Energy Environ. Sci.*, vol. 9, pp. 490–498, 2016.
- [140] X. Li, M. I. Dar, C. Yi, J. Luo, M. Tschumi, S. M. Zakeeruddin, M. K. Nazeeruddin, H. Han, and M. Grätzel, "Improved performance and stability of perovskite solar cells by crystal crosslinking with alkylphosphonic acid ω -ammonium chlorides," *Nat. Chem.*, vol. 7, pp. 703–711, 2015.

- [141] H. J. Snaith, "Perovskites: The Emergence of a New Era for Low Cost High Efficiency Solar Cells," *J. Phys. Chem. Lett.*, vol. 4, no. 21, pp. 3623–3630, 2013.
- [142] J. P. Mailoa, C. D. Bailie, E. C. Johlin, E. T. Hoke, A. J. Akey, W. H. Nguyen, M. D. McGehee, and T. Buonassisi, "A 2-terminal perovskite/silicon multijunction solar cell enabled by a silicon tunnel junction," *Appl. Phys. Lett.*, vol. 106, p. 121105, 2015.
- [143] C. D. Bailie, M. G. Christoforo, J. P. Mailoa, A. R. Bowring, E. L. Unger, W. H. Nguyen, J. Burschka, N. Pellet, J. Z. Lee, M. Grätzel, R. Noufi, T. Buonassisi, A. Salleo, and M. D. McGehee, "Semi-transparent perovskite solar cells for tandems with silicon and CIGS," *Energy Environ. Sci.*, vol. 8, pp. 956–963, 2015.
- [144] T. Todorov, T. Gershon, O. Gunawan, C. Sturdevant, and S. Guha, "Perovskite-kesterite monolithic tandem solar cells with high open-circuit voltage," *Appl. Phys. Lett.*, vol. 105, p. 173902. 1–5, 2014.
- [145] J. Luo, J.-H. Im, M. T. Mayer, M. Schreier, M. K. Nazeeruddin, N.-G. Park, S. D. Tilley, H. J. Fan, and M. Grätzel, "Water photolysis at 12.3% efficiency via perovskite photovoltaics and Earth-abundant catalysts," *Science*, vol. 345, no. 6204, pp. 1593–1596, 2014.
- [146] Y.-S. Chen, J. S. Manser, and P. V. Kamat, "All Solution-Processed Lead Halide Perovskite-BiVO₄ Tandem Assembly for Photolytic Solar Fuels Production," *J. Am. Chem. Soc.*, vol. 137, no. 2, pp. 974–981, 2015.
- [147] A. Barranco, A. Borrás, A. R. Gonzalez-Elipé, and A. Palmero, "Perspectives on oblique angle deposition of thin films: From fundamentals to devices," *Prog. Mater. Sci.*, vol. 76, pp. 59–153, 2016.
- [148] F. J. Ramos, M. Oliva-Ramirez, M. K. Nazeeruddin, M. Grätzel, A. R. Gonzalez-Elipé, and S. Ahmad, "Nanocolumnar 1-dimensional TiO₂ photoanodes deposited by PVD-OAD for perovskite solar cell fabrication," *J. Mater. Chem. A*, vol. 3, pp. 13291–13298, 2015.

2. Objectives

In the previous section, a short historical overview of different photovoltaic technologies, solar cells fundamentals and its working principles were summarized focusing on PSC in particular. A summary of principal properties of hybrid organic-inorganic lead halide perovskites with PV interest was also included, followed by principal perovskite deposition routes, PSC architectures and configurations and, lastly, some considerations for future commercialization.

Taking into account aforementioned evidences, exploration of novel alternatives for photoanodes and new HTMs with matching energetic levels compatible with perovskite are essential requirements for PSC cell optimization. Furthermore, the search of cost-effective materials, easy to fabricate compounds, and homogeneous and large scale feasible deposition techniques are also central requirements in order to drive a potential and realistic upscaling and future industrial application.

For that reason, the principal aim of this work was proposing and proving new photoanodes and innovative HTM for PSC fabrication.

More precisely, regarding new photoanode materials, since best performing devices are being still achieved with porous photoanodes based on non-expensive inorganic semiconductors using regular configuration, it was decided to keep the nature of the compounds but modifying the deposition technique employed. At lab scale, spin coating techniques are useful for research purposes. However, they are poorly reproducible, not able to be scaled and extremely time, energy and material consuming. Hence, the employment of porous inorganic semiconductor films prepared by dry chemistry techniques, with easy controllable conditions, homogeneous in large area and easy to scale as effective photoanodes in PSC was considered as a principal goal for the current study. Consequently, in this thesis, diverse alternatives were tested, suggesting ZnO nanowires, TiO₂ nanocolumns and 1-dimensional nanocolumnar photonic crystals (1-DPC) as PSC photoanodes. For each case, particular objectives can be detailed:

- ZnO nanowire-based photoanodes. Demonstration of ZnO nanowires films with porous structure grown by plasma-enhanced chemical vapor deposition (PECVD) as photoanodes in PSC was projected. Device optimization and characterization were also shown.
- TiO₂ nanocolumnar photoanodes. Proof of concept of tilted TiO₂ nanocolumnar films as porous photoanodes in PSC was demonstrated. Device optimization, study of morphological characteristics on final performance (*i.e.* porosity and thickness), infiltration of perovskite inside photoanode film and stability were analyzed.
- 1-DPC as photoanodes. Different mesoporous nanocolumnar multilayered films with alternating refractive indices were studied as photonic crystal like structures for light management in order to show improved absorption properties. Device integration, optimization and statistical analysis were accomplished as well.

On the other hand, new HTMs are needed to replace the expensive and hard to synthesize Spiro-OMeTAD and PTAA. Thus, implementation and optimization of unusual or original HTMs presenting easy synthesis and low cost are considered central tasks of this work. Moreover, in order to improve stability, some of the molecules were tested without dopants or additives (LiTFSI or t-BP), since long

term stability is reduced by those compounds though PV properties were enhanced. For the selected HTMs: TIPS-pentacene, Zn(II)octa(2,6-diphenylphenoxy) phthalocyanine (coded as TT80) and triazatruxene based HTMs (named as HMDI and HPDI), some particular objectives can be distinguished:

- TIPS-pentacene as HTM. For this case, testing an old existing molecule showing remarkable properties and reproducibility not only with but also without the use of additives was studied.
- Non-aggregated Zn(II) phthalocyanine as HTM. In this example, the proof of concept a metal-organic semiconducting phthalocyanines can work as HTM in PSC was desired. Device optimization and influence of diphenylphenoxy substituent were planned.
- Triazatruxene based compounds as HTM. HTMs based on triazatruxene core were tested in PSC. Their PV properties, stability, thermal properties and statistical analysis were also analyzed.

3. Global summary of results

More significant results obtained during this thesis are summarized in following chapter. Global discussions will be elucidated in chapter 4. Each subsection corresponds to one article, which can be found in appendix section in journal format.

3.1 PSC based on nanocolumnar plasma deposited ZnO thin films

Main figures and results regarding new porous nanocolumnar ZnO thin films as photoanodes for PSC are contained in this section. Information has been taken from the article text available as annex.

First of all, the new device architecture expected by the introduction of ZnO nanowires in regular (n-i-p) porous configuration is represented in Figure 3.1. In contrast, a scheme for standard regular (n-i-p) porous configuration using spherical semiconductor particles was depicted in introduction section (Figure 1.12a). The technique here selected to grow the nanocolumnar ZnO films was plasma enhanced chemical vapor deposition (PECVD) using diethyl zinc as precursor. Some of the advantages of implementing this technique are the absence of solvents during fabrication, the easy scalability and adequate uniformity over large areas making a good candidate for future industrial scale processes.

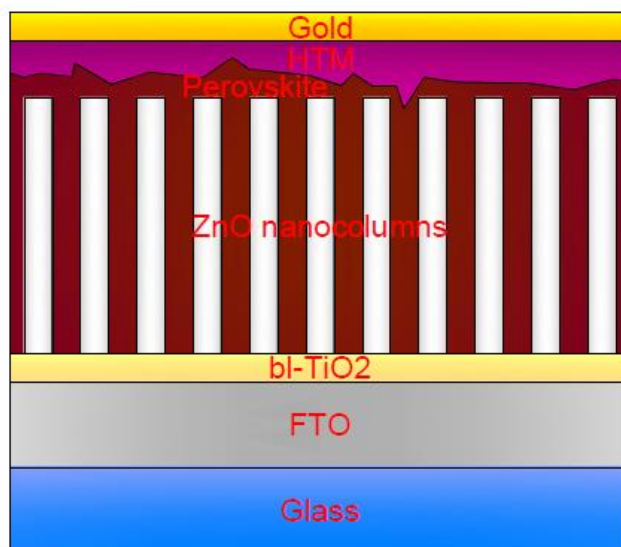


Figure 3.1. Schematic diagram of a device fabricated using ZnO nanocolumnar structures. Dimensions are not at scale.

In order to confirm the conceived structure, scanning electron microscopy images were developed. Cross-sectional and top view SEMs were prepared onto the photoanodes based on porous nanocolumnar ZnO thin films with different thicknesses (Figure 3.2a-c). In addition, a cross sectional SEM was prepared for the best performing device using 300 nm thick ZnO film.

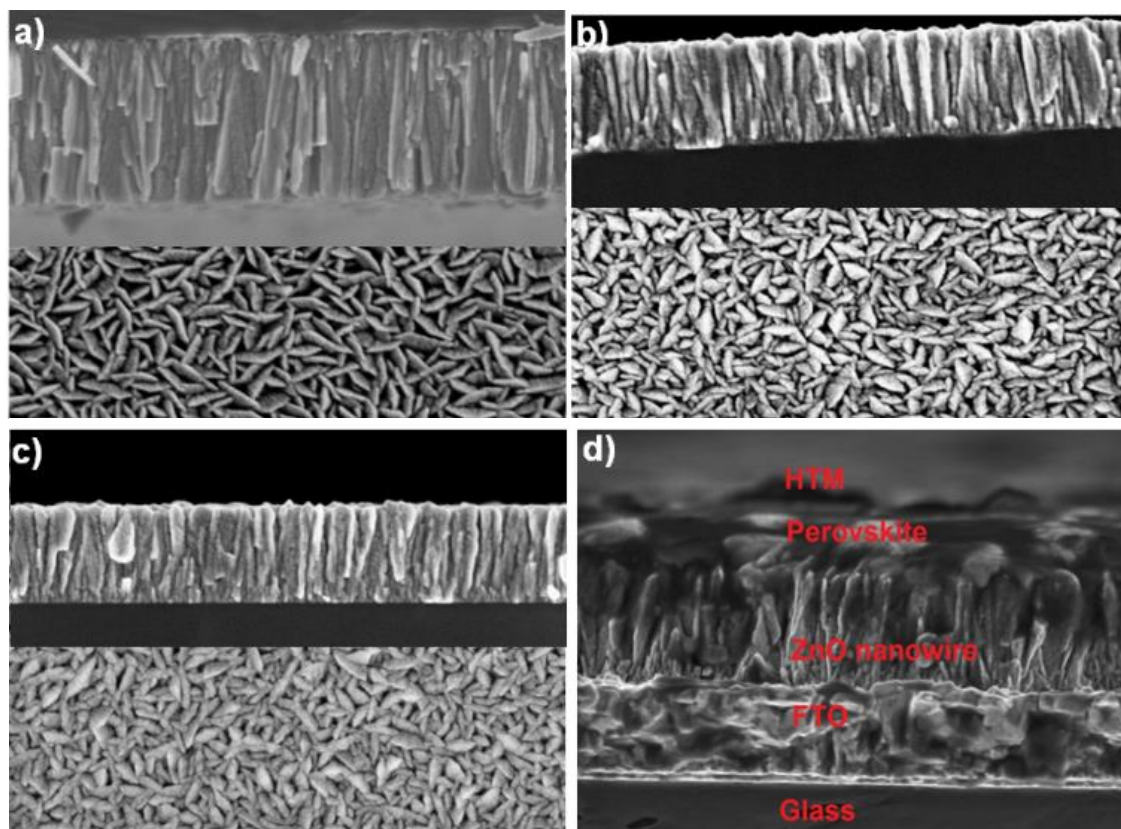


Figure 3.2. SEM images (cross-sectional and top view) of ZnO films of: a) 400, b) 500, and c) 600 nm thickness and d) cross-sectional images of fabricated solar-cell devices containing 300 nm-thick ZnO films.

Although nanocolumnar ZnO porous films with diverse thicknesses were prepared, only the ones with 300 nm were employed for device integration based on preliminary prospective analyses which reveal the best results with this thickness. These films were characterized by a high transparency and refractive index of 1.8 which denotes also its high porosity.

In this case, sequential deposition was utilized according introductory chapter. Different perovskite deposition conditions were explored, such as concentration of PbI_2 precursor, concentration of MAI solution for dipping and annealing temperature of perovskite film, analyzing its impact on device PV performance.

Results are summarized in Table 3.1. It was observed that Spiro-OMeTAD based devices ($\text{PCE}=3.9\%$, $J_{SC}=12.5 \text{ mA cm}^{-2}$, $V_{OC}=792 \text{ mV}$ and $\text{FF}=0.391$) showed better performance than PTAA based ones ($\text{PCE}=1.3\%$, $J_{SC}=8.3 \text{ mA cm}^{-2}$, $V_{OC}=481 \text{ mV}$ and $\text{FF}=0.327$) in similar conditions. After annealing temperature optimization, devices with Spiro-OMeTAD reached $\text{PCE}=4.8\%$, ($J_{SC}=16.0 \text{ mA cm}^{-2}$, $V_{OC}=718 \text{ mV}$ and $\text{FF}=0.412$).

3. Global summary of results

Table 3.1. Summary of the performances obtained employing different experimental conditions under 1 Sun (100 mW cm^{-2}) for PSC containing ZnO nanocolumnar photoanodes deposited by plasma-enhanced chemical vapor deposition (PECVD).

[PbI ₂] (M)	CH ₃ NH ₃ I concentration (mg mL ⁻¹)	Annealing temperature (°C)	HTM used	<i>J</i> _{sc} (mA cm ⁻²)	<i>V</i> _{oc} (mV)	FF	PCE (%)
1	8	70	Spiro-OMeTAD	12.5	792	0.391	3.9
1.25	8	70	Spiro-OMeTAD	5.3	660	0.321	1.2
1.35	8	70	Spiro-OMeTAD	1.4	631	0.350	0.3
1	10	70	Spiro-OMeTAD	6.0	761	0.406	1.9
1.25	10	70	Spiro-OMeTAD	2.7	621	0.397	0.7
1	8	100	Spiro-OMeTAD	16.0	718	0.412	4.8
1	8	70	PTAA	8.3	481	0.327	1.3

Furthermore, *J-V* curves both in dark and under 1 sun intensity for the optimized perovskite synthesis conditions (*i.e.* [PbI₂] = 1.25 M and 8 mg mL⁻¹ MAI concentration in 2-propanol) comparing different annealing temperatures are shown in Figure 3.3a. IPCE characteristic for champion device is also included (Figure 3.3b).

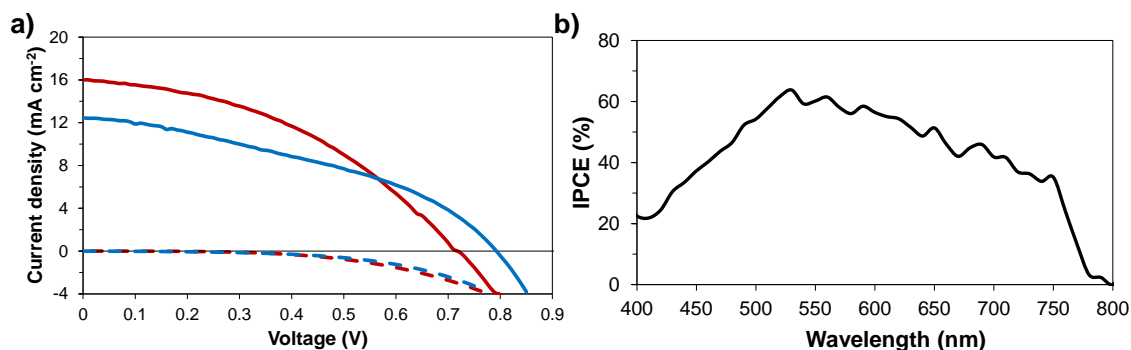


Figure 3.3. a) *J-V* curves of the fabricated devices. Blue line show a cell annealed at 70°C whereas red line represent a cell annealed at 100°C, being both deposited using [PbI₂] = 1.25M, 8 mg mL⁻¹ MAI concentration in 2-propanol. The corresponding dark currents are represented by dotted lines and b) IPCE of the ZnO nanocolumnar structure with CH₃NH₃PbI₃ solar cells.

Finally, more detailed discussions can be found in discussion section and in the main article attached in appendix part.

3.2 Nanocolumnar 1-dimensional TiO₂ photoanodes deposited by PVD-OAD for PSC fabrication

The main aim of this work consisted on the implementation of a new type of nanocolumnar TiO₂ structures (NC-TiO₂) deposited by physical vapor deposition at oblique incidence angle (PVD-OAD) creating a tilted NC-TiO₂ porous photoanodes for PSC preparation. The utilization of a solvent-free technique was introduced in order to minimize operational costs and permitting homogeneous and controlled growth conditions over big deposition areas.

An explicative scheme of the technique employed is depicted in Figure 3.4a, where it is observed by controlling the position of the sample and the distance to the source, the incidence glancing angle (α) is tuned. In addition a schematic representation of PSC using the tilted nanocolumns as photoanode is included as well (Figure 3.4b).

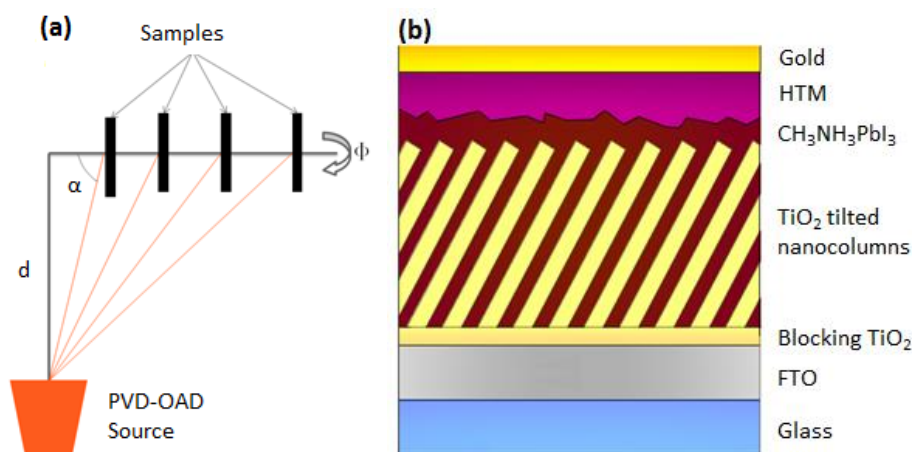


Figure 3.4. a) Schematic configuration for the physical vapor deposition at glancing incidence (PVD-OAD) technique used for titania nanocolumnar films and b) schematic representation of the PSC using the tilted nanocolumns as photoanode.

A characteristic of PVD-OAD technique is by varying the incidence glancing angle (α), the tilting angle of the deposited column (β) is modified and then, the porosity of the film can be tuned with precision according the desired requirements. In the present study, several thicknesses and porosities were tested by varying the deposition time and incidence angle (α) respectively in tilted NC-TiO₂ porous films. For an evaporation angle $\alpha=70^\circ$ a real tilting angle $\beta\sim 34^\circ$ is expected, while when $\alpha=85^\circ$ the columns are expected to be more tilted ($\beta\sim 47^\circ$). Afterwards, those structures were employed as photoanodes in PSC being analyzed their morphologies and the influence of photoanodes over photovoltaic properties.

For morphological characterization, SEM images were recorded (Figure 3.5). In Figure 3.5a and 3.5b cross sectional SEM images for tilted NC-TiO₂ porous films with different α are included to compare the changes in tilting angle (β) and appreciate the variation in the porosity when the deposition angle is tuned. Top view SEM images for NC-TiO₂ before and after perovskite deposition are included in Figures 3.5c and 3.5d. Both cross sectional SEM for a NC-TiO₂ film with perovskite infiltrated and for a full device are also studied to observe the complete

infiltration of perovskite across the NC-TiO₂ porous film. For visualization the thickness of each layer, cross sectional SEMs of a device after perovskite infiltration and for a final device are presented in Figure 3.5e and 3.5f respectively.

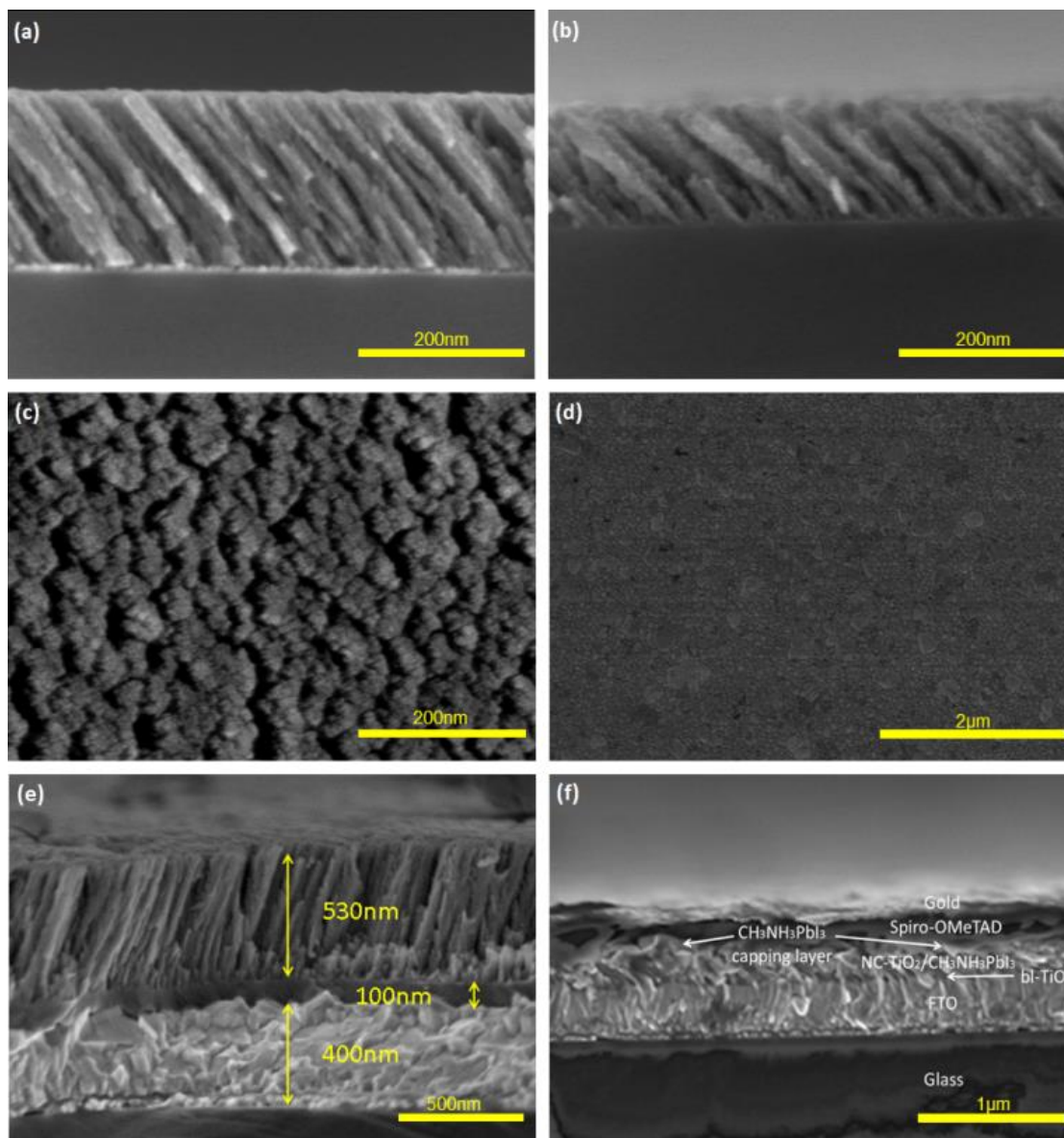


Figure 3.5. Cross sectional scanning electron microscopy (SEM) images of a) TiO₂ tilted nanocolumnar TiO₂ photoanode deposited by PVD-OAD with 70° as glancing angle (α), b) cross section of the NC-TiO₂ film deposited with 85° as α , c) top view image of the NC-TiO₂ film, d) top view of the perovskite formed over the NC-TiO₂ film, e) cross sectional SEM image of NC-TiO₂ film with perovskite infiltrated and f) cross sectional SEM image of full device. Note the Figure 3.5a is focused and zoomed.

For the sample (Figure 3.5e) composed by bi-TiO₂/NC-TiO₂/perovskite, time-of-flight secondary ion mass spectrometry (ToF-SIMS) measurements were performed in order to confirm the elemental distribution of the different materials along the cross section of the sample. Thus, the infiltration of perovskite inside the porous matrix made of NC-TiO₂ can be studied. In the following Figure 3.6, results of ToF-SIMS are included for the species with interest: Ti⁺, Sn⁺, Pb⁺, PbO⁺, SiO⁺, I⁺ NH₃⁺

and NH_4^+ . Different zones can be appreciated which correspond with the different layers deposited.

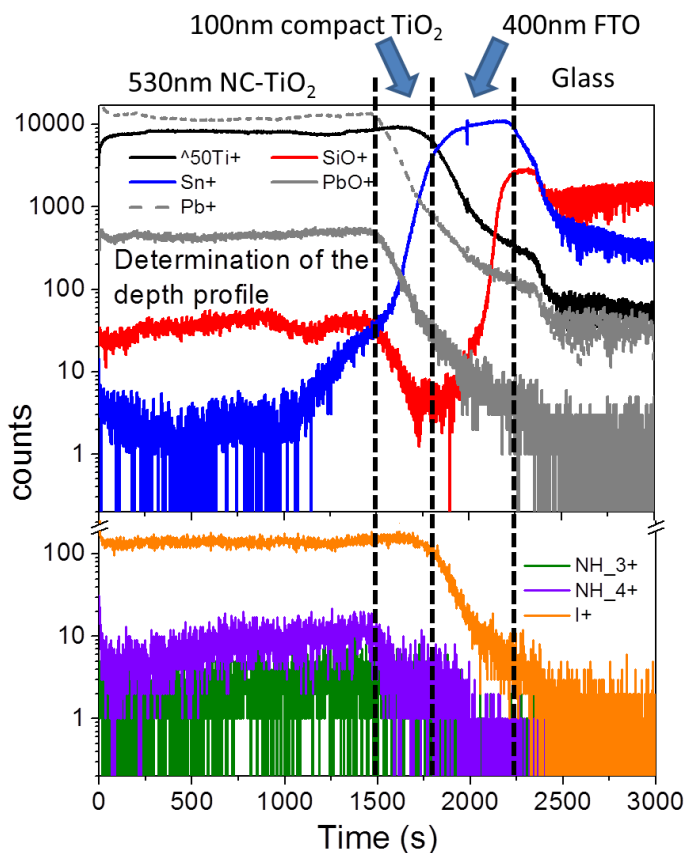


Figure 3.6. Time of flight secondary-ion mass spectrometry (ToF-SIMS) profiles for Ti^+ , SiO^+ , Sn^+ , PbO^+ , Pb^+ , I^+ and NH_3^+ (NH_4^+) species proving the homogenous distribution of the perovskite through the porous structure of the 530 nm thick bi-TiO₂/NC-TiO₂/CH₃NH₃PbI₃ film.

After that, photovoltaic characterization was made to analyze the influence of photoanode morphology, *i.e.* thickness and porosity (controlled by tuning α), in the final PV performance of the PSC.

In Table 3.2, photovoltaic parameters (J_{SC} , V_{OC} , FF, PCE and R_s) are shown for the best performing device prepared with each type of photoanode configuration: thicknesses, deposition glancing angle (α) and HTM employed. Variation of the photovoltaic properties with thickness and porosity of the tested photoanodes is depicted in Figure 3.7, finding an optimum using 200 nm thick at $\alpha=85^\circ$.

Statistical information, $J-V$ characterization curves and IPCE can be consulted in the Appendix section.

3. Global summary of results

Table 3.2. Performance of the perovskite sensitized solar cells fabricated employing TiO₂ tilted nanocolumns as photoanodes. Different photoanode thicknesses, evaporation angles (α) and two different HTMs were employed. Sun Intensity is expressed as percentage of 1 Sun (AM1.5G).

Thickness (nm)	Evaporation angle, α (°)	HTM	Sun Intensity (%)	J_{sc} (mA cm ⁻²)	V_{oc} (mV)	FF	PCE (%)	R_s (Ω cm ²)
100	70	Spiro-OMeTAD	95.5	10.57	867.3	0.632	6.06	15.38
100	85	Spiro-OMeTAD	95.7	6.04	857.4	0.600	3.24	43.02
200	70	Spiro-OMeTAD	96.0	14.39	972.9	0.637	9.29	12.04
200	85	Spiro-OMeTAD	96.1	16.68	949.8	0.639	10.53	11.71
300	70	Spiro-OMeTAD	99.6	18.25	949.0	0.588	10.22	12.13
300	85	Spiro-OMeTAD	95.6	18.02	849.7	0.609	9.75	10.05
500	70	Spiro-OMeTAD	96	15.67	800.2	0.523	6.82	17.13
200	70	PTAA	95.7	7.29	825.3	0.576	3.62	25.38

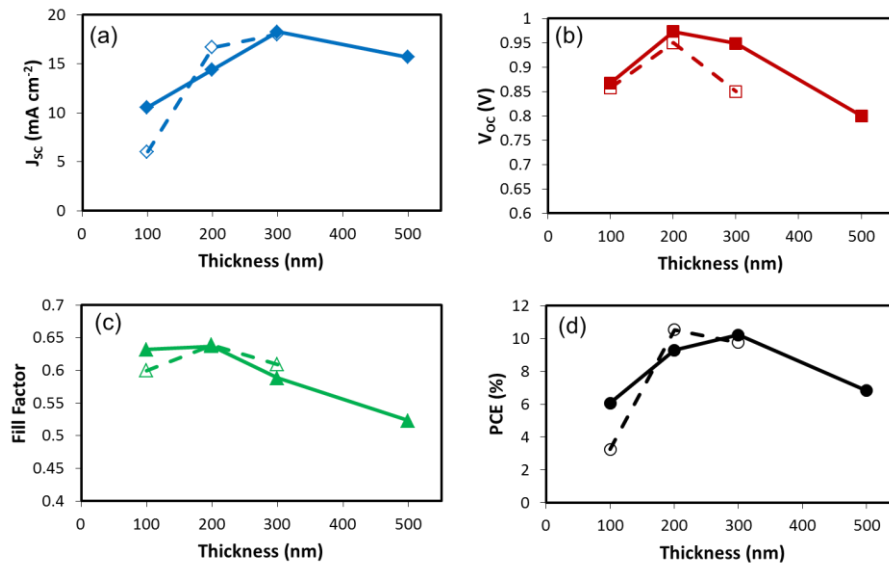


Figure 3.7. a) Short-circuit current (J_{sc}), b) open-circuit voltage (V_{oc}), c) fill factor (FF) and d) power conversion efficiency (PCE) shown for the perovskite sensitized solar cells depending the thickness and angle of the TiO₂ photoanodes. Solid rhombus, squares, triangles and circles linked with solid lines were prepared with 70° as evaporation glancing angle (α). Hollow rhombus, squares, triangles and circles linked with dashed lines were prepared with 85° as evaporation glancing angle (α).

Finally, the stability of the PSC containing porous NC-TiO₂ photoanodes was compared with standard mp-TiO₂ based ones, being depicted in Figure 3.8.

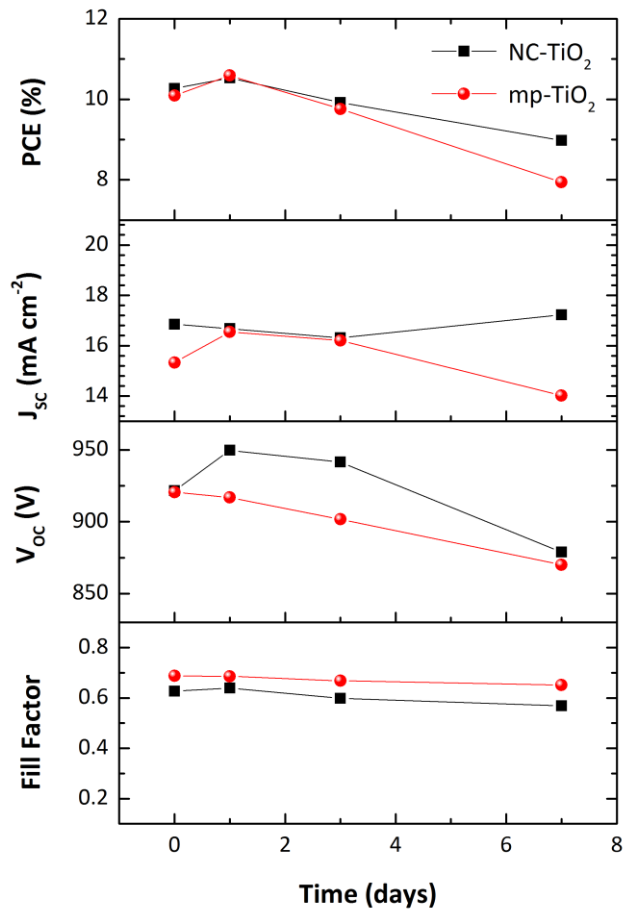


Figure 3.8. Evolution of the photovoltaic parameters (PCE, J_{sc} , V_{oc} and FF) for NC-TiO₂ photoanodes and standard mp-TiO₂ ones at AM1.5G at 100 mW cm⁻² with time.

3.3 Porous 1-dimensional nanocolumnar structures as effective photonic crystal for PSC

Based on PVD-OAD technique explained in previous section, new photonic crystal like structures were conceived as new porous nanocolumnar photoanode structures for PSC with improved absorption properties. As shown earlier, with the control of incidence glancing angle (α), the real tilting angle of the column (β) is varied resulting in a modification of the porosity of the monolayer. Thus, when the porosity of the film is increased, the refractive index of the film (n) is reduced accordingly. Therefore, adjusting the refractive index of each monolayer (either modifying the porosity or changing the deposited material), its thickness and the total number of monolayers, photonic crystal like structures can be created controlling the location in the spectra and depth of the desired photonic bandgap by alternating an even number of monolayers with high and low refractive indices.

Consequently, three different types of porous nanocolumnar photonic crystal like films were used as photoanodes in PSC with improved optical properties. A scheme of the different architectures here studied is depicted below (Figure 3.9).

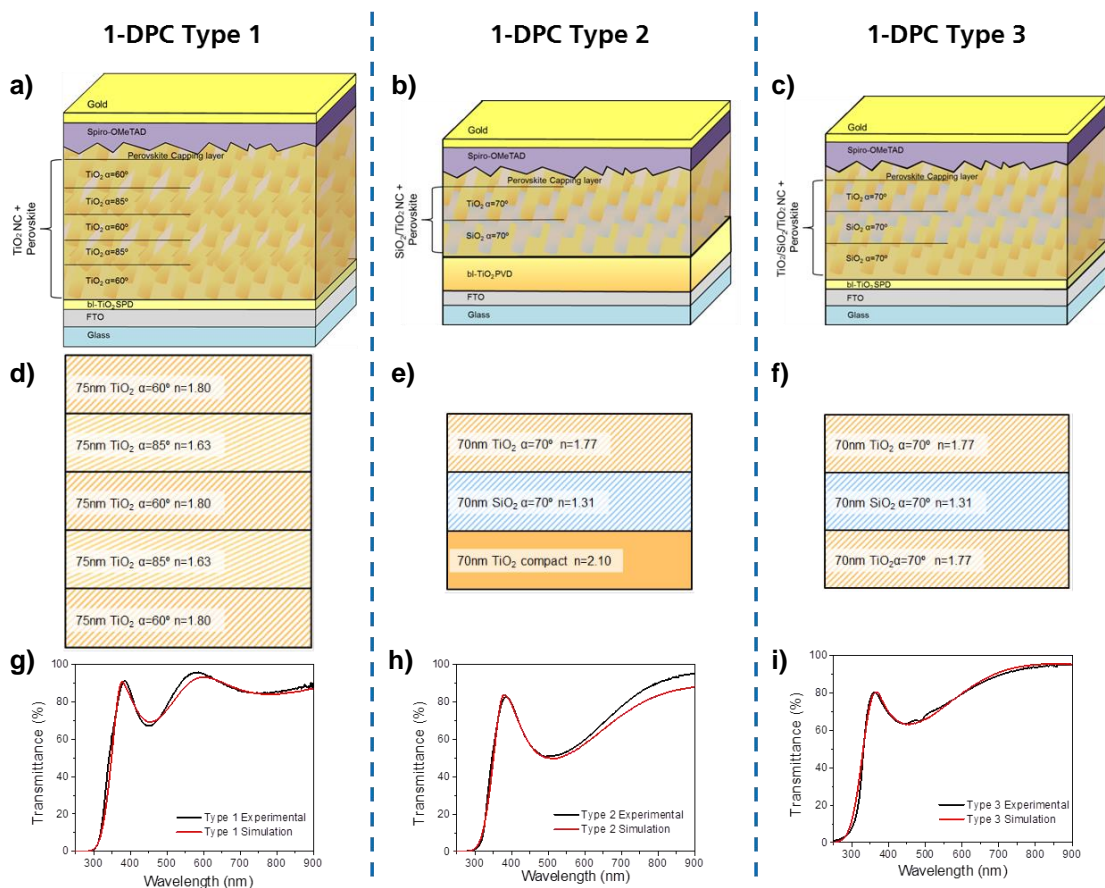


Figure 3.9. a-c) Architectures of the final devices containing photonic crystal Type 1, 2 and 3 respectively (not at scale), d-f) schematic representation of the photonic crystals type 1, 2 and 3 respectively indicating composition of the film, thickness, deposition glancing angle (α) and refractive index of each monolayer and g-i) experimental transmittance measurements (black lines) and simulations (red ones) for the different 1-DPC structures over quartz.

Photonic crystal type 1 (PC1) consist on five layers of TiO_2 nanocolumnar films 75 nm thick with alternating refractive index (1.80 and 1.63) over a TiO_2 buffer layer (bl- TiO_2). The alternation in refractive index for photonic crystal type 2 (PC2) and type 3 (PC3) was induced by alternating columnar structures with same porosity but made of different materials (SiO_2 and TiO_2). PC2 is composed by one dense TiO_2 layer with $n=2.10$ followed by porous SiO_2 ($n=1.31$) and porous TiO_2 ($n=1.77$). In PC3, porous TiO_2 /porous SiO_2 /porous TiO_2 ($n=1.77/n=1.31/n=1.77$) are deposited onto a bl- TiO_2 .

In order to confirm the projected morphology of the layers, cross-sectional field effect SEM (FE-SEM) measurements were made for photonic crystal based samples over silicon wafer. In Figure 3.10, a schematic picture of the technique is depicted in Figure 3.10a while a ~ 300 nm thick NC- TiO_2 film ($\alpha=70^\circ$) employed as reference in this work, similar with the films prepared in previous section 3.2. Figures 3.10c, e and g shows the back scattered electrons SEM showing distributions in composition while secondary electron SEM are depicted in Figures 3.10d, f and g to distinguish the morphology.

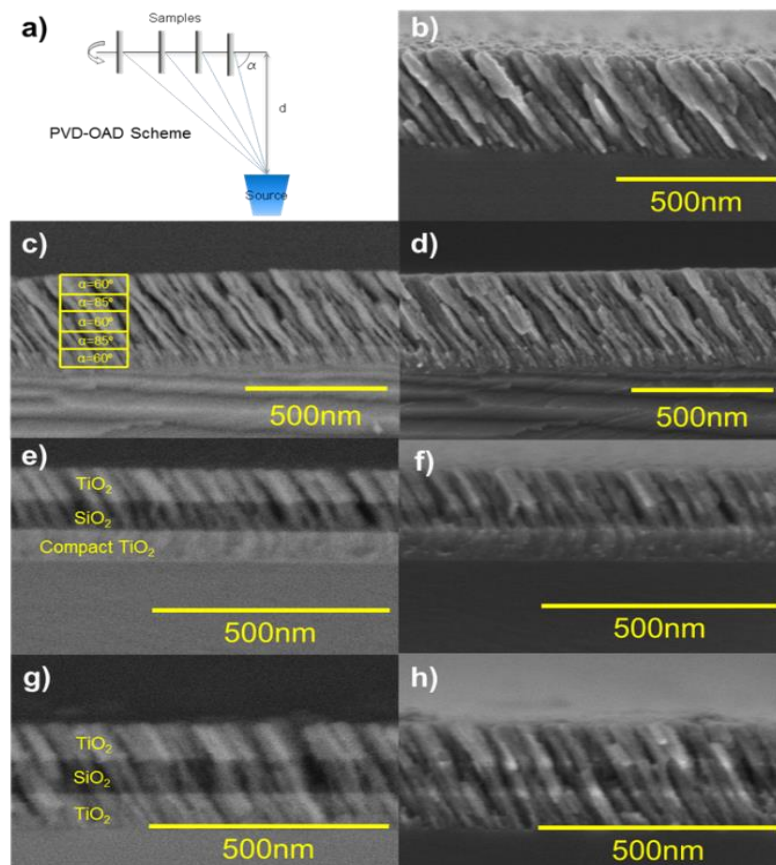


Figure 3.10. a) Schematic representation of the Physical Vapor Deposition at Oblique Angle (PVD-OAD) technique here employed to fabricate photonic crystal architectures, b) cross sectional field effect scanning electron microscopy images (FE-SEM) using secondary electrons for 300 nm thick straight TiO_2 ($\alpha=70^\circ$) nanocolumns prepared onto silicon wafer, c-d) cross FE-SEM using back scattered electrons and secondary electrons respectively for Photonic Crystal type 1 over Si, e-f) cross FE-SEM of back scattered electrons and secondary electrons respectively for PC2 over Si, g-h) cross FE-SEM by back scattered electrons and secondary electrons respectively for PC3 over Si.

A scheme explaining the spatial distribution of the square of electrical field caused by a porous photonic crystal structures over FTO, similar with the ones here prepared is included in Figure 3.11 to illustrate the dominant behavior which is considered to provoke the enhancement of harvesting and absorbing properties for the PSC.

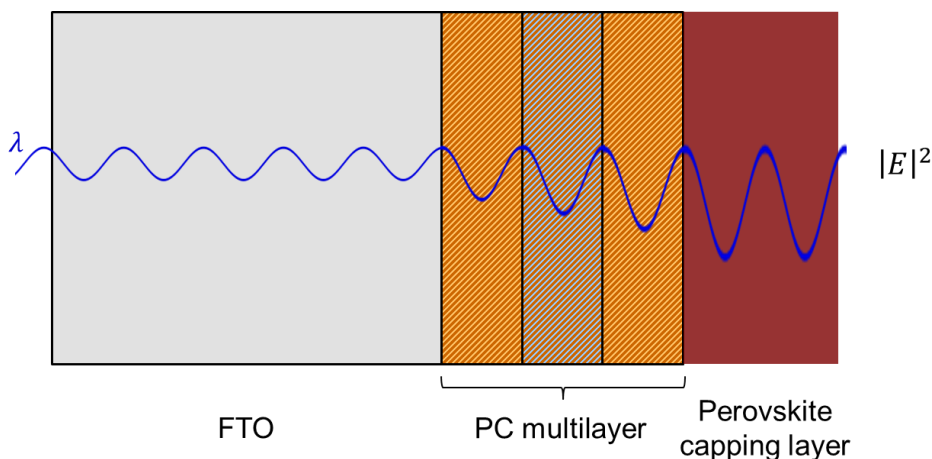


Figure 3.11. Schematic representation of the spatial distribution of the square amplitude of the electric field for a photonic crystal like structure composed of three layers over FTO.

After optical measurements of PC structures, perovskite was infiltrated inside porous photoanodes followed by HTM and cathode deposition. Once the device fabrication is finished $J-V$ and IPCE measurements were made to analyze PV properties of the photonic crystals containing PSC. In Table 3.3 PV parameters such as J_{SC} , V_{OC} , fill factor and PCE are detailed for each type of PC based configuration and also for reference showing mean \pm standard deviation (SD) and best value between brackets. Both $J-V$ and IPCE curves for champion device with each configuration are depicted in Figure 3.12.

Table 3.3. Summary of the photovoltaic parameters (J_{SC} , V_{OC} , FF and PCE) obtained for the different PSC here studied including 1-DPC transparent photoanodes and its comparison with similar structures where photonic crystal effect is not expected. Values are expressed as mean \pm SD and maximum values obtained are between brackets.

Configuration	J_{SC} (mA cm ⁻²)	V_{OC} (mV)	FF	PCE (%)
NC-TiO ₂ [148]	17.87 \pm 0.53 (18.25)	934.4 \pm 10.7 (949.0)	0.568 \pm 0.018 (0.588)	9.56 \pm 0.37 (10.22)
PC1	18.56 \pm 0.55 (19.29)	867.7 \pm 11.9 (928.9)	0.615 \pm 0.036 (0.659)	10.05 \pm 0.69 (10.94)
PC2	15.05 \pm 1.15 (16.68)	883.1 \pm 60.3 (954.9)	0.312 \pm 0.060 (0.396)	4.28 \pm 1.32 (6.39)
PC3	18.44 \pm 0.32 (18.77)	1026.1 \pm 5.5 (1032.0)	0.603 \pm 0.012 (0.617)	11.52 \pm 0.30 (12.03)

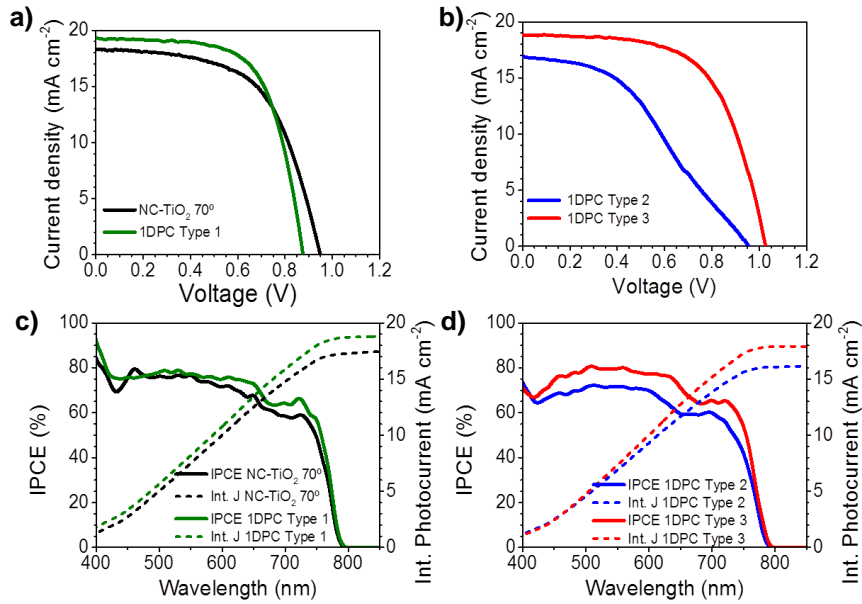


Figure 3.12. a) J - V characterization of the PSC containing TiO_2 tilted nanocolumns at $\alpha=70^\circ$ (black) and PC1 (green), b) J - V characterization of the PSC containing PC2 (blue) and PC3 (red), c) IPCE spectra for the PSC with TiO_2 tilted nanocolumns at $\alpha=70^\circ$ (black) and PC1 (green), and d) IPCE spectra for the PSC with PC2 (blue) and PC3 (red).

The statistical results for PV parameters are summarized as box-whiskers chart as well in following Figure 3.13.

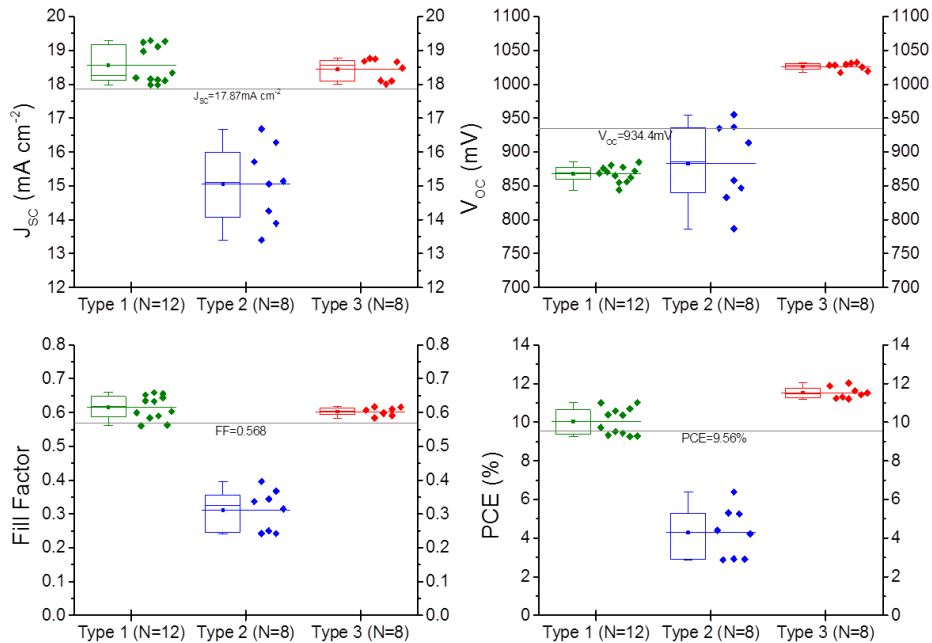


Figure 3.13. Box-whiskers plot which shows all the photovoltaic magnitudes for the different devices containing 1-DPC porous structures: PC1 (green), PC2 (blue) and PC3 (red). Grey lines represent the average values for each magnitude in the case of base NC- TiO_2 photoanode. Dots at the right side of the box mean the exact value of each sample.

3.4 A dopant free linear acene derivative as a HTM for PSC

The replacement of Spiro-OMeTAD as HTM in PSC for other alternatives which present frontier orbitals compatible with perovskite (*i.e.* HOMO level higher than perovskite valence band), potentially less expensive, easier to synthesize and can work as dopant free in order to maximize the stability of the solar cells is a necessary requirement inside this field. In the present work, we have implemented for first time a high mobility organic semiconductor as HTM into PSC: 6,13-bis(triisopropylsilyl)ethynyl)pentacene (TIPS-pentacene) with and without additives.

In Figure 3.14a, TIPS-pentacene molecular structure is represented. To analyze the optical band gap and HOMO/LUMO levels of TIPS-pentacene, optical absorption and cyclic voltammetry measurements were made. In Figure 3.14b, cyclic voltammetry measurements are shown for pristine TIPS-pentacene, for TIPS-pentacene with additives (LiTFSI + t-BP) and for Spiro-OMeTAD. Results obtained for band gap, and frontier orbitals are summarized in Table 3.4 while the energy level diagram of the PSC containing TIPS-pentacene is shown in Figure 3.14c. In addition conductivity of TIPS-pentacene in film has been studied, showing 3.5×10^{-7} S cm⁻¹ for pristine TIPS-pentacene while after the addition of the additives it was 1.0×10^{-5} S cm⁻¹. Glass transition (T_g) temperature of TIPS-pentacene was evaluated by DSC and found to be $T_g = 122^\circ\text{C}$.

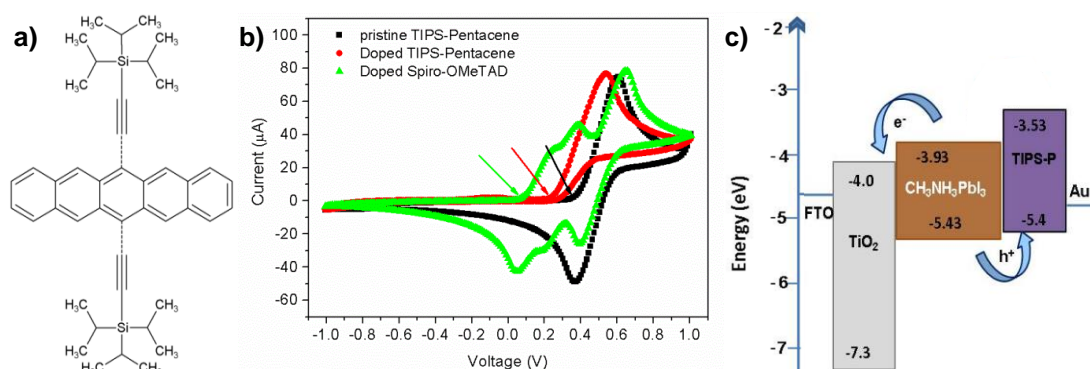


Figure 3.14. a) Chemical structure of TIPS-pentacene, b) cyclic voltammograms of Spiro-OMeTAD and TIPS-pentacene in pristine form and with LiTFSI dopant and t-BP additive in dichloromethane solvent and c) corresponding energy level diagram for PSC containing TIPS-pentacene as HTM.

Table 3.4. Summary of electrochemical and optical parameters of TIPS-pentacene and Spiro-OMeTAD.

HTM	$E_{g\ opt}^a$ (eV)	$E_{\frac{1}{2}\ ox}^b$ (V)	HOMO (eV)	LUMO ^b (eV)
Pristine TIPS-pentacene	1.87	0.488	-5.4	-3.53
Spiro-OMeTAD	2.98	0.156	-5.07	-2.09

^aOptical band gap ($E_{g\ opt}$) was calculated by onset of optical absorption. ^b $LUMO = HOMO + E_{g\ opt}$.

Once the energy levels of TIPS-pentacene have been studied demonstrating its usefulness, it was as HTM in PSC, and devices were fabricated. To study the morphology and thickness of the fabricated PSC, cross sectional SEM pictures of PSC containing TIPS-pentacene as HTM are presented in Figure 3.15.

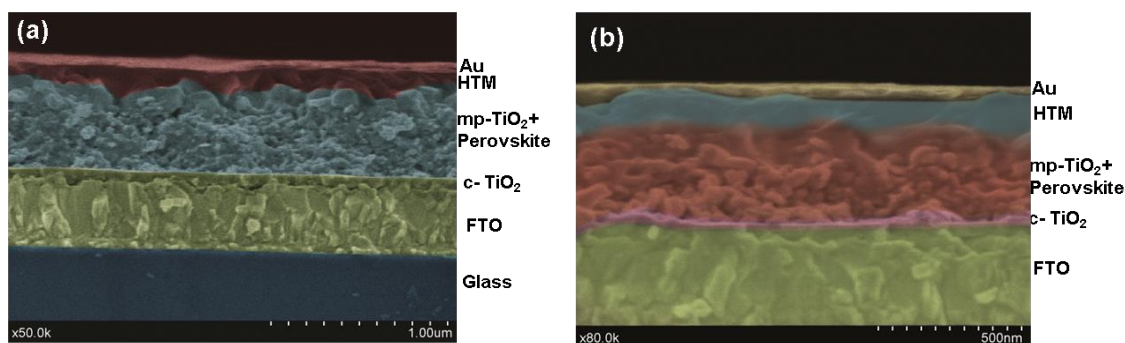


Figure 3.15. Cross-sectional SEM of the $\text{CH}_3\text{NH}_3\text{PbI}_3$ perovskite based device with pristine TIPS-pentacene HTM, a) at 1 μm scale with low magnification and b) at 500 nm scale with higher magnification. Both images shows a clear interface between TIPS-pentacene and perovskite layer. Colors were applied to distinguish easily the different layers.

Subsequently, photovoltaic characteristics of this PSC were analyzed. In Table 3.5 PV properties (J_{SC} , V_{OC} , FF, PCE) expressed as mean \pm SD (standard deviation) for the solar cells containing different HTMs: TIPS-pentacene without additives, with additives and Spiro-OMeTAD as reference. Both J - V characterization and IPCE curves for a cell with average properties are shown in Figure 3.16 for each type of HTM here employed.

Table 3.5. Photovoltaics parameters derived from J - V measurements of mesoporous $\text{CH}_3\text{NH}_3\text{PbI}_3$ perovskite based devices with TIPS-pentacene and Spiro-OMeTAD as HTM^a.

Device	J_{SC} (mA cm^{-2})	V_{OC} (mV)	FF	PCE (%)
Pristine TIPS-pentacene	20.84 \pm 0.01	913 \pm 5	0.60 \pm 0.01	11.51 \pm 0.31
TIPS-pentacene + LiTFSI + t-BP	16.51 \pm 0.49	920 \pm 4	0.54 \pm 0.01	8.20 \pm 0.23
Spiro-OMeTAD + LiTFSI + t-BP	18.61 \pm 0.78	843 \pm 5	0.62 \pm 0.01	9.77 \pm 0.35

^aAverage data with standard deviation were based in a single batch. Devices were masked with a black aperture to define the active area of 0.283 cm^2 .

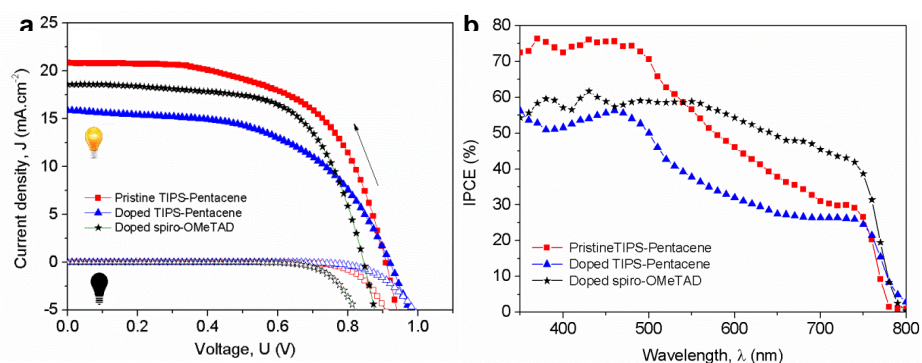


Figure 3.16. a) J - V characteristics of a $\text{CH}_3\text{NH}_3\text{PbI}_3$ perovskite based device with average performance for pristine TIPS-pentacene (red), TIPS-pentacene with additives (blue) and Spiro-OMeTAD (black) as HTM in dark (hollow symbols) and under illumination at AM 1.5G (filled symbols), 100 mW cm^{-2} in a reverse bias scan; and b) corresponding IPCE spectra of the devices.

Additionally, it is interesting to note the champion device was obtained from additive free TIPS-pentacene and it reached a PCE=11.82% presenting negligible hysteresis (see appendix section) and with remarking PV properties: J_{SC} =20.86 mA cm⁻², V_{OC} =918 mV and a fill factor of FF=0.62.

Finally, for further information, such as thermal characterization of TIPS-pentacene compound and hysteresis analysis, stability and statistical information of TIPS-pentacene containing PSC can be consulted in Appendix section.

3.5 Non-aggregated Zn(II)octa(2,6-diphenylphenoxy) phthalocyanine as a HTM for efficient PSC

In order to find novel compounds with interesting properties, capable to be used as HTM in PSC, a new phthalocyanine based compound: Zn(II)octa(2,6-diphenylphenoxy) phthalocyanine (coded as TT80) was tested. Molecular structure of TT80 compound is depicted in Figure 3.17a while absorption spectrum of the molecule in chloroform is shown in Figure 3.17b.

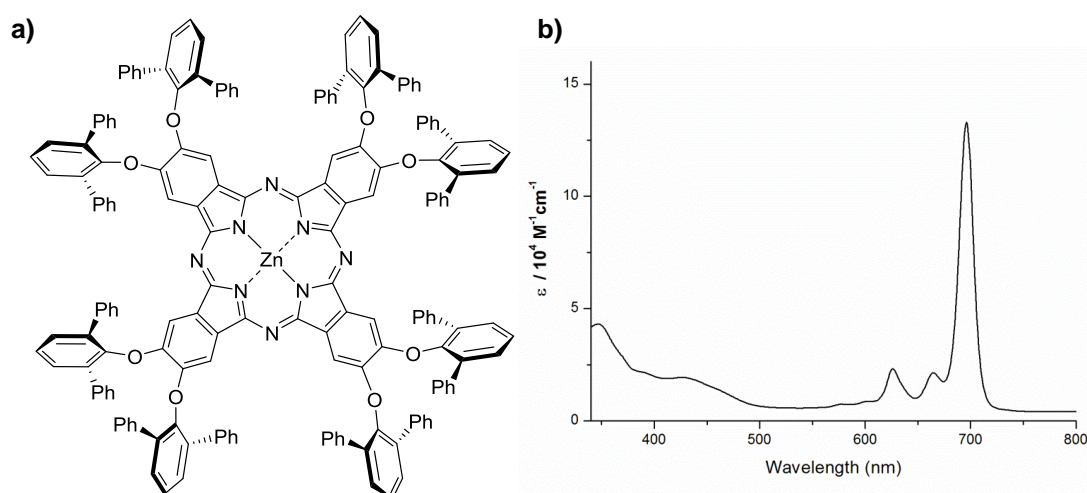


Figure 3.17. a) Molecular structure of TT80, b) UV-Vis absorption spectrum of TT80 in CHCl_3 solution ($\sim 1 \times 10^{-5}$ M).

After device integration, photovoltaic characteristics of PSC containing TT80 as HTM were analyzed through J - V and IPCE characterization. Three different deposition configurations were tested: pristine TT80 in Chlorobenzene, TT80 with additives (LiTFSI and t-BP) in chlorobenzene and additive add TT80 (with LiTFSI and t-BP) in toluene. In Table 3.6 photovoltaic parameters for champion cells in each configuration are detailed.

Table 3.6. Photovoltaic parameters^a obtained for the PSC employing phthalocyanine as hole-transporting materials (HTMs). P_{in} , incident intensity of simulated AM1.5G solar light^b

Additives	Uptake Solvent	P_{in} (mW cm^{-2})	J_{SC} (mA cm^{-2})	V_{OC} (mV)	FF	PCE (%)
-	Chlorobenzene	96.8	11.90	578	0.362	2.6
LiTFSI + t-BP	Chlorobenzene	97.4	16.35	797	0.503	6.7
LiTFSI + t-BP	Toluene	97.4	16.91	796	0.450	6.2

^aThe values presented were obtained for the best device in each configuration. For each configuration, several devices of equal quality were tested, and the uncertainties of PCE values were within 1–6% (see Table S1 in the Appendix section). ^b $P_{in} = 100 \text{ mW cm}^{-2}$ for 1 sun irradiation.

J - V curves for each champion cell previously reported are plotted in Figure 3.18a. IPCE curve for the optimized configuration, *i.e.* for TT80 + LiTFSI + t-BP using toluene as uptake solvent is found in Figure 3.18b.

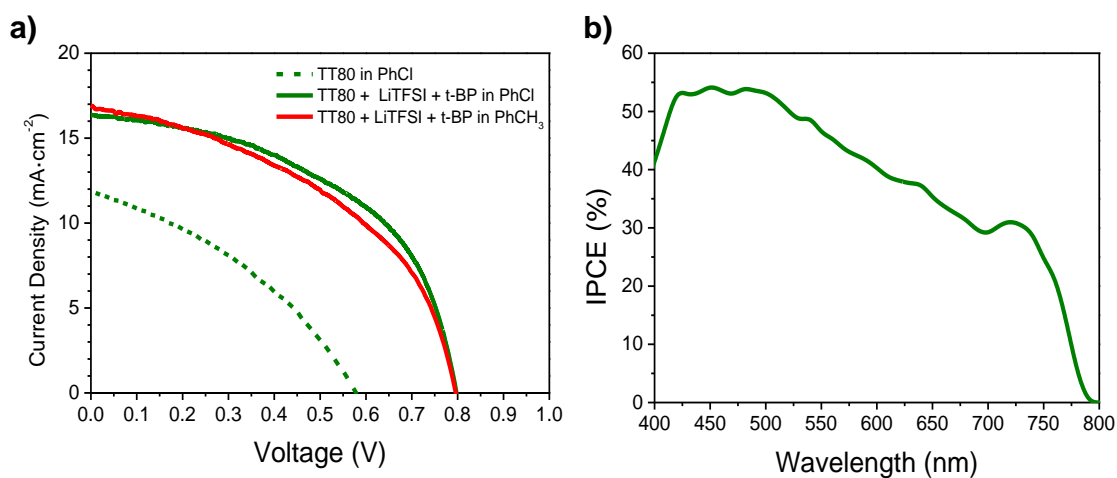


Figure 3.18. a) J - V curves under simulated full sun illumination (AM1.5G) for the three cells made with TT80 as HTM using different solvents and additives (PhCl = chlorobenzene; PhCH₃ = toluene) and b) IPCE for the best cell made with TT80 under optimized configuration (TT80 + LiTFSI + t-BP in PhCl).

Detailed photovoltaic parameters with statistical information for all the devices fabricated, current dynamic spectrum of TT80/PSC, copy of ¹H NMR, MS and HRMS spectra of TT80 can be consulted in Appendix section where calculations to evaluate the molecular weight of TT80 molecule revealed a value of 2528.8g mol⁻¹.

3.6 Rational design of triazatruxene based hole conductors for PSC

Persevering with the aim of finding new potentially low-cost materials with HOMO levels compatible with perovskite to be implemented in stable and efficient PSC, two novel compounds based on triazatruxene molecule, with substituents to obtain the necessary solubility to be deposited through solution process were proposed: 5,10,15-Trihexyl-3,8,13-trimethoxy-10,15-dihydro-5H-diindolo [3,2-a:30,20-c]carbazole (HMDI) and 5,10,15-Tris(4-(hexyloxy)phenyl)-10,15-dihydro-5H-diindolo [3,2-a:30,20-c]carbazole (HPDI), observing a very high solubility for both ($>100 \text{ mg mL}^{-1}$). Figure 3.19 shows the synthetic route scheme for both compounds.

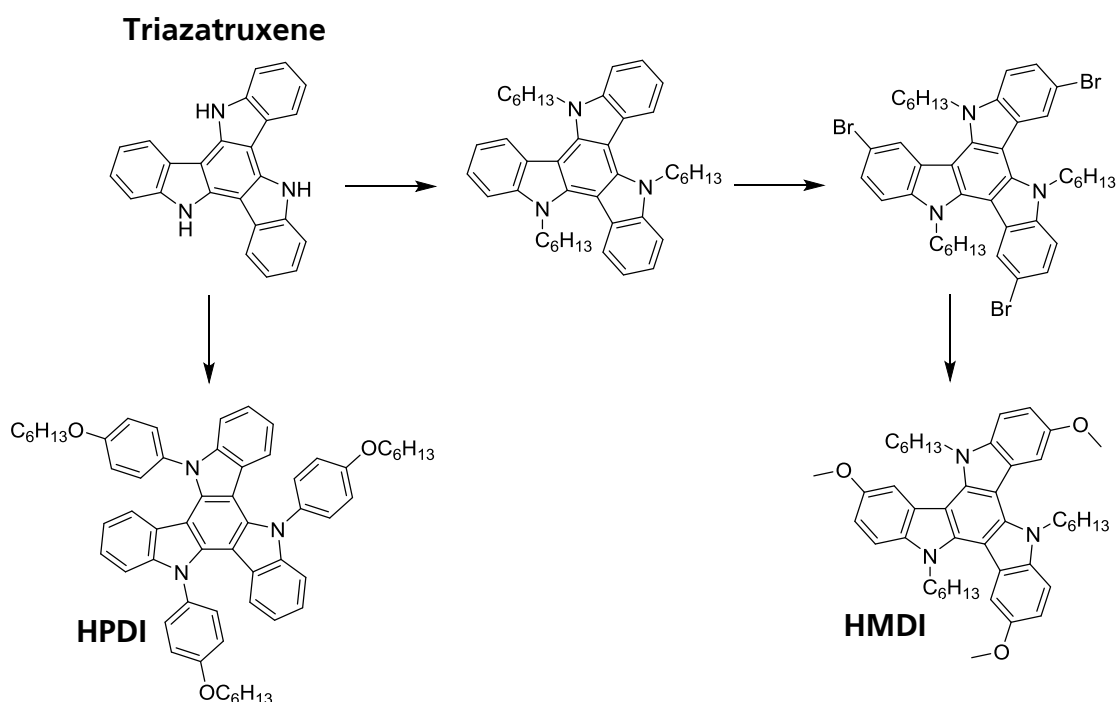


Figure 3.19. Synthetic route for the HMDI and HPDI HTMs.

In order to evaluate the band gap and frontier orbitals: HOMO/LUMO of these molecules, UV-Vis absorption spectra and cyclic voltammetry experiments were developed. In Table 3.7, band gap and molecular orbitals for HMDI and HPDI obtained by those experiments are detailed; glass transition temperature (T_g) attained by differential scanning calorimetry (Appendix section) is also reported. In Figure 3.20, absorbance spectra and cyclic voltammetry plots for triazatruxene based compounds are included together with an energy level diagram for the here fabricated PSC.

3. Global summary of results

Table 3.7. Summary of optical, electrochemical and thermal properties for the studied HTMs.

Compound	λ_{onset}^a (nm)	$E_{g\ opt}^b$ (eV)	$E_{\frac{1}{2}ox\ vs\ Fc^+/Fc}^c$ (eV)	HOMO ^d (eV)	LUMO ^e (eV)	T_g^f (°C)
HMDI	395	3.14	0.108	-5.17	-2.03	1
HPDI	380	3.26	0.344	-5.41	-2.15	36

^aAbsorption spectra measured in dichloromethane solution. ^bOptical band gap ($E_{g\ opt}$) was calculated by onset of optical absorption. ^c $E_{\frac{1}{2}ox\ vs\ Fc^+/Fc}$ was calculated from Cyclic Voltammetry as $E_{\frac{1}{2}ox\ vs\ Fc^+/Fc} = \frac{1}{2}(E_{pa} + E_{pc})$.

^dHOMO was calculated as: $HOMO = -\left(E_{\frac{1}{2}ox\ vs\ Fc^+/Fc} + 5.064\right)$ in eV. ^eLUMO = $HOMO + E_{g\ opt}$.

^f T_g glass transition temperature calculated from DSC.

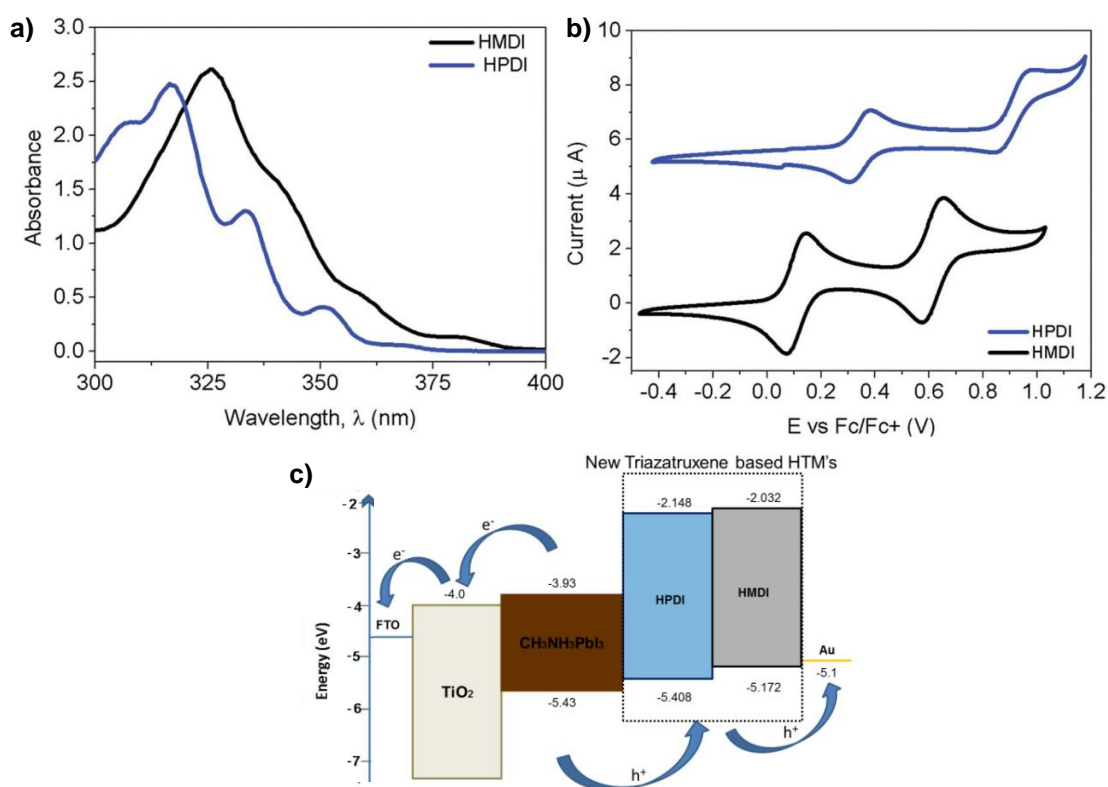


Figure 3.20. a) UV-Vis absorbance spectra of HTMs measured in a dilute solution of chlorobenzene, b) cyclic voltammograms of HTMs measured in 0.1 M solution of tetra-n-butylammonium hexafluorophosphate in dichloromethane using a glassy carbon working electrode, Pt reference electrode, and Pt counter electrode with Fc/ Fc⁺ as the internal standard. Note: to match the scale the current on Y-axis was offset to 5.5 mA in case of HPDI curve and c) energy level diagram for the fabricated photovoltaic devices using HMDI and HPDI as HTMs.

After checking the availability to introduce these novel compounds as HTMs in PSC since the HOMO level is compatible with the use of perovskite absorber and the solubility is adequate to be deposited by solution process methods, device integration of PSC containing HMDI and HPDI compounds were prepared.

In Figure 3.21, cross sectional SEM pictures of a device containing HPDI as HTM (before gold cathode evaporation) is included to estimate the thickness of HTM layer and the intimate contact with perovskite layer is under it.

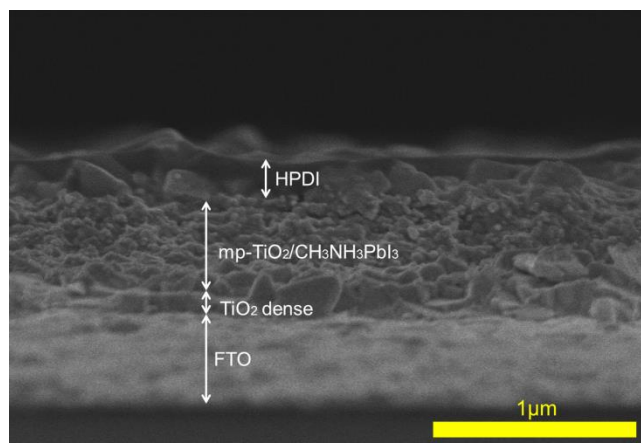


Figure 3.21. Cross sectional scanning electron microscopy image (SEM) image of the photovoltaic devices using HPDI as HTM.

Finally, for PV characterization, both J - V and IPCE characterization measurements were developed as usual for PSC containing triazatruxene based HTMs. In Table 3.8 the principal PV parameters (J_{sc} , V_{oc} , FF, PCE) expressed as mean \pm SD are indicated for cells prepared in the same batch employing three different HTM configurations: pristine HMDI, pristine HPDI and HPDI containing LiTFSI salt. In Figure 3.22, J - V and IPCE curves for champion devices prepared with each configuration are shown.

Table 3.8. Photovoltaics parameters derived from J - V measurements for $\text{CH}_3\text{NH}_3\text{PbI}_3$ perovskite based solar cells using the synthesized triazatruxene molecules.^a

HTM		J_{sc} (mA cm ⁻²)	V_{oc} (mV)	FF	PCE (%)
HMDI		14.43	938	0.637	8.62
	Mean \pm SD	14.31 \pm 1.73	907 \pm 26	0.551 \pm 0.070	7.13 \pm 1.14
HPDI		16.51	897	0.663	9.83
	Mean \pm SD	16.80 \pm 0.23	893 \pm 4	0.642 \pm 0.020	9.62 \pm 0.17
HPDI + LiTFSI ^b		19.16	976	0.576	10.82
	Mean \pm SD	18.69 \pm 0.39	961 \pm 21	0.562 \pm 0.010	10.15 \pm 0.53

^aAverage data and standard deviation calculated for 3 cells in the same batch. Mask size: 0.159 cm².

^bMeasured at 99.5 mW cm⁻² under AM 1.5G spectra.

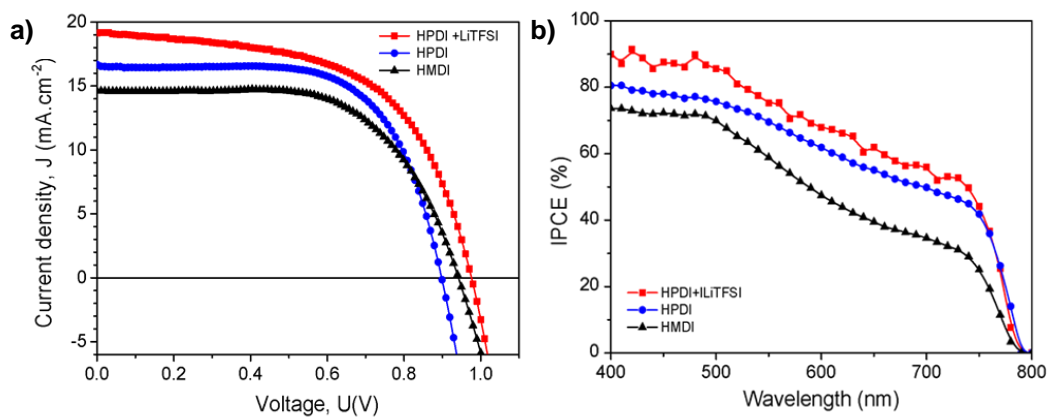


Figure 3.22. a) Current-Voltage characteristics for the PSC employing HPDI with LiTFSI salt as additive (red), pristine HPDI (blue) and pristine HMDI (black) and b) IPCE spectra for the devices shown in a).

4. Global discussion of results

4.1 PSC based on nanocolumnar plasma deposited ZnO thin films

Nanocolumnar ZnO thin films grown by plasma enhanced-chemical vapor deposition (PECVD) were successfully implemented as photoanodes in PSC. Film properties such as microstructure, crystallinity, porosity, defect concentration of ZnO can be easily tuned by changing substrate temperature during deposition and the characteristics of the plasma used with PECVD technique. In addition, the thickness of the film can be fixed by controlling the deposition time.

In Figures 3.2a-c, the preferential growth along the perpendicular axis of ZnO nanocolumnar films as well as the homogeneous distribution over the surface can be esteemed independently of the total thickness of the film. For the optimal thickness chosen for device integration (300 nm), a very good infiltration of perovskite throughout porous film was perceived in Figure 3.2d.

PV characteristics were studied for different deposition conditions using sequential deposition route finding 1M PbI_2 and 8 mg mL^{-1} MAI solution concentrations as optimal conditions as it was specified in Table 3.1. In Figure 3.3a, the two different perovskite annealing temperatures here studied (70°C and 100°C) were compared, observing as annealing temperature increases PCE is enhanced, principally by J_{SC} increase, which suggest better perovskite infiltration in the porous nanocolumnar structure or better conversion of the perovskite. More precisely, PCE at 70° annealing temperature was only 3.9% efficient ($J_{SC}=12.5 \text{ mA cm}^{-2}$, $V_{OC}=792 \text{ mV}$ and a fill factor of $\text{FF}=0.391$), while for higher temperature (100°C), PCE=4.8% was reached ($J_{SC}=16.0 \text{ mA cm}^{-2}$, $V_{OC}=718 \text{ mV}$ and a fill factor of $\text{FF}=0.412$).

On the other hand, poly(triarylamine) was also compared with standard 2,2',7,7'-tetrakis(N,N-di-p-methoxyphenylamine)-9,9'-spirobifluorene (Spiro-OMeTAD) as HTM, showing much lower performance with only PCE=1.3% was reached ($J_{SC}=8.3 \text{ mA cm}^{-2}$, $V_{OC}=481 \text{ mV}$ and a fill factor of $\text{FF}=0.327$), indicating the poor quality of the interface perovskite/PTAA since the J_{SC} and V_{OC} were reduced significantly (Table 3.1).

For charge transfer impedance spectroscopy analysis (see Appendix section for results) revealed the principal mechanism which hampers power conversion was the high recombination presented for all the ZnO nanocolumnar photoanode based PSC.

4.2 Nanocolumnar 1-dimensional TiO₂ photoanodes deposited by PVD-OAD for PSC fabrication

Highly ordered, well packaged and uniform over large area 1D porous tilted NC-TiO₂ films were fruitfully grown by PVD-OAD technique. The here assembled solar cells, with optimized photoanode properties: thickness and glancing angle of the photoanode, employed industrially accepted methods, concreting an easy implementation for large scale fabrication.

By changing the glancing incidence angle (α) the tilting angle of the final NC-TiO₂ film (β) can be tuned, being consequently modified the porosity and the refractive index of the final film. By controlling the deposition time, the thickness of the final film is controlled as well.

Cross sectional SEM pictures (Figures 3.5a-b) revealed the differences in morphology between the NC-TiO₂ photoanodes prepared with different α . It was confirmed that the NC-TiO₂ photoanodes deposited under higher glancing angle were not only more tilted ($\alpha=85^\circ; \beta \sim 47^\circ$), but also more porous than the TiO₂ films prepared with lower α ($\alpha=70^\circ; \beta \sim 34^\circ$). Both the remarkably good packaging of the nanocolumnar film and the noticeably homogeneity over high areas was confirmed in top view SEM (Figure 3.5c). After perovskite deposition, a regular and conformal capping layer on the top of photoanode was observed, reducing the roughness of the system (Figure 3.5d). In order to confirm the effective penetration of the CH₃NH₃PbI₃ absorber inside the porous photoanode scaffold, a 530 nm thick NC-TiO₂ film was infiltrated with perovskite deposited by solution processes and cross sectional SEM was recorded (Figure 3.5e), where adequate infiltration of the perovskite along the layer was perceived. To observe the effective and homogeneous penetration of CH₃NH₃PbI₃ into NC-TiO₂ using the structure presented in Figure 3.5e (FTO/bl-TiO₂/NC-TiO₂/CH₃NH₃PbI₃), time of flight-secondary ion mass spectrometry (ToF-SIMS) measurements were completed over that sample (Figure 3.6). In this Figure, lead based species (PbO⁺ and Pb⁺) are used to clarify the distribution of perovskite inside the device. The most exceptional consideration is Ti⁺ signals runs almost parallel with lead ones (PbO⁺ and Pb⁺) along the full NC-TiO₂ structure confirming the exceptional distribution and penetration of the perovskite inside the pores of the NC-TiO₂ film as it was suggested in Figure 3.5e. Moreover, during the initial timescale, Ti⁺ signal is reduced while PbO⁺ and Pb⁺ were incremented, fact which is consistent with the capping layer observed in Figure 3.5d. Further explanations regarding ToF-SIMS characterization can be found in Appendix section. To close morphological characterization a cross sectional SEM for the full device is shown in Figure 3.5f, where the thickness of each layer can be observed.

Five different configurations of NC-TiO₂ photoanodes were tested for PSC fabrication to find the optimal conditions. For instance, 100 nm $\alpha=70^\circ$, 100 nm $\alpha=85^\circ$, 200 nm $\alpha=70^\circ$, 200 nm $\alpha=85^\circ$, 300 nm $\alpha=70^\circ$, 300 nm $\alpha=85^\circ$ and 500 nm $\alpha=70^\circ$ were the studied configurations. In Table 3.2 and Figure 3.7 a summary of PV parameters obtained for the PSC containing NC-TiO₂ is presented. Focusing only in the devices with Spiro-OMeTAD as HTM, some trends can be addressed. Generally speaking, as the PCE of any PV devices is directly related to J_{SC} , V_{OC} and FF, the final efficiency of the devices was a balance between those parameters.

300 nm thick NC-TiO₂ photoanodes presented higher short circuit photocurrents, while 200 nm thick ones exhibited higher voltages. This reduction in thickness suggests lower overall recombination. On the other hand, as thickness increases fill factor decreases. Therefore, best results in terms of PCE were shown by 200 and 300 nm thick devices with no significant differences between them. The optimum porous tilted NC-TiO₂ films to be implemented as photoanode in PSC resulted 200 nm under $\alpha=85^\circ$, combining the lower voltage losses of thinner samples with the higher capabilities of absorbing more perovskite material by the increase in porosity, (*i.e.* higher glancing angle), presenting an overall efficiency for the champion device of PCE=10.53% ($J_{SC}=16.68 \text{ mA cm}^{-2}$, $V_{OC}= 949.8 \text{ mV}$ and a fill factor of FF=0.639) under 0.961 Suns (AM 1.5G).

When PTAA was employed as HTM, a reduction of PCE by decreasing of photocurrent was observed, in a similar way to ZnO columnar photoanode structures studied in the previous chapter.

Statistical histograms for the prepared PSC can be consulted in the available supplementary information of the publication.

Finally, PSC based on NC-TiO₂ photoanodes were found more stable with time than standard mp-TiO₂ films based on TiO₂ spheres (Figure 3.8), suggesting columnar films enhance the protection of perovskite to ambient conditions by reducing the effective area is exposed to external environment.

4.3 Porous 1-dimensional nanocolumnar structures as effective photonic crystal for PSC

Three architectures of porous 1-dimensional photonic crystals (1-DPC) consisting on alternated nanocolumnar films with different refractive index deposited by physical vapor deposition at oblique angle (PVD-OAD) were implemented as effective photoanodes of $\text{CH}_3\text{NH}_3\text{PbI}_3$ solar cells improving the PV characteristics by optical management of the incident light. The technique employed allows an easy large scale implementation.

In Figure 3.9 the architectures of the different photonic crystal like structures were presented. For 1-DPC Type 1 (PC1), five TiO_2 layers (~ 75 nm) with alternating refractive index ($n = 1.80/n = 1.63/n = 1.80/n = 1.63/n = 1.80$) were prepared over a bl- TiO_2 . In this case the alternation in refractive index using the same material for all the prepared layers (TiO_2) was induced by a careful control over the incidence glancing angle (α), and then tuning the porosity and n of the monolayer. Since the refractive index variation from layer to layer is modest (high $n = 1.80$ vs low $n = 1.63$), the number of layers in this case has to be increased up to 5 layers to have a suitable photonic band gap (see Figure 3.9g). In PC2, the first high refractive index layer ($n = 2.10$) was made of compact TiO_2 deposited by PVD using $\alpha = 0^\circ$, while two nanocolumnar layers made of porous SiO_2 ($n = 1.31$) and porous TiO_2 ($n = 1.77$) were respectively deposited on the top utilizing $\alpha = 70^\circ$. For PC3, TiO_2 and SiO_2 nanocolumnar films were grown over a thin bl- TiO_2 under $\alpha = 70^\circ$ to create a photonic crystal like structure with alternating indices as following: $n = 1.77/n = 1.31/n = 1.77$. For all the cases analyzed here, the photonic band gap was shaped in the interval 400-500 nm (Figures 3.9g-i).

In Figure 3.10, a precise and controlled growth of the nanocolumnar structures has been proved by cross sectional SEM pictures showing very low concentration of defects in the multilayered structure. For backscattered electron SEM images (left side of Figure 3.10), lighter areas represents TiO_2 films while SiO_2 is placed in darker ones being observed a very homogeneous distribution of compounds and very drastic changes in material composition (and then in n) as it is required for a high optical quality in the formed photonic crystal architecture.

A schematic image of the spatial distribution of the square amplitude of the electrical field for a photonic crystal like structure similar with PC3 was drawn in Figure 3.11. Although it was not at scale, the explanation of the optical effect able to push the absorption properties is expressed: the reduction in the group velocity of the light near the wavelength of a stop band in a periodic dielectric. As the photons are slowed down inside PC matrix, the chances to absorb them becomes higher, not only inside the optical band gap as it is expected from augmentation in reflections inside the device but also for other wavelengths outside the optical bandgap due to the concentration of the square of the electrical field inside the PC architecture. This phenomenon was confirmed in our experiment since the increase of IPCE was produced for the whole wavelength (Figures 3.12c-d).

In Table 3.3, $J-V$ curves (Figures 3.12a and b), and box whiskers charts (Figure 3.13), principal photovoltaic performance for the PSC prepared are shown for the three PC architectures used as photoanodes in PSC and compared with a similar

photoanodes based on tilted NC-TiO₂ (analogous with the ones fabricated in the previous studies). The reference photoanode based on NC-TiO₂ (300 nm thick) presented a performance of PCE=9.56±0.37% (J_{SC} =17.87±0.53 mA cm⁻², V_{OC} =934.4±10.7 mV and FF=0.568±0.018). With the introduction of PC1, an enhancement in absorption, and subsequently in J_{SC} was observed exhibiting J_{SC} =18.56±0.55 mA cm⁻²; however, the voltage was reduced in comparison with the reference (V_{OC} =867.7±11.9 mV) since the increase in photoanode thickness promotes higher recombination issues to obtain a final gain in the PCE (PCE=10.05±0.69% with FF=0.615±0.036). The performance of PC2 was poor (PCE=4.28±1.32%, J_{SC} =15.05±1.15 mA cm⁻², V_{OC} =883.1±60.3 mV and FF=0.312±0.060), being mainly attributed to the use of a non-injecting oxide (NC-SiO₂) just over the compact layer. In the case of PC3, an improvement of J_{SC} by the well design of PC structure, together with the shrink of photoanode which endorses an enhancement in terms of V_{OC} regarding reference photoanode, lead to reach a final overall PCE=11.52±0.30%, with J_{SC} =18.44±0.32 mA cm⁻², V_{OC} =1026.1±5.5 mV and FF=0.603±0.012, and showing for the champion cell a PCE=12.03 (J_{SC} =18.677 mA cm⁻², V_{OC} =1028 mV and FF=0.616) under 0.983 Suns (AM 1.5G).

Finally, more detailed optical characterization and both top view and cross sectional SEMs before and after perovskite penetration are addressed in Appendix section.

4.4 A dopant free linear acene derivative as a HTM for PSC

A linear acene molecular organic semiconductor: 6,13-bis(triisopropylsilylethynyl)pentacene (TIPS-pentacene), was successfully employed as HTM in PSC. This molecule is a potentially cheap material, showing HOMO level compatible with the valence band of perovskite (HOMO=-5.4 eV, LUMO=-3.53 eV), with interesting conductivity ($3.5 \times 10^{-7} \text{ S cm}^{-1}$ in pristine form) and soluble in many organic solvents and widely reported in literature. It has been utilized without any additive as HTM in PSC showing improved stability and lower hysteresis than additive based one.

In Figure 3.14a molecular structure of TIPS-pentacene is presented. Cyclic voltammograms using Fc/Fc⁺ as internal standard (Figure 3.14b) revealed a reversible redox couple, since anodic/cathodic peak ratio was close to unity, in both for pristine TIPS-pentacene and Spiro-OMeTAD; nevertheless, TIPS-pentacene displays lower HOMO level (more negative vs vacuum). After adding LiTFSI and t-BP to TIPS-pentacene, two trends were contrasted: the left shifting of cathodic peak suggesting higher HOMO level for additive add TIPS-pentacene in comparison with its pure form and the unusual absence of reversibility. The irreversibility in CV peaks for doped TIPS-pentacene was ascribed, in this case, with the introduction of trap sites or disorder in chain packing. Considering those results, frontier orbitals obtained for TIPS-pentacene and Spiro-OMeTAD are summarized in Figure 3.14c and Table 3.4, exhibiting HOMO= -5.4 eV and LUMO= -3.53 eV for TIPS-pentacene meanwhile for Spiro-OMeTAD HOMO=-5.07eV and LUMO=-2.09 eV. Regarding conductivity measurements in film, TIPS-pentacene shows remarkable behavior even before adding LiTFSI and t-BP ($3.5 \times 10^{-7} \text{ S cm}^{-1}$), being increased when additives were incorporated ($1.0 \times 10^{-5} \text{ S cm}^{-1}$).

Cross sectional SEM images were made to analyze the morphology of the prepared solar cells (Figure 3.15). Successful complete penetration of perovskite into mesoscopic TiO₂ photoanode (~250 nm) was achieved; being well differentiated part of the perovskite infiltrated into perovskite and a CH₃NH₃PbI₃ capping layer over that. On the top of the capping layer, ~150 nm TIPS-pentacene were formed, presenting also comparable thickness when LiTFSI and t-BP were added to TIPS-pentacene.

After trying several processing parameters such as solvent employed to dispense HTM and concentration of additives, the use of toluene as solvent to dispense TIPS-pentacene as such was found as preferable solvent.

In Table 3.5 and Figure 3.16, photovoltaic behavior of PSC containing TIPS-pentacene as HTM is summarized. Pristine TIPS-pentacene as HTM showed an average performance of $J_{SC} = 20.84 \pm 0.01 \text{ mA cm}^{-2}$, $V_{OC} = 913 \pm 5 \text{ mV}$ and $FF = 0.60 \pm 0.01$ for an average PCE=11.51±0.31%, with a champion cell reaching $J_{SC} = 20.86 \text{ mA cm}^{-2}$, $V_{OC} = 918 \text{ mV}$ and $FF = 0.62$ to obtain PCE=11.82% under 1 Sun (AM 1.5G). On the other hand, the introduction of additives didn't help to push the PV properties obtaining only $J_{SC} = 16.51 \pm 0.49 \text{ mA cm}^{-2}$, $V_{OC} = 920 \pm 4 \text{ mV}$ and $FF = 0.54 \pm 0.01$ with an efficiency of PCE=8.20±0.23%.

It is worthy to mention the low grade of hysteresis when additive free TIPS-pentacene was employed (PCE=11.82% in reverse scan while PCE=10.90% (it can be contrasted in Appendix section).

Moreover, since LiTFSI salt is well known as highly hygroscopic compound, it was expected to contribute in reducing the stability of the PV systems which contained it. Thus, stability of additive free TIPS-pentacene was demonstrated higher than the additives free one. After 3 months, PCE of pure TIPS-pentacene based devices was similar with the original one whereas for TIPS-pentacene + LiTFSI + t-BP, the PCE was reduced by half just after two weeks (see Appendix section).

4.5 Non-aggregated Zn(II)octa(2,6-diphenylphenoxy) phthalocyanine as a HTM for efficient PSC

TT80, a novel non-aggregated Zn(II)octa(2,6-diphenylphenoxy) phthalocyanine has been implemented as HTM for PSC fabrication by solvent deposition. This has been the first proof of concept to use phthalocyanine compound as effective HMT for PSC. The introduction of umbrella-like 2,6-diphenylphenoxy groups allows avoiding aggregation and helps with the dissolution of the metal-organic molecule in organic non-polar or poorly polar solvents.

In Figure 3.17a, the molecular structure of TT80 is depicted presenting the umbrella-like 2,6-diphenylphenoxy substituents which are reported to avoid aggregation and assisting with its solubility. In Figure 3.17b, the UV-Vis absorption spectrum of TT80 in chloroform revealing a Q-band centered in 696 nm to show a deep green color.

Three different configurations were tested to analyze the photovoltaic response of TT80 containing PSC dispensed by solution process: pristine TT80 in chlorobenzene, TT80 + LiTFSI + t-BP in chlorobenzene as well and TT80 + LiTFSI + t-BP in toluene.

Photovoltaic response was summarized in Table 3.6 and Figure 3.18 disclosing a poor behavior when additives were not added to phthalocyanine compound in Chlorobenzene, presenting just 2.6% of PCE for best performing device using those conditions ($J_{SC}=11.90 \text{ mA cm}^{-2}$, $V_{OC}=578 \text{ mV}$ and $FF=0.362$), but the performance was improved significantly with the introduction of LiTFSI and t-BP additives by J_{SC} and V_{OC} enrichment. In particular, for TT80 + LiTFSI + t-BP in chlorobenzene was achieved PCE=6.7% ($J_{SC}=16.35 \text{ mA cm}^{-2}$, $V_{OC}=797 \text{ mV}$ and $FF=0.503$), whereas TT80 + LiTFSI + t-BP in toluene reached PCE=6.2% ($J_{SC}=16.91 \text{ mA cm}^{-2}$, $V_{OC}=796 \text{ mV}$ and $FF=0.450$) was attained for the champion device with each configuration respectively.

The statistical information of the here treated cells can be found in Appendix section, where PSC containing TT80 were found reasonably reproducible.

4.6 Rational design of triazatruxene based hole conductors for PSC

New HTM based on triazatruxene core: (5,10,15-trihexyl-3,8,13-trimethoxy-10,15-dihydro-5H-diindolo[3,2-a:30,20-c]carbazole) (named as HMDI) and (5,10,15-tris(4-(hexyloxy)phenyl)-10,15-dihydro-5H-diindolo[3,2-a:30,20-c]carbazole) (named as HPDI), were synthesized and applied as HTM in PSC. Alkoxy substituents were rationally assembled to triazatruxene core in order to increase the solubility in organic solvents and tuning the HOMO level of the molecules to make them compatible with the valence band of perovskite. Remarkable thermal properties and easy fabrication that potentially promote a low cost fabrication were suggested.

In Figure 3.19, the synthetic route of triazatruxene based compounds is shown. An ease of fabrication of both compounds was found, requiring very few steps for the synthesis of HMDI (3 steps from triazatruxene) and HPDI (just in one step) from triazatruxene core. Due to the side alkoxy chains, both compounds presented a very high solubility ($>100 \text{ mg mL}^{-1}$) in organic solvents as chlorobenzene or toluene.

Necessary characterization to evaluate the frontier orbitals (HOMO/LUMO) was exposed in Figure 3.20 and summarized in Table 3.7. $E_{g \text{ opt}}$ was determined through UV-Vis spectroscopy and HOMO level from cyclic voltammograms obtaining HOMO/LUMO levels of -5.17 eV/-2.03 eV for HMDI and -5.41 eV/-2.15 eV for HPDI. Since HOMO levels are higher than valence band of perovskite, HMDI and HPDI can be tested as HTM in PSC.

On account of thermal characterization of HMDI and HPDI compounds, thermogravimetry analysis and differential scanning calorimetry were done (see Appendix section), showing very high thermal stability until 400°C and low T_g , making possible to be more amorphous, so attaching well to irregular surfaces of perovskite capping layer crystals.

For morphological study of devices, cross sectional SEM pictures were recorded (Figure 3.21). Over $\text{CH}_3\text{NH}_3\text{PbI}_3$ capping layer, a uniform and well attached layer of HPDI of ~150 nm was observed.

Photovoltaic parameters obtained from J - V and IPCE characterization curves are shown in Figure 3.22 and detailed in Table 3.8. HMDI and HPDI were firstly tried as HTM in PSC in their pristine forms, *i.e.* without any kind of additive. HMDI based PSC showed PCE=7.13±1.14%, with J_{SC} =14.31±1.73 mA cm⁻², V_{OC} =907±26 mV and FF=0.551±0.070 while in the case of HPDI based ones, PCE=9.62±0.17%, with J_{SC} =16.80±0.23 mA cm⁻², V_{OC} =893±4 mV and FF=0.642±0.020 were recorded with best cells reaching 8.62% and 9.83% respectively.

In order to improve PV properties, in special photogenerated current, LiTFSI was included in the HPDI recipe showing PCE=10.15±0.53%, with J_{SC} =18.69±0.39 mA cm⁻², V_{OC} =961±21 mV and FF=0.562±0.010 with a champion device which reached PCE=10.82% (J_{SC} =19.16 mA cm⁻², V_{OC} =976 mV and FF=0.576) under

99.5 mW cm⁻² (AM 1.5G spectra). To complete PV characterization, the addition of t-BP didn't result in an augmentation of PV properties (see Appendix section).

Furthermore, full synthetic details and *J-V* hysteresis characterization can be found in the Appendix section.

5. Conclusions

In this thesis, two main general objectives were proposed: the investigation of new photoanode architectures and the implementation of innovative HTM in PSC.

More in detail, regarding novel photoanodes, several porous 1-dimensional structured photoanodes made of cost-effective inorganic metal oxides and using scalable and homogeneous over large area deposition techniques were addressed. Different architectures, such as plasma enhanced chemical vapor deposition (PECVD) and physical vapor deposition at oblique angle (PVD-OAD) were integrated in PSC and the performance of the PSC devices which contained those photoanodes was analyzed. Some specific conclusions can be also detailed:

- Nanocolumnar ZnO thin films deposited by PECVD were employed as PSC photoanodes. Diverse properties, *e.g.* as microstructure, crystallinity, porosity, defect concentration of ZnO can be controlled by varying different conditions during deposition. Thickness of the film, annealing temperature of perovskite material and the use of an adequate HTM were found the most critical parameters in order to fabricate PV devices. After adjusting the optimal conditions during fabrication, PCE=4.8% PSC was attained. It has been as the first approach ever reported for a dry route synthesized photoanode implemented in PSC.
- Porous tilted nanocolumnar titania (NC-TiO₂) films deposited by PVD-OAD were satisfactory applied as photoanodes in PSC. The influence of morphological properties such as thickness and porosity of the film driven by glancing angle modification (α) resulted critical in order to optimize the system. The impact of morphology on final PV properties was also studied. The effect of infiltration of perovskite inside the mesoporous photoanode scaffold was also proven and analyzed by ToF-SIMS. After device optimization, samples over 10% efficiency were prepared (PCE=10.53%). NC-TiO₂ based structures resulted in more stable than the state of the art ones.
- Three original porous 1-dimensional photonic crystals (1-DPC) deposited by PVD-OAD technique were used as photoanodes in PSC exhibiting enhanced absorption properties as proof of concept. Optical characterization, device integration and optimization were also completed showing >12% efficient devices.

For the application of novel HTM into PSC, some materials were proposed gathering some important trends in order to be adopted as HTM into PSC, such as HOMO level compatible with hole injection from perovskite valence band, easy production which can potentially replace expensive Spiro-OMeTAD and adequate solubility in organic solvents. Some specific conclusions can be highlighted in each case:

- Although TIPS-pentacene is a familiar organic semiconductor, its use as HTM in PSC has been addressed for first time in this thesis. 6,13-bis(triisopropylsilylethynyl) pentacene showed a compatible HOMO level to be used in PSC systems (HOMO = -5.4 eV/LUMO= -3.53 eV), with acceptable conductivity, soluble in many solvents and with the opportunity of avoiding the addition of highly hygroscopic Li salt additives, hence provoking more stable and hysteresis free photovoltaic devices. Thus, devices with power conversion efficiencies, of 11.8% were fabricated.

- Zn(II)octa(2,6-diphenylphenoxy) phthalocyanine (TT80) has been employed as HTM in PSC, being the first approach of substituted phthalocyanine compound as HTM into PSC technologies. Umbrella-like substituent (2,6-diphenylphenoxy) allows to dissolve phthalocyanine in many organic solvent and circumventing the formation of aggregates. PSC employing this deep green compound as HTM, reached PCE=6.7% with a satisfactory inclusion of additives.
- Two new compounds based on triazatruxene core with alkoxy substituents were conceived: (5,10,15-trihexyl-3,8,13-trimethoxy-10,15-dihydro-5H-diindolo[3,2-a:30,20-c]carbazole) (HMDI) and (5,10,15-tris(4-(hexyloxy)phenyl)-10,15-dihydro-5H-diindolo[3,2-a:30,20-c]carbazole) (HPDI). HOMO/LUMO levels were totally compatible for their integration in PSC (-5.17 eV/-2.03 eV for HMDI and -5.41 eV/-2.15 eV for HPDI). These compounds also presented excellent thermal properties and low cost fabrication being candidates to create a family of highly efficient HTMs for PSC fabrication since PCE over 10% were achieved.

In conclusion, new alternatives here proposed both for photoanode and HTM engineering could pave important ways for future PSC development. On the one hand, although non-porous photoanodes can be found in literature, the best results in the state of the art suggests the use of porous based ones, so additional improvements in homogeneous large area deposition routes are still required. On the other hand, for industrial development of PSC technologies, Spiro-OMeTAD has to be removed, not only due to its high price but also by its poor behavior without additives such as LiTFSI or t-BP. These additives improve the performance of the system at the expense of long term device stability. Finally, new compositions and deposition routes for perovskite absorber are also necessary to be studied in future works to promote this technology.

Appendix



SERVICIO DE DOCTORADO

PRESENTACIÓN DE TESIS DOCTORAL

REGULADO POR R.D. 99/2011 (NORMATIVA REGULADA POR ACUERDO 7.2/CG 17-6-11)

La Comisión Académica del programa de doctorado
CIENCIA Y TECNOLOGÍA DE NUEVOS MATERIALES

utilizando el procedimiento acordado por la misma, previo informe del director/es, así como del tutor, ha acordado

AUTORIZAR **NO AUTORIZAR** la presentación de la tesis doctoral cuyos datos se citan a continuación:

DOCTORANDO		
NOMBRE	APELLIDOS	
FCO. JAVIER	RAMOS MELLADO	
DENOMINACIÓN DEL PROGRAMA DE DOCTORADO CURSADO POR EL DOCTORANDO		
CIENCIA Y TECNOLOGÍA DE NUEVOS MATERIALES. LÍNEA DE INVESTIGACIÓN: NANOMATERIALES		
DIRECTOR/ES DEL PLAN DE INVESTIGACIÓN		
NOMBRE Y APELLIDOS	DNI	UNIVERSIDAD / CENTRO / DEPARTAMENTO / INSTITUTO
SHAHZADA AHMAD	Y2232028-F	ABENGOA RESEARCH
TUTORIA DEL PLAN DE INVESTIGACIÓN		
NOMBRE Y APELLIDOS		
AGUSTÍN RODRÍGUEZ GONZÁLEZ-ELIPE		
DENOMINACIÓN DEL PLAN DE INVESTIGACIÓN		
PROGRAMA DOCTORADO: CIENCIA Y TECNOLOGÍA DE NUEVOS MATERIALES.		
DEPARTAMENTO: QUÍMICA INORGÁNICA		
LÍNEA DE INVESTIGACIÓN: NANOMATERIALES		
TÍTULO DE TESIS: NUEVOS FOTOÁNODOS Y NUEVOS MATERIALES TRANSPORTADORES DE HUECOS PARA LA FABRICACIÓN DE CELDAS SOLARES FOTOVOLTAICAS BASADAS EN PEROVSKITA (NEW PHOTOANODES AND HOLE TRANSPORTING MATERIALS FOR THE FABRICATION OF PEROVSKITE-BASED SOLAR CELLS)		

Sevilla, 11 de abril de 2016

El director (1)

Fdo. Shahzada Ahmad

El director (2)

Fdo.

El director (3)

Fdo.

El tutor

Fdo. Agustín Rguez. Glez.-Elipe

El Presidente de Comisión Académica

PROGRAMA DE DOCTORADO
CIENCIA Y TECNOLOGÍA DE
NUEVOS MATERIALES

SR. PRESIDENTE DE LA COMISIÓN DE DOCTORADO

Fdo.: José Antonio Odriozola Gordón
Presidente Comisión Académica

Appropriateness report


According to Article 9 of Agreement 9.1 / CG 04/12/19, this thesis is presented as a thesis by publication of articles, the appropriateness of this alternative has to be justified.

These days, the presentation of thesis by publication of articles is an option with increasing interest in various scientific and engineering fields. A thesis using this approach, justify the merit of thesis as publications in scientific peer-reviewed articles in specialized journals, gives more recognition, visibility and citations to the PhD student work inside the scientific community. Moreover, as the individual articles are already scrutinized by the expert journal referees, the examination process and valuation of PhD student research can be made more easily.

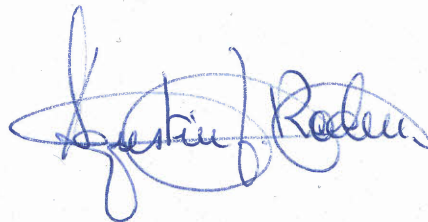
In this case, the PhD candidate: Fco. Javier Ramos has published six (6) first author publications in high impact factor journals, which are in first quarter of international scientific journals. Thus, the requirements to present the thesis by compilation of articles is fully justified and achieved. The presentation of this thesis as a thesis by publications is recommended according international quality standards.

Seville, April 8th, 2016

Director:


Shahzada Ahmad

Tutor:


Agustín Rodríguez
González-Elípe

Commission Ph.D.:


UNIVERSIDAD DE SEVILLA
PROGRAMA DE DOCTORADO
CIENCIA Y TECNOLOGÍA DE
NUEVOS MATERIALES
Fdo.: José Antonio Odrizola Gordón
Presidente Comisión Académica

Contribution report

According to Article 9 of Agreement 9.1 / CG 04/12/19, as all the works contained in this thesis by publications have more than four coauthors, the contribution of each author is detailed as following.

- F. J. Ramos, M. C. López-Santos, E. Guillén, M. K. Nazeeruddin, M. Grätzel, A. R. González-Elipe, and S. Ahmad, "Perovskite Solar Cells Based on Nanocolumnar Plasma- Deposited ZnO Thin Films," *ChemPhysChem*, vol. 15, no. 6, pp. 1148–1153, 2014.

FJRM performed the experiments and fabricated the devices. MCLS deposited ZnO films and ARGE supervised the work. EG performed EIS measurements. FJRM, ARGE and SA analyzed the data and prepared the manuscript while MKN and MG supervised the device fabrication. SA directed the project. All authors reviewed the paper.

- F. J. Ramos, M. Oliva-Ramirez, M. K. Nazeeruddin, M. Grätzel, A. R. Gonzalez-Elipe, and S. Ahmad, "Nanocolumnar 1-dimensional TiO₂ photoanodes deposited by PVD-OAD for perovskite solar cell fabrication," *J. Mater. Chem. A*, vol. 3, pp. 13291–13298, 2015.

FJRM performed the experiments, fabricated and optimized the solar cells. MOR deposited these structures under the supervision of ARGE and also made the ToF-SIMS measurement, while MKN and MG supervised the device fabrication part. SA directed the work. All authors discussed the results and commented on the manuscript

- F. J. Ramos, M. Oliva-Ramirez, M. K. Nazeeruddin, M. Grätzel, A. R. Gonzalez-Elipe, and S. Ahmad, "Light management: porous 1-dimensional nanocolumnar structures as effective photonic crystals for perovskite solar cells," *J. Mater. Chem. A*, vol. 4, pp. 4962 – 4970, 2016.

FJRM performed the experiments, fabricated and optimized the solar cells. MOR deposited photonic crystal like structures under the supervision of ARGE and also made the optical characterization, while MKN and MG supervised the device fabrication part. SA directed the work. All authors discussed the results and commented on the manuscript

- S. Kazim‡, F. J. Ramos‡, P. Gao, M. K. Nazeeruddin, M. Grätzel, and S. Ahmad, "A dopant free linear acene derivative as a hole transport material for perovskite pigmented solar cells," *Energy Environ. Sci.*, vol. 8, pp. 1816–23, 2015.

SK and FJRM contributed equally to this work. FJRM performed the experiments and fabricated the devices. TIPS-pentacene molecule was synthesized by PG. SK made electro-optical and thermal measurements. MKN and MG contributed to the supervision of the device fabrication. SA directed the work. All authors reviewed the paper.

- F. J. Ramos, M. Ince, M. Urbani, A. Abate, M. Grätzel, S. Ahmad, T. Torres, and M. K. Nazeeruddin, "Non-aggregated Zn(II)octa(2,6-diphenylphenoxy) phthalocyanine as a hole transporting material for efficient perovskite solar cells," *Dalton Trans.*, vol. 44, no. 23, pp. 10847–51, 2015.

FJRM performed the experiments and fabricated the devices. Phthalocyanine molecule (TT80) was synthesized by MI and MU under the supervision of TT and was characterized. AA also contributed to PSC fabrication. MG, SA and TT contributed to the supervision of the project while MKN directed the work. All authors discussed the results and commented on the manuscript.

- F. J. Ramos, K. Rakstys, S. Kazim, M. Grätzel, M. K. Nazeeruddin, and S. Ahmad, "Rational design of triazatruxene-based hole conductors for perovskite solar cells," *RSC Adv.*, vol. 5, pp. 53426–32, 2015.

FJRM performed the experiments and fabricated the devices. HMDI and HPDI molecules were synthesized and characterized by KR. UV-vis measurements were made by SK and thermal characterization was made by SK and FJRM. MG and MKN contributed to the supervision of device fabrication. SA and SK had the idea and directed the work. All authors discussed the results and commented on the manuscript.

Seville, April 7th, 2016

Director of the thesis:


Shahzada Ahmad

Report of scientific relevance of the publications

Firstly, full reference of the works here compiled as a thesis by publications is provided in this section including: title of the publication, year of publication, name of the scientific journal with impact factor and quartile and number of citations of the work according both Google Scholar and CrossRef (Table A.1).

Table A.1. Summary of the scientific relevance for the publications contained in this thesis. Last updated: 12.04.2016.

Publication title	Year	Journal name	Impact factor	Quartile	Citations (Google Scholar)	Citations (CrossRef)
Publications contained in this thesis						
Perovskite Solar Cells Based on Nanocolumnar Plasma-Deposited ZnO Thin Films	2014	ChemPhysChem	3.419	Q1	29	20
Nanocolumnar 1-dimensional TiO ₂ photoanodes deposited by PVD-OAD for perovskite solar cell fabrication	2015	J. Mater. Chem. A	7.443	Q1	4	5
Light management: porous 1-dimensional nanocolumnar structures as effective photonic crystals for perovskite solar cells	2016	J. Mater. Chem. A	7.443	Q1	0	0
A dopant free linear acene derivative as a hole transport material for perovskite pigmented solar cells	2015	Energy Environ. Sci.	20.523	Q1	16	16
Non-aggregated Zn(II)octa(2,6-diphenylphenoxy) phthalocyanine as a hole transporting material for efficient perovskite solar cells	2015	Dalton Trans.	4.197	Q1	15	10
Rational design of triazatruxene-based hole conductors for perovskite solar cells	2015	RSC Adv.	3.840	Q1	3	2

After that, a summary report has been also completed not only including first authorship publications but also for all the collaborations made by the candidate during the PhD in order to evaluate total number of citations, i10 index and *h*-index (Table A.2).

Table A.2. Summary of the scientific relevance for all the publications completed by the candidate during the PhD (both first author and collaborations). Last updated: 12.04.2016.

Publication title	Year	Journal name	Impact factor	Quartile	Citations (Google Scholar)	Citations (CrossRef)
Publications contained in this thesis						
Perovskite Solar Cells Based on Nanocolumnar Plasma-Deposited ZnO Thin Films	2014	ChemPhysChem	3.419	Q1	29	20
Nanocolumnar 1-dimensional TiO ₂ photoanodes deposited by PVD-OAD for perovskite solar cell fabrication	2015	J. Mater. Chem. A	7.443	Q1	4	5
Light management: porous 1-dimensional nanocolumnar structures as effective photonic crystals for perovskite solar cells	2016	J. Mater. Chem. A	7.443	Q1	0	0
A dopant free linear acene derivative as a hole transport material for perovskite pigmented solar cells	2015	Energy Environ. Sci.	20.523	Q1	16	16
Non-aggregated Zn(II)octa(2,6-diphenylphenoxy) phthalocyanine as a hole transporting material for efficient perovskite solar cells	2015	Dalton Trans.	4.197	Q1	15	10
Rational design of triazatruxene-based hole conductors for perovskite solar cells	2015	RSC Adv.	3.840	Q1	3	2
Other collaborations						
Highly efficient flexible cathode for Dye sensitized solar cells to complement Pt@TCO coatings	2014	J. Mater. Chem. A	7.443	Q1	6	7
Photoanode Based on (001)-Oriented Anatase Nanoplatelets for Organic – Inorganic Lead Iodide Perovskite Solar Cell	2014	Chem Mater.	8.354	Q1	20	15
Real-space observation of unbalanced charge distribution inside a perovskite-sensitized solar cell	2014	Nature Commun.	11.470	Q1	47	48
Elucidating Transport-	2014	J. Phys. Chem. C	4.772	Q1	31	27

Recombination Mechanisms in Perovskite Solar Cells by Small-Perturbation Techniques							
Direct monitoring of ultrafast electron and hole dynamics in perovskite solar cells	2015	Phys. Chem. Chem. Phys.	4.493	Q1	16	13	
Unraveling the Role of Monovalent Halides in Mixed Halide Organic-Inorganic Perovskites	2016	ChemPhysChem	3.419	Q1	0	0	
Conference papers							
Fabrication and encapsulation of perovskites sensitized solid state solar cells	2014	40th PVSC, IEEE (Conference paper)	-	-	2	1	

Total citations	189	164
i10-index	7	7
h-index	7	7

List of publications

Complete reference of publications finished by the PhD candidate during his PhD is listed below by order of acceptance for publication:

- J. Idígoras, E. Guillén, **F. J. Ramos**, J. A. Anta, M. K. Nazeeruddin, and S. Ahmad, "Highly efficient flexible cathode for Dye sensitized solar cells to complement Pt@TCO coatings," *J. Mater. Chem. A*, vol. 2, pp. 3175–3181, 2014.
 - **F. J. Ramos**, M. C. López-Santos, E. Guillén, M. K. Nazeeruddin, M. Grätzel, A. R. González-Elipe, and S. Ahmad, "Perovskite Solar Cells Based on Nanocolumnar Plasma- Deposited ZnO Thin Films," *ChemPhysChem*, vol. 15, no. 6, pp. 1148–1153, 2014.
 - **F. J. Ramos**, D. Cortes, A. Aguirre, F. J. Castano, and S. Ahmad, "Fabrication and encapsulation of perovskites sensitized solid state solar cells," *IEEE 40th PVSC*, no. JUNE 2014, pp. 2584–2587, 2014.
 - M. I. Dar, **F. J. Ramos**, Z. Xue, B. Liu, S. Ahmad, S. A. Shivashankar, M. K. Nazeeruddin, and M. Grätzel, "Photoanode Based on (001)-Oriented Anatase Nanoplatelets for Organic – Inorganic Lead Iodide Perovskite Solar Cell," *Chem. Mater.*, vol. 26, pp. 4675–4678, 2014.
 - V. W. Bergmann, S. A. L. Weber, **F. J. Ramos**, M. K. Nazeeruddin, M. Grätzel, D. Li, A. L. Domanski, I. Lieberwirth, S. Ahmad, and R. Berger, "Real-space observation of unbalanced charge distribution inside a perovskite-sensitized solar cell," *Nat. Commun.*, vol. 5, p. 5001, 2014.
 - E. Guillén, **F. J. Ramos**, J. A. Anta, and S. Ahmad, "Elucidating Transport-Recombination Mechanisms in Perovskite Solar Cells by Small-Perturbation Techniques," *J. Phys. Chem. C*, vol. 118, no. 40, pp. 22913–22922, 2014.
 - **F. J. Ramos**, M. Ince, M. Urbani, A. Abate, M. Grätzel, S. Ahmad, T. Torres, and M. K. Nazeeruddin, "Non-aggregated Zn(II)octa(2,6-diphenylphenoxy) phthalocyanine as a hole transporting material for efficient perovskite solar cells," *Dalton Trans.*, vol. 44, no. 23, pp. 10847–51, 2015.
 - P. Piatkowski, B. Cohen, **F. J. Ramos**, M. Di Nunzio, M. K. Nazeeruddin, M. Grätzel, S. Ahmad, and A. Douhal, "Direct monitoring of ultrafast electron and hole dynamics in perovskite solar cells," *Phys. Chem. Chem. Phys.*, vol. 17, no. 22, pp. 14674–14684, 2015.
 - **F. J. Ramos**, M. Oliva-Ramirez, M. K. Nazeeruddin, M. Grätzel, A. R. Gonzalez-Elipe, and S. Ahmad, "Nanocolumnar 1-dimensional TiO₂ photoanodes deposited by PVD-OAD for perovskite solar cell fabrication," *J. Mater. Chem. A*, vol. 3, pp. 13291–13298, 2015.
 - S. Kazim‡, **F. J. Ramos‡**, P. Gao, M. K. Nazeeruddin, M. Grätzel, and S. Ahmad, "A dopant free linear acene derivative as a hole transport material for perovskite pigmented solar cells," *Energy Environ. Sci.*, vol. 8, pp. 1816–23, 2015.
- ‡ These authors contributed equally to this work.

- **F. J. Ramos**, K. Rakstys, S. Kazim, M. Grätzel, M. K. Nazeeruddin, and S. Ahmad, "Rational design of triazatruxene-based hole conductors for perovskite solar cells," *RSC Adv.*, vol. 5, pp. 53426–32, 2015.
- M. Deepa, **F. J. Ramos**, S. M. Shivaprasad, and S. Ahmad, "Unraveling the Role of Monovalent Halides in Mixed Halide Organic- Inorganic Perovskites," *ChemPhysChem*, vol. 17, no. 6, pp. 913–920, 2016.
- **F. J. Ramos**, M. Oliva-Ramirez, M. K. Nazeeruddin, M. Grätzel, A. R. Gonzalez-Elipe, and S. Ahmad, "Light management: porous 1-dimensional nanocolumnar structures as effective photonic crystals for perovskite solar cells," *J. Mater. Chem. A*, vol. 4, pp. 4962 – 4970, 2016.



SERVICIO DE DOCTORADO

SOLICITUD DE MENCIÓN INTERNACIONAL EN EL TÍTULO DE DOCTOR

REGULADO POR R.D. 99/2011 (NORMATIVA REGULADA POR ACUERDO 7.2/CG 17-6-11)

D/D^a FCO. JAVIER RAMOS MELLADO,
nacido/a el día 29 de MAYO de 1986, con DNI/Pasaporte nº 06270984-B,
expedido en ALCÁZAR DE SAN JUAN el día 23 de ABRIL de 2014, y con domicilio en la
calle/plaza VIRGEN DE CRIPTANA, nº 56, C.P. 13610,
localidad CAMPO DE CRIPTANA, provincia de CIUDAD REAL,
teléfono 647146100, correo electrónico javieramosm@gmail.com

EXPONE:

Que ha realizado la tesis doctoral titulada NEW PHOTOANODES AND HOLE TRANSPORTING MATERIALS
FOR THE FABRICATION OF PEROVSKITE-BASED SOLAR CELLS
(NUEVOS FOTOÁNODOS Y NUEVOS MATERIALES TRANSPORTADORES DE HUECOS PARA LA
FABRICACIÓN DE CELDAS SOLARES FOTOVOLTAICAS BASADAS EN PEROVSKITA)

cuya presentación ha sido aprobada por la Comisión Académica del Programa de Doctorado:
CIENCIA Y TECNOLOGÍA DE NUEVOS MATERIALES

habiendo sido dirigida por ¹ Dr. SHAHZADA AHMAD

Que durante la realización de la tesis realizó una estancia desde 04 / 05 / 2014 hasta 01 / 08 / 2014 +
en ² ÉCOLE POLYTECHNIQUE FÉDÉRALE DE LAUSANNE (EPFL) + 15-22 / 12 / 2014 + 1-7 / 03 / 2015

colaborando en el equipo del profesor MICHAEL GRÄTZEL

Que acompaña informes favorables a la defensa de la tesis de los Profesores Doctores:

1.³ Prof. ALDO DI CARLO

2.³ Prof. HORST-GÜNTER RUBAHN

Que está dispuesto a efectuar al menos la cuarta parte de la defensa de su tesis en ⁴ INGLÉS.

SOLICITA: Poder optar a la mención internacional en el título de Doctor.

Firma

Sevilla, 11 de abril de 2016

SR. PRESIDENTE DE LA COMISIÓN DE DOCTORADO

¹ Indicar director o directores. Señalar los centros a los que están vinculados en caso de no ser profesores de la Universidad de Sevilla

² Indicar departamento, centro y país.

³ Indicar nombre, centro y país de origen

⁴ Indicar idioma.

To whom it might concern



Prof. Dr. H.-G. Rubahn
Mads Clausen Institute
University of Southern Denmark
Alsion 2
DK-6400 Sønderborg
Denmark

Tlf.: +45 6550 11 90
Fax: +45 6550 16 54

april 17, 2016

Preliminary assessment of the PhD thesis

“New Photoanodes and Hole Transporting Materials for the Fabrication of Perovskite-Based Solar Cells”

submitted by Fco. Javier Ramos Mellado to The University of Seville, Spain for the Degree of Doctor of Philosophy

Member of the Assessment Committee:

- Professor Horst-Günter Rubahn, Mads Clausen Institute, University of Southern Denmark

Supervisor: Shahzada Ahmad, Agustin Roderiguez Gonzalez-Elipse,

The thesis comprises 183 pages, including a lengthy introduction (46 pages) on general photovoltaics and principles of perovskite solar cells, a summary and discussion of the results (40 pages) and a lengthy appendix, which includes reprints of the most relevant publications of the author. The candidate has authored 13 peer reviewed publications in good to excellent journals, 6 of them as first author. He has further published a patent, submitted a patent application and gave presentations with abstracts at 10 conferences. Besides work at Abengoa he has also worked at EPFL under guidance of Michael Grätzel and M.K. Nazeeruddin.

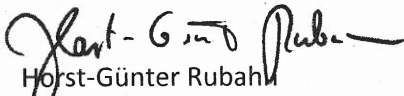
The overall goal of this thesis is to demonstrate novel electron- and hole transporting layers in perovskite solar cells (PSC) that would allow an easier upscaling and a more reliable approach to mass production of hybrid solar cells on the basis of PSC. It is no doubt that hybrid solar cells with conversion efficiencies between 10 and 20 % are a most relevant alternative at least to other kind of third generation solar cells (if not to all generation solar cells). The author shows in his work very convincingly that oblique angle physical vapor deposition under optimized deposition conditions can result in porous layered (photonic crystal) structures that serve as highly efficient photoanodes in PSC. In addition, he introduced novel molecules forming novel hole transport layers that resulted in efficiencies above 10 % and bear the potential of higher stability for the overall device.

The scientific and technical work is original and has been performed careful and precise, resulting in relevant results. Whereas the presentations in all (multi-authored) publications are very clear and concise, the introductory part of the thesis misses focus and provides background that not in all cases is most relevant to the topic of the thesis. The level of redundance between introduction, objective definition, discussion of specific results and conclusions is rather high and all these parts could have been shortened without losing content. Instead, a comparative conclusion would have been useful and also a more extended outlook. The initial, summarizing part of the thesis resembles too much the compilation of articles that forms the second part. As a technical remark, the consistent use of error bars and the english language should be checked.

However, overall the thesis and their excerpt in form of the scientific papers are well written and specifically in the detailed topics scientifically sound with very convincing results that highlight the potential of the developed techniques and materials. The publications and presentations at international conferences also impressively demonstrate the significance of the results.

Based on the independent scientific work and the high research level I suggest to accept this thesis for an oral defence.

Yours Sincerely,



Horst-Günter Rubahn
Prof.Dr.Dr.hc, Director, Mads Clausen Institute
Tel: +45 6011 3517
E-mail: rubahn@mci.sdu.dk



DIPARTIMENTO DI INGEGNERIA ELETTRONICA
UNIVERSITÀ DEGLI STUDI DI ROMA "TOR VERGATA"
Via del Politecnico 1 - 00133 ROMA – Italy

Roma, 23 April 2016

EVALUATION REPORT OF DOCTORAL THESIS

Title of the Thesis: New Photoanodes and Hole Transporting Materials for the Fabrication of Perovskite-Based Solar Cells

Name of the Thesis Author: F. Javier Ramos

Name and affiliation of the evaluator: Prof. Aldo Di Carlo
Department of Electronics Engineering
University of Rome "Tor Vergata"
Via del Politecnico 1, 00133 Roma (Italy)
Tel: +39-06-72597456
Email: aldo.dicarlo@uniroma2.it

Perovskite Solar Cells (PSCs) are revolutionizing the field of III generation photovoltaics pushing efficiency well beyond to what was achieved with previous technologies such as Organic Photovoltaics or Dye Solar Cells. Being a new PV technology, several aspects need to be optimized to scale up to industrial applications. The thesis focuses on this aspect and in particular on the development of new photoanodes and innovative Hole Transporting Materials (HTM) for PSC fabrication.

With the idea of a scalable process, in the first part of the thesis physical deposition processes are developed for the fabrication of mesoscopic photoanodes. The obtained results are state of art in the field of PSCs and represent a breakthrough for industrial exploitation of such technology. In particular, the use of nanocolumnar 1-dimensional TiO₂ photoanodes in conjunction with photonic crystal is of particular relevance.

Concerning HTM, efforts were devoted to find alternatives to the costly and low stability SPIRO-OMeTAD. A TIPS-pentacene was considered and remarkable results were achieved with such HTM even without doping, which could induce degradation of the PSC. Novel compounds based on triazatruxen and Zn-phthalocyanine molecules have been considered as HTM and a thorough investigation is presented.

In conclusion, the thesis presents results well beyond the state of art, which could impact the PSC technology. I strongly recommend the author of this thesis for the PhD degree.

Sincerely Yours

Prof. Aldo Di Carlo

Prof. Dr. Michael Graetzel
EPFL SB ISIC LPI
Station 6
CH-1015 Lausanne

Tel. +41 21 693 31 12
Fax: +41 21 693 61 00
michael.graetzel@epfl.ch

TO WHOM IT MAY CONCERN

This is to confirm that Mr Francisco Javier Ramos Mellado, born on May 29, 1986, was a visiting PhD student at the Laboratory of Photonics and Interfaces at the Swiss Federal Institute of Technology, Lausanne, Switzerland during the following periods:

- October 14th, 2012 - April 30th, 2013 (6 and a half months)
- May 31st, 2013 - August 30th, 2013 (3 months)
- September 30th, 2013 - March 30th, 2014 (6 months)
- May 4th, 2014 - August 1st, 2014 (3 months)
- December 15th - 22nd, 2014 (1 week)
- March 1st - 7th, 2015 (1 week)

These visits were organized in the framework of the collaboration between LPI and Abengoa Research, Sevilla.

Lausanne, April 18th, 2015



Prof. Michael Grätzel
Director of the Laboratory of
Photonics and Interfaces

List of stays

The following stays were completed at Laboratory of photonic and Interfaces (LPI), École Polytechnique Fédéral de Lausanne (EPFL), under the supervision of Prof. Michael Grätzel:

- October 14th, 2012 – April, 30th, 2013 (6 and a half months)
- May 31st, 2013 – August, 30th, 2013 (3 months)
- September 30th, 2013 – March 30th, 2014 (6 months)
- May 4th, 2014 – August 1st, 2014 (3 months)
- December 15th – 22nd, 2014 (1 week)
- March 1st – 7th, 2015 (1 week)

List of patents

• **Title:** “Compuesto aromático policíclico sustituido como material de transporte de huecos en células solares de estado sólido basadas en perovskita”. (“Substituted Polycyclic Aromatic Compound as a Hole Transport Material in Perovskite-Based Solid-State Solar Cells”).

Inventors: S. Ahmad, F.J. Ramos, S. Kazim, M. Doblaré Castellano, M.K. Nazeeruddin, and M. Graetzel.

Applicant: Abengoa Research, S.L. (100.0%) (ES).

Publication number: ES2563361 (14.03.2016)

Application number: P201431324 (12.09.2014)

• **Title:** “Novel Compound and their Use as Hole Transport Material”

Applicant: Abengoa Research, S.L. (100.0%) (ES).

Publication number: Pending

Application number: P201431776 (28.11.2014)

- [A. Douhal](#), P. Piatkowski, B. Cohen, **F.J. Ramos**, M.R. Di Nunzio, M.K. Nazeeruddin and S. Ahmad. "Interrogating the Dynamics of Electrons and Holes Within Perovskite-based Solar Cells".
 - [S. Ahmad](#) and **F.J. Ramos**. "Device Characterization and Structure Property Relationship in Perovskites Based Solar Cell".
 - [E. Guillén](#), **F.J. Ramos**, J.A. Anta and S. Ahmad. "Small-perturbation Characterization of Perovskite Solar Cells and Identification of Transport-recombination Mechanisms" (Poster).
 - [S. Kazim](#), **F.J. Ramos**, E. Guillén, P. Gao, M.K. Nazeeruddin, M. Graetzel and S. Ahmad. "An Efficient Organic Hole Transport Material for Mesoscopic Perovskite based Solar Cells" (Poster).
 - **F.J. Ramos**, M.K. Nazeeruddin, M. Oliva-Ramirez, M. Graetzel, A.R. Gonzalez-Elipe and S. Ahmad. "Nanocolumnar 1-D photoanodes deposited by PVD-GLAD for efficient perovskite solar cells fabrication" (Poster).
- 40th IEEE Photovoltaic Specialist Conference. Denver, Colorado (USA). June 8-13th, 2014. Poster and full text in book of Proceedings contributions. Poster nominated as finalist.

ABENGOA RESEARCH Innovative technology solutions for sustainability

Fabrication and encapsulation of solid state perovskite solar cells

F. Javier Ramos¹, David Cortés², Aranzazu Aguirre², Fernando J. Castaño^{1,2}, Shahzada Ahmad^{1*}
¹Abengoa Research, C/ Energía Solar nº 1, Campus Palmas Altas-41014, Sevilla, Spain.
²Abengoa Solar New Technologies, Soland Center, Sanlúcar la Mayor, 41800 Sevilla, Spain.

Introduction

Recently, the use of certain perovskite materials has revolutionized these devices and is currently being explored for efficient light to electricity conversion in mesoscopic solar cells [1,2]. Perovskite materials are unique in their multifunctional behavior, being capable of acting as light absorber, as well as electron and hole transporter, simple fabrication, large variety of possible combinations with other materials and tunable properties [3-5]. However, device stability and alternative deposition techniques compatible with the up-scaling processes remain mostly unexplored despite the relevance of these issues to transition into the manufacturing arena. In the present contribution, approaches for low-temperature device encapsulation will be described.

Configuration

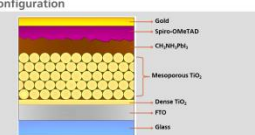


Figure 1. Schematic diagram of a perovskite solar cell.

Experimental

- **Compact TiO₂:** Spin-coating OPD of TAA in ethanol
- **Mesoporous TiO₂:** Spin-coating of 18-NRT paste in ethanol
- **Perovskite:** Sequential deposition. 1st) Spin-coating PbI₂ in DMF. 2nd) Dipping in CH_{3NH₃I in 2-propanol}
- **Spiro-OMeTAD:** Spin-coating
- **Gold:** Thermal evaporation. Sputtering for big devices.
- **Encapsulation:** Two step process. 1st) Encapsulation and curing. 2nd) Lamination at 130°C

Conclusions

- Solid state solar cells using perovskites as light absorber with a power conversion efficiency of 12% were fabricated.
- Two-step encapsulation process that ensures device thermal and mechanical stability was developed with device power conversion efficiency losses under 12%.
- A first approach for the up-scaling with a successful encapsulation was also developed.

References

[1] M. Grätzel, *Nature*, 414, 338 (2001).
[2] S. Ahmad, E. Guillén, J. Ramos, M. Graetzel, M. F. Nazeeruddin, *Energy Environ. Sci.*, vol. 6, pp. 3423-3430, 2013.
[3] S. Ahmad, M.F. Nazeeruddin, M. Grätzel, S. Ahmad, *Angew. Chem. Int. Ed.*, vol. 52, pp. 2952-2956, 2013.
[4] S. Ahmad, M. F. Nazeeruddin, S. Ahmad, *Angew. Chem. Int. Ed.*, vol. 52, pp. 2952-2956, 2013.
[5] S. Ahmad, M. F. Nazeeruddin, E. Guillén, M. F. Nazeeruddin, M. Grätzel, A. R. Gonzalez-Elipe, S. Ahmad, *Chem. Phys. Chem.*, vol. 15, pp. 1348-1353, 2014.

Results

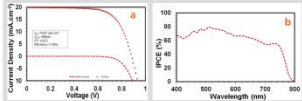


Figure 2. a) J-V curve for the champion cells prepared b) Incident Photon-to-current efficiency

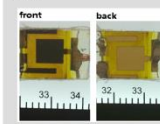


Figure 3. Front and back side of devices after encapsulation. The encapsulant materials appear clear in the cell area.

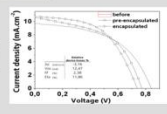


Figure 4. J-V characteristics of a device before encapsulation, after pre-encapsulation and after complete encapsulation.

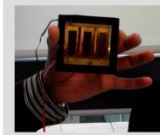
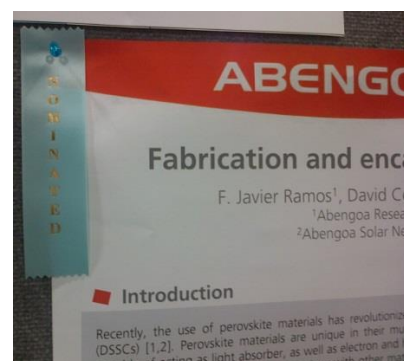



Figure 5. Photograph of a perovskite solar cell with 5cm² active area after encapsulation process.



- **F.J. Ramos**, D. Cortés, A. Aguirre, [F.J. Castaño](#) and S. Ahmad. "Fabrication and encapsulation of solid state perovskite solar cells" (Poster). Poster has been nominated for the best poster award of session 6 (Finalist)
- **F.J. Ramos**, D. Cortés, A. Aguirre, [F.J. Castaño](#) and S. Ahmad. "Fabrication and encapsulation of perovskites sensitized solid state solar cells" (Conference paper).

- PSCO15. Lausanne (Switzerland), September 27-30th, 2015.


Innovative technology solutions for sustainability

Triazatruxene-based molecules as hole transporting material in Perovskite Solar Cells

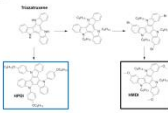
F. Javier Ramos¹, Kaspars Rakstys^{1,3}, Samrana Kazim¹, Michael Grätzel¹, Mohammad K. Nazeeruddin³ and Shahzad Ahmad¹

¹Abengoa Research, CI Energia Solar nº 1 Campus Palmas Altas 41014, Sevilla (Spain)
²Laboratory of Photonics and Interfaces, EPFL, BC, 36, EPFL, CH-1015 Lausanne (Switzerland)
³Group for Molecular Engineering of Functional Materials, OC-16-MN, Doc. 26, EPFL, CH-1521 Sion, Switzerland

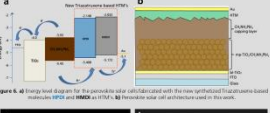
Introduction

In this work, triazatruxene-based hole transporting molecules were synthesized and used in perovskite solar cells. The HOMO levels of HTMs are comparable to the requirement in Perovskite solar cells (PSC). They present very high stability in organic solvent, good thermal properties, and high air-stability that can be increased with low concentrations of additives [2].

Synthesis



Configuration



Compound characterization

Compound	λ_{max} (nm)	ϵ_{max} (cm ² mol ⁻¹)	E_{onset}^{HOMO} (eV)	E_{onset}^{LUMO} (eV)	E_{gap}^{opt} (eV)	χ_p (eV)
HTM1	380	3.26	-5.41	-2.15	3.6	3.6
HTM2	395	3.14	-5.17	-2.03	3.1	3.1

PV Characterization

Compound	J _{sc} (mA/cm ²)	V _{oc} (V)	FF (%)	PCE (%)
HTM1	19.76	0.576	0.576	10.82
HTM2	18.69±0.39	0.561±0.021	0.562±0.010	10.74±0.13
HTM3	16.51	0.597	0.603	9.83
HTM4	16.80±0.23	0.593±0.004	0.542±0.030	8.2±0.17
HTM5	14.43	0.538	0.637	6.42
HTM6	14.31±1.73	0.507±0.038	0.531±0.010	7.13±1.14

Conclusions

- New triazatruxene-based HTMs with electron-withdrawing groups were fabricated. HTM1 and HTM2 showed HOMO/LUMO band-positions of 5.41 and 2.15 eV respectively for the synthesized perovskite solar cells.
- High efficiencies were obtained in unbalanced systems: 10.82% for HTM1 and 10.82% for HTM2. The performance was enhanced with the introduction of HTM1 and HTM2 in HTM1.
- These molecules are easy to fabricate and inexpensive alternatives to replace Spiro-OMeTAD.
- They present excellent stability in organic solvents and good thermal properties.

References

- [1] F. J. Ramos, K. Rakstys, S. Kazim, M. Grätzel, and S. Ahmad, *Energy Environ. Sci.*, 2015, 8, 2342-2348.
- [2] S. Ahmad, M. Grätzel, S. Kazim, K. Rakstys, M. K. Nazeeruddin, and F. J. Ramos, *Energy Environ. Sci.*, 2015, 8, 2342-2348.
- [3] F. J. Ramos, K. Rakstys, S. Kazim, M. Grätzel, M. K. Nazeeruddin, S. Ahmad, *Energy Environ. Sci.*, 2015, 8, 2342-2348.

Configuration

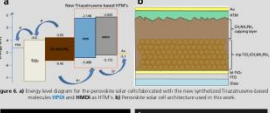


Figure 6. Energy level diagram for a perovskite solar cell fabricated with the new synthesized triazatruxene-based molecules HTM1 and HTM2. The perovskite solar cell architecture used in this work.

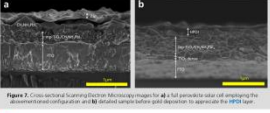


Figure 7. Cross-sectional SEM images of the perovskite solar cells for all the perovskite solar cells employing the above-mentioned configuration (a) and (b) detailed sample before gold deposition to appreciate the HTM1 layer.

PV Characterization

Compound	J _{sc} (mA/cm ²)	V _{oc} (V)	FF (%)	PCE (%)
HTM1	19.76	0.576	0.576	10.82
HTM2	18.69±0.39	0.561±0.021	0.562±0.010	10.74±0.13
HTM3	16.51	0.597	0.603	9.83
HTM4	16.80±0.23	0.593±0.004	0.542±0.030	8.2±0.17
HTM5	14.43	0.538	0.637	6.42
HTM6	14.31±1.73	0.507±0.038	0.531±0.010	7.13±1.14

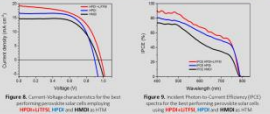



Figure 8. Current-voltage characteristics for the best performing perovskite solar cells employing HTM1 and HTM2 in HTM1.

Figure 9. Incident Photon-to-Current Efficiency (IPCE) spectra for the best performing perovskite solar cells employing HTM1 and HTM2 in HTM1.



1st International Conference on Perovskite Solar Cells and Optoelectronics, Lausanne, 27-29 September 2015

- V. Bergmann, S.A.L. Weber, **F.J. Ramos**, M.K. Nazeeruddin, M. Grätzel, D. Li, I. Lieberwirth, S. Ahmad, **R. Berger**. "Unbalanced Charge Distribution inside a Perovskite-Sensitized Solar Cell in Real Space".
- **F.J. Ramos**, K. Rakstys, S. Kazim, M. Grätzel, M.K. Nazeeruddin and S. Ahmad. "Triazatruxene-based molecules as hole transporting material in Perovskite Solar Cells" (Poster).